Modeling and Numerical Simulation of Shape Memory Alloys in Robotics Applications

by

Tyler Ross Lambert

A thesis submitted to the Graduate Faculty of
Auburn University
in partial fulfillment of the
requirements for the Degree of
Master's of Science in Mechanical Engineering

Auburn, Alabama
August 5, 2017

Keywords: Shape Memory, Simulation, Heat Transfer

Approved by

Dr. David Beale, Chair, Professor, Department of Mechanical Engineering
Dr. Roy Knight, Assistant Professor, Department of Mechanical Engineering
Dr. Royall Broughton, Professor Emeritus, Department of Polymer and Fiber Engineering

Abstract

Shape memory alloys (SMA) are uniquely alloyed metals that have the ability to change crystalline structure upon the application or removal of stress or upon heating or cooling. This change in crystalline structure gives SMA several properties that make them useful in robotics applications. For example, certain SMA can be used to create actuators that are simple, high strength, and inexpensive. However, poor electrical efficiency, a moderate lifetime, and complex mechanical behavior that makes them difficult to design into new applications and products have stymied the growth of these actuators as viable alternatives to more traditional actuators such as pneumatics or motors. In order to improve the integration of SMA actuators into modern mechanical applications, tools have been created that account for the complex thermal and mechanical behaviors of these materials under feedback controls. This was done through the development of thermo-electro-mechanical constitutive models which were then analyzed analytically and then solved numerically using routines present in multibody dynamics software ADAMS as well as through programs such as MATLAB. Models of varying complexity were implemented and compared to one another as well as to experimental results. The mechanical model utilizes 1-D constitutive equations that account for the material temperature and state of stress to determine the material state. The material state determines the electrical resistivity of the material, which drives Joule heating. Thermal cooling of the material is based on a heat transfer analysis of various geometries. These models contain information on material states that are very difficult to measure experimentally (such as crystalline phase fraction) and thus provide insight into the material behavior and design that experimental results cannot offer. The numerical models of material behavior also can then be used with a variety of control laws in order to test their stability and response time.

Acknowledgements

I would like to express my gratitude to my supervisor Dr. David Beale for the useful comments, remarks and engagement through the learning process of this master thesis. Furthermore, I would like to thank Austin Gurley for introducing me to the topic as well for the support on the way. I would like to thank Katharine Kehrt for her support throughout my stay in the graduate program. Finally, I would like to thank my family who have supported me throughout the entire process and never wavered in their full fledged support of my dreams. I will be grateful forever for your love.

Table of Contents

List of Tables

List of Illustrations

List of Abbreviations

ABS: Acrylonitrile Butadiene Styrene

BTCS: Backward Time Centered Space

CTCS: Centered Time Centered Space

DSC: Differential Scanning Calorimetry

FDM: Finite Difference Method

FTCS: Forward Time Centered Space

MBD: Multibody Dynamics

SMA: Shape Memory Alloy

SMC: Sliding Mode Control

PWM: Pulse Width Modulation

XRD: X-Ray Power Diffractograms

Chapter 1: Introduction

Shape Memory Alloys (SMA) are specially alloyed metals that undergo a change in crystal geometry when thermally cycled that causes the alloy to constrict to recover residual strains upon heating and then elongate upon cooling in the presence of a preload. By far the most economical version of these shape memory alloys come in the form of nickel titanium alloys, which are colloquially known as nitinol. The remarkable properties of nitinol was discovered in 1962 when it was fabricated in order to make a missile nose cone for the Naval Ordinance Laboratory that would resist fatigue, heat, and force of impact. One specific sample was bent out of shape and was passed around at a meeting, when a scientist applied heat from his smoking pipe to the sample and watched as the accordion shaped strip of nitinol reverted into its previous non-deformed shape.

The motion of a shape memory alloy can be controlled by heating using electric current and cooling in a surrounding fluid, typically ambient air. Due to the mechanism of actuation being dictated by the speed at which convective heat transfer can lower the temperature of the wire, repeatability and response time of SMA actuators remains a challenge in cyclic actuations, so research has been done in categorizing the selection of specific SMA for their uses in various projects as well as their appropriate sizing. SMA actuators – in this case a simple thin wire - can provides huge benefits in cost reduction and miniaturization of robotic devices, especially when the length of the SMA wire can be measured via self-sensing (i.e. without an additional position sensor). To simulate the behavior of these actuators accurately is difficult and requires many parameters that vary over time. Here, a general platform for design and analysis of SMA actuators in complex mechanical systems so that the benefits and obstacles of SMA actuators can be tested and overcome. The SMA wire actuator is coupled to a mechanical system in both a finite difference

scheme and multibody dynamics software, where it actuates the system based on feedback control laws. The model is validated by comparing the simulated systems to experimental results.

The objective of this research is to quantify a means of determining the temperature response accurately in a shape memory alloy actuator in order to determine how fast it can act in a control scheme and how suitable it is for various applications. This paper will go through the background of shape memory alloys and their method of operation and of the mathematical approach to the modelling of the heat transfer of an SMA actuator in Chapter 2. In Chapter 3, analytical approaches are investigated to determine ways to quantify the actuator temperature response, time response, efficiency, bandwidth, and distortion from measurement with a thermocouple. An electro-thermo-mechanical model of the actuator is derived with a statistically based and thermodynamically based kinetics model that provides a stable finite difference scheme to accurately predict the results of shape memory alloys in simple heating/cooling tests as well as in tensile testing. Finally, the developed models are directly compared to experimental results when paired with a variety of controller schemes. In Chapter 4, the same schemes are put into MSC ADAMS for multibody dynamics simulation of shape memory behavior and validated through the use of a ball-beam-balancer experiment. In Chapter 5, general conclusions and results are given.

Chapter 2: Background and Literature Review

2.1 Introduction to Shape Memory Alloy Actuators

Shape Memory Alloys (SMA) are specially alloyed metals that undergo a change in crystal geometry when thermally cycled that causes the alloy to contract to recover residual strains upon heating. The wires can then elongate upon cooling in the presence of a preload. This actuation is controllable through heating using electric current and cooling in a surrounding fluid, typically ambient air. Natural convection relies on buoyant forces to carry heat away from the wire, which is a relatively slow process and limits the system bandwidth significantly for SMA actuators. Therefore, research has been performed in categorizing the selection of specific SMA for their uses in various projects as well as their appropriate sizing based on both their response time and their overall efficiency, which is by all accounts their greatest shortcomings. Despite these shortcomings, SMA actuators can provide huge benefits in cost reduction and miniaturization of robotic devices, especially when the length of the SMA wire can be reliably measured without the use of an additional position sensor (Figure 1).

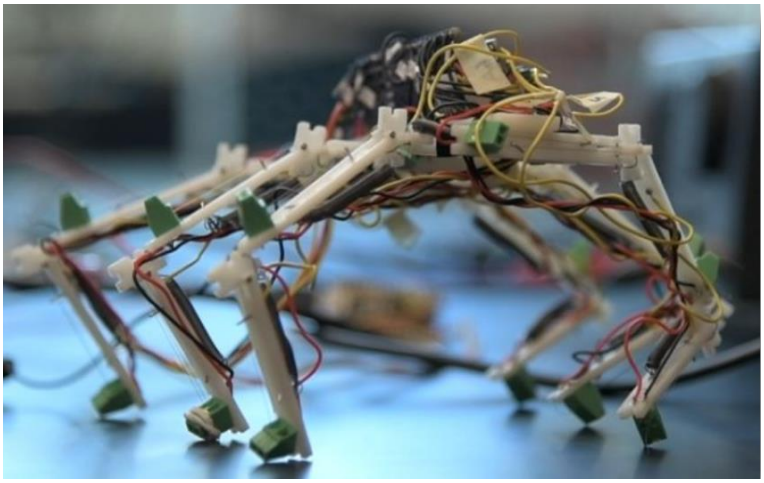

Figure 1. 16 DOF Hexapod using SMA Actuators

2.2 Mechanical Modelling

The mechanism of actuation for shape memory alloys is a change in crystal structure initiated by a change in the material temperature and stress. The two crystalline structures of interest are Austenite (*A*), an interpenetrating simple cubic structure (*B2* structure), and Martensite (*M*), a more complicated monoclinic structure (*B19* structure and its distorted variants) [1]. The Martensite structure has the unique ability to undergo limited deformation upon the application of stress without breaking atomic bonds. This phenomenon is known as *twinning*, and the deformation allows for the shifting of atomic planes at the interface of the crystalline lattices of Martensite variants without causing permanent deformation. The realigned Martensite structure is then said to be *detwinned* and typically has high values of engineering strain when compared to the twinned Martensite. Upon the application of heat to Martensite, the crystalline structure will shift back to the same interpenetrating simple cubic structure of Austenite regardless of whether the Martensite was twinned or detwinned, and it is in this matter that shape memory alloys act as actuators (Figure 2) [2].

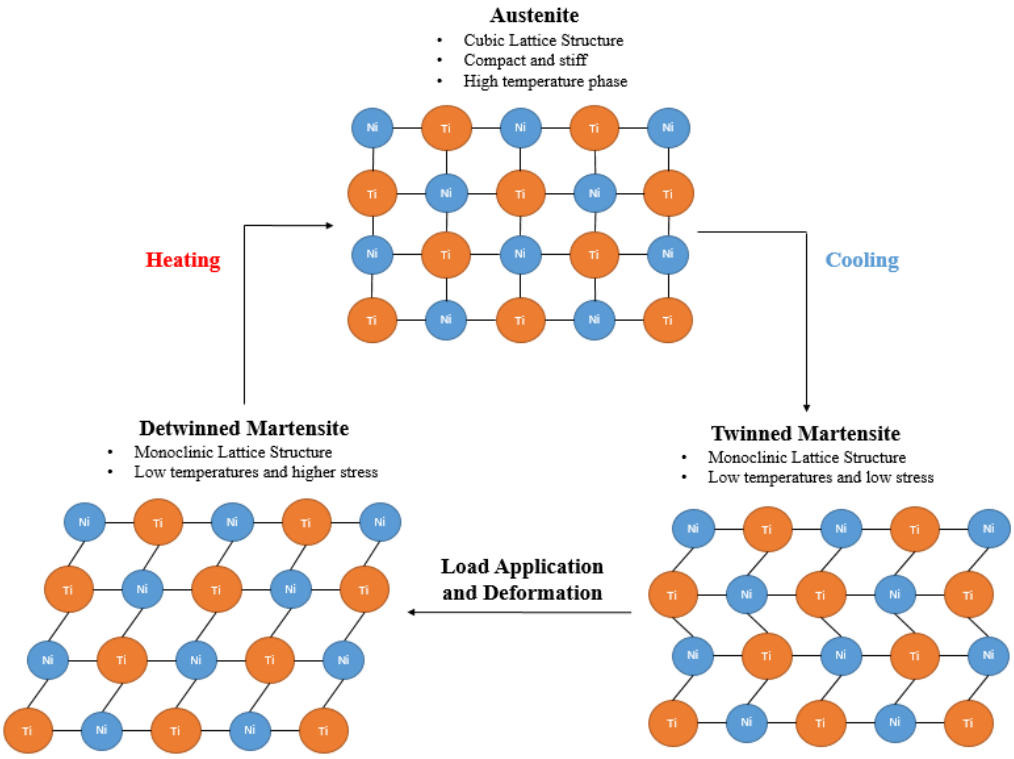

Figure 2. SMA Actuation Process

The material does not instantly transform in its entirety from one state to another. As such, intermediate fractions of the phases can be present at any given time. Conventionally, the phase composition is denoted by ξ, which is the detwinned Martensite phase fraction of the material which is bounded such that $0 \leq \xi \leq 1$. Oftentimes, the transition temperatures are considered to be defined as starting and ending temperatures that are functions of stress for a given SMA actuator (but not constant for the alloy as cold working, heat treatment, and the number of actuation cycles the actuator has undergone affect the properties) [3]. Conventionally, the start of $M \rightarrow A$ transformation is denoted as the Austenite Start (A_s) temperature and the end of the $M \rightarrow A$ transformation is denoted as the Austenite Finish (A_f) temperature. Likewise, the $A \rightarrow M$ transformation starts with the Martensite Start (M_s) and

Martensite Finish (M_f) temperatures. The region of temperatures between A_s and A_f, as well as M_s and M_f are traditionally referred to as transformation bands. In most models of mechanical behavior, these bands are considered to be the only active regions of transformation. A third crystalline structure is often seen upon cooling at lower stresses for the commonly used nickel titanium shape memory alloy, termed the R-phase. The R-phase crystalline lattice is essentially a distortion of the Austenite B2 crystalline lattice that does not provide the benefits of large strains that the Martensite to Austenite transformation does. As a result, experiments often try to eliminate the presence of the R-phase by cycling the actuator above a certain critical stress level [4, 5, 6, 7]. The relationships between the phase composition of an SMA and its temperature and stress are compactly presented on the materials' phase diagram (Figure 3).

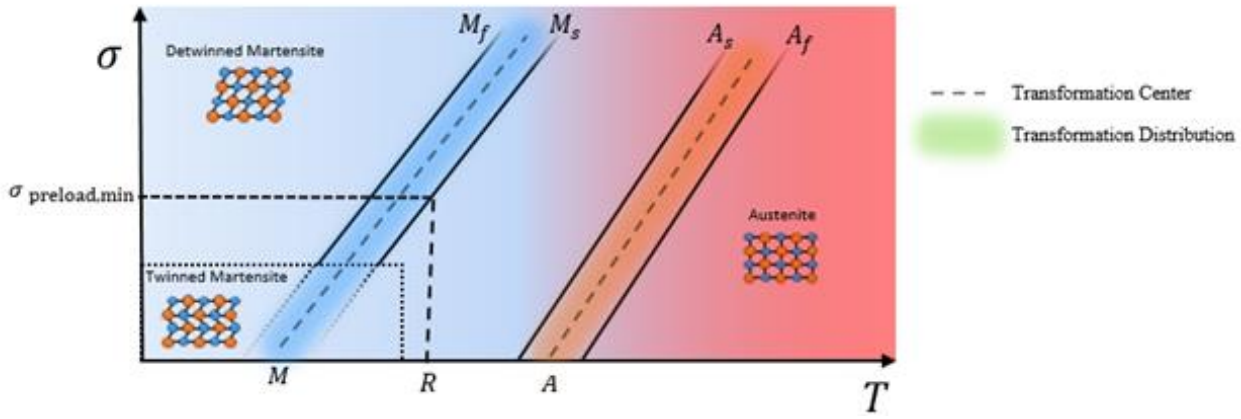

Figure 3. SMA Phase Diagram

Two bands of active transformation as shown in the phase diagram define the boundaries of the Austenite to Martensite transformation and vice versa. By either cooling the SMA or by applying external stress, the phase can be made to transform by crossing the Martensite (*M*) transformation band so long as a preload is applied so that the SMA operates above the critical preload stress. Similarly, by relieving stress or heating the phase crosses the Austenite (*A*) band.

These bands fall along the center of the transformation bands outlined by the A_s and A_f temperatures and the M_s and M_f temperatures. These parameters can be seen to be linear functions of the stress applied to the SMA. The slope of the lines formed by the *A* and *M* transformation bands are denoted C_A and C_M, respectively. The M crystal phase corresponds with an elongated wire that has a lower Young's modulus, while the A crystal phase corresponds with a contracted wire with a higher Young's modulus. The two transformation boundaries are separated by a large gap, where the entire piece of material can be a mixture of the two phases. The transformation bands themselves also do not coincide, and this gap in between the transformation bounds is the cause of hysteresis during cycling between the two transformation bounds. While Figure 3 provides a good illustration of a general phase plane for SMA, more precise modeling of the transformation stresses has been done for specific SMA alloys [16, 17].

When holding stress constant and cycling heat, an SMA wire expands and contracts with the *shape memory effect* (Figure 4,lower). By maintaining temperature moderately high and cycling stress, the SMA wire stretches and returns to its original length in what is termed the *super-elastic effect* (Figure 4, right). Both effects demonstrate the characteristic hysteresis of the material.

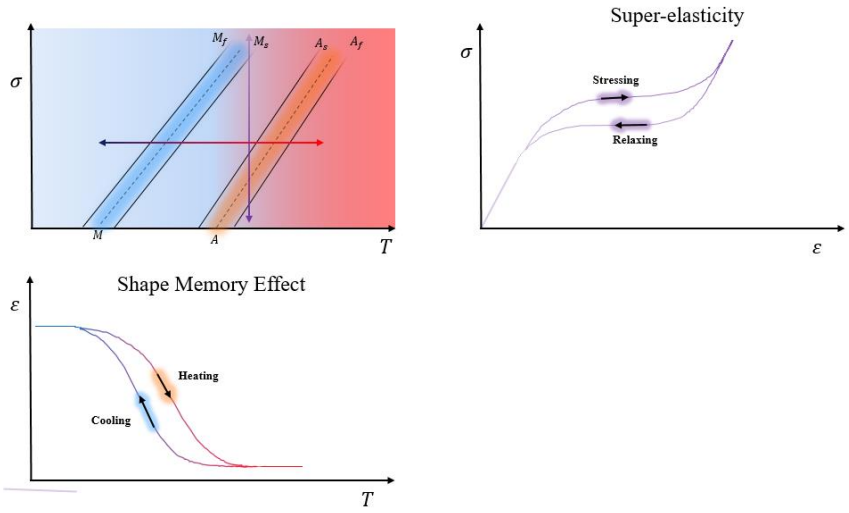

Figure 4. Shape-memory and super-elastic effects showing their relationship to motion on the phase diagram.

The earliest form of the mechanical model was created by Tanaka for super-elastic alloys [8], which is expressed in rate form as:

$$\dot{\sigma} = E(\xi)\dot{\varepsilon} + \theta(\xi)\dot{T} + \Omega(\xi)\dot{\xi} \tag{2.2.1}$$

This form identifies the stress (σ) on the actuator as a function of the strain (ε), the temperature (T), the coefficient of thermal expansion (θ), the transformation tensor (Ω), and the phase fraction (ξ). The consistency of this model was recognized by Liang and Rogers to only be upheld for a certain form of the transformation tensor [9], where:

$$\Omega(\xi) = -\varepsilon_L E(\xi) \tag{2.2.2}$$

This form identifies Ω as the stress associated with phase transformation neglecting applied stress from the mechanical system and ε_L the strain associated with phase transformation with no elastic deformation.

A different type of model was proposed by Ikuta where instead of looking at the problem from a thermodynamics perspective, the two crystalline phases could be viewed as springs in a parallel configuration in what is termed the Voigt model [10]:

$$\sigma = (1-\xi)\sigma_A + \xi\sigma_M = (E_A(1-\xi) + E_M\xi)\varepsilon \tag{2.2.3}$$

A similar model was purposed by Ivshin and Pence, which viewed the two phases as springs in a series configuration in what is termed the Reuss model [11]:

$$\varepsilon = (1-\xi)\varepsilon_A + \xi\varepsilon_M = \left(\frac{(1-\xi)}{E_A} + \frac{\xi}{E_M}\right)\sigma \tag{2.2.4}$$

Both the Voigt and Reuss models use E_A to denote the elastic modulus of the purely Austenite phase and E_M to denote the elastic modulus of the purely Martensite phase. A constitutive model that could be achieved by decomposing the overall strain into its components of elastic deformation, transformation strain, and thermal expansion was developed by Brinson and Huang [12], such that:

$$\varepsilon = \frac{\sigma}{E(\xi)} - \varepsilon_L E(\xi) + \frac{\theta(\xi)}{E(\xi)}(T_0 - T) \tag{2.2.5}$$

Eq. 2.2.5 is generally accepted in this literature as the constitutive model for the actuator strain, where the elastic modulus must be allowed to change as a function of the phase fraction in order for the model to be accurate. Representing a shape memory alloy as springs in parallel as per the Voigt model would yield an effective elastic modulus given by:

$$E = (1 - \xi)E_A + \xi E_M \tag{2.2.6}$$

In contrast, the Reuss model representation of the elastic modulus would have the elastic modulus expressed in the form:

$$E = \frac{(1 - \xi)}{E_A} + \frac{\xi}{E_M} \tag{2.2.7}$$

The specific model chosen has been shown by Gurley to have only a small impact on the system inside of the transformation region [13].

In the majority of cases, SMA actuators take the form of small diameter wires, so it is convenient to convert this intrinsic model to an actuator model using the wire diameter (d), cross sectional area (A_c) and wire length (L). The geometry is a function of the strain and Poisson's ratio (υ) of the material such that [14]:

$$L = L_0(1 + \epsilon) \tag{2.2.8}$$

$$d = d_0(1 - \upsilon\epsilon) \tag{2.2.9}$$

$$A_c = \frac{\pi}{4}d^2 \tag{2.2.10}$$

As a matter of convenience, the Poisson's ratio of both the Austenite and Martensite phases is taken to be the same with values varying from 0.3 to 0.33 [15]. However, experimental data has shown that this value is only an effective approximation of the Poisson's ratio, and that the

Poisson's ratio does vary from 0.3 for the B2 crystalline structure of Austenite and 0.41 for the B19' structure of Martensite [16, 17]. Denoting the different Poisson's ratios for the different phases υ_A and υ_M, respectively, the effective Poisson's ratio can be found as a function of the Martensite phase fraction using the Voigt model such that:

$$\upsilon = (1-\xi)\upsilon_A + \xi\upsilon_M \tag{2.2.11}$$

The spring rate and spring force are then given by using Eq. 2.2.11 from the Poisson's ratio, Eq. 2.2.10 for the cross-sectional area, Eq. 2.2.8 for the actuator length, and Eq. 2.2.6 for the elastic modulus and substituting them into the definition of the spring rate and spring force:

$$K_{SMA} = \frac{A_c E(\xi)}{L} = \frac{\pi\left[d_0\left(1-\left((1-\xi)\upsilon_A + \xi\upsilon_M\right)\epsilon\right)\right]^2\left[(1-\xi)E_A + \xi E_M\right]}{4L_0(1+\epsilon)} \tag{2.2.12}$$

$$F_{sma} = K_{SMA}(\epsilon - \epsilon_L\xi)L_0 = \frac{\pi(\epsilon-\epsilon_L\xi)\left[d_0\left(1-\left((1-\xi)\upsilon_A + \xi\upsilon_M\right)\epsilon\right)\right]^2\left[(1-\xi)E_A + \xi E_M\right]}{4(1+\epsilon)} \tag{2.2.13}$$

2.3 Electrical Modelling

As with most macroscopic properties of a shape memory alloy, the electrical resistivity changes with the phase fraction [18]. The electrical resistivity (ρ_e) has been modelled as a function of the phase fraction utilizing the Voigt model such that [19, 10]:

$$\rho_e = (1-\xi)\rho_A + \xi\rho_M \tag{2.3.1}$$

The electrical resistivities of the Austenite phase and Martensite phase are denoted ρ_A and ρ_M, respectively. These properties have a temperature dependence that can be adequately modelled as linear, which creates the form:

$$\rho_A = \rho_{A0} + \alpha_A(T - T_0) \tag{2.3.2}$$

$$\rho_M = \rho_{M0} + \alpha_M(T - T_0) \tag{2.3.3}$$

where T_0 is a reference temperature at which ρ_{M0} and ρ_{A0} are measured. A similar model that includes linear proportionality of resistivity to actuator stress has been proposed and is shown below with coefficients of proportionality β_A and β_M [4]:

$$\rho_A = \rho_{A0} + \alpha_A(T - T_0) + \beta_A\sigma \tag{2.3.4}$$

$$\rho_M = \rho_{M0} + \alpha_M(T - T_0) + \beta_M\sigma \tag{2.3.5}$$

The electrical resistivity can then be related to the actuator resistance by definition:

$$R = \frac{\rho_e L}{A_c} \tag{2.3.6}$$

The resistance as a function of known constants, initial geometry, actuator strain, and phase fraction is then found by substituting in Eq. 2.3.1 for the electric resistivity, Eq. 2.2.10 for the cross-sectional area, and Eq. 2.2.8 for the actuator length to yield:

$$R = \frac{\{(1-\xi)[\rho_{A0} + \alpha_A(T - T_0)] + \xi[\rho_{M0} + \alpha_M(T - T_0)]\}L_0(1+\epsilon)}{\frac{\pi}{4}\left[d_0\left(1 - \left((1-\xi)\upsilon_A + \xi\upsilon_M\right)\epsilon\right)\right]^{2^2}} \tag{2.3.7}$$

2.4 Phase Kinetics Modelling

Research into the phase kinetics of SMA has sought to explain how the Martensite phase fraction changes during the transformation period as a function of temperature and stress. The conditions for transformation are based on an interpretation of the phase diagram and determine when a transformation is going to occur. Several models exist that model the transformation conditions around the start and end transformation temperature [20, 11, 21]. However, some models exist that do not bound the conditions for transformation to within the start and finish temperatures. This is physically consistent with thermodynamics via the Clasius-Clapyron relationship [8], but it is not physically consistent with differential scanning calorimetry (DSC) experiments that show there is not a discontinuous start to transformation. This discrepancy can be reconciled if transformation temperatures are viewed as the endpoints of a distribution of a transformation region. If this assumption is used, the conditions of transformation are greatly simplified as they are only based on the directionality of the temperature and stress perpendicular to the transformation boundaries:

$$\text{if } \left\{ \begin{matrix} \dot{T} - \dfrac{\dot{\sigma}}{C_A} > 0 \\ \dot{T} - \dfrac{\dot{\sigma}}{C_M} < 0 \end{matrix} \right\} \quad \text{then } \left\{ \begin{matrix} \xi_{M \to A} \\ \xi_{A \to M} \end{matrix} \right\} \tag{2.4.1}$$

Models that explicitly bound themselves to within the transformation region are termed here as Class I models, whereas models that view transformation as a smooth distribution are termed here as Class II models.

During transformation, the Martensite phase fraction is typically modelled as a function of the distance travelled across transformation boundaries. These functions use parameters that relate

stress and temperature states within the transformation regions to the distance to the transformation boundaries. For Class I models, these take the form:

$$x^{I}{}_{A\to M} = -\frac{T - \frac{\sigma}{C_M} - M_s}{M_s - M_f} \tag{2.4.2a}$$

$$x^{I}{}_{M\to A} = -\frac{T - \frac{\sigma}{C_A} - A_f}{A_f - A_s} \tag{2.4.2b}$$

For Class II models, these parameters are based on the distance from the center bands of the distributions:

$$x^{II}{}_{A\to M} = K_M\left(T - \frac{\sigma}{C_M} - M\right) \tag{2.4.3a}$$

$$x^{II}{}_{M\to A} = K_A\left(T - \frac{\sigma}{C_A} - A\right) \tag{2.4.3b}$$

K_M and K_A and are fitting parameters from DSC experiments that determine the distribution of the transformation band.

Class II models can use any model in which the phase fraction is bounded between zero and one for all values of stress and temperature. Nearly all population growth models [22] can be used for fitting the phase fraction to these parameters. The most common model is the logistic function which is commonly used in population growth modeling, which can be written as [10, 23, 24]:

$$\xi_{M\to A} = \frac{\xi_M}{1 + \exp(x^{II}{}_{M\to A})} \tag{2.4.4a}$$

$$\xi_{A\to M} = \frac{1 - \xi_A}{1 + \exp(x^{II}{}_{M\to A})} + \xi_A \tag{2.4.4b}$$

Zotov expanded upon this model using X-Ray Power Diffractograms (XRD) and saw that the experimental data fit very well to the generalized logistics function (i.e. the Richards logistics function) such that the Martensite to Austenite transformation could be written as [25]:

$$\xi_{M\to A} = \frac{\xi_M}{(1+\nu_A \exp(x^{II}{}_{M\to A}))^{1/\nu_A}} \tag{2.4.5a}$$

The Austenite to Martensite transformation was then outlined by Gurley to be consistent with the previous exponential model [26]:

$$\xi_{A\to M} = \frac{1-\xi_A}{(1+\nu_M \exp(x^{II}{}_{A\to M}))^{1/\nu_M}} + \xi_A \tag{2.4.5b}$$

The parameters ν_A and ν_M can be solved from empirically gathered from DSC experiments. The Richards function simplifies to the original logistics function model when these two parameters are set equal to unity. This model has been shown to fit experimental data well [4, 5, 6, 7]. The parameters ξ_M and ξ_A are hysteresis parameters that store the values of the phase fraction as the transformation reverses direction such that for $\xi_{M\to A}$, $\xi_A = \xi$ and for $\xi_{A\to M}$, $\xi_M = \xi$. This is the model that is selected in this literature as it is continuously differentiable except when the transformation reverses direction and can account for partial transformations in the material. It is worth noting that empirical models relating ξ to temperature and stress have been developed experimentally by utilizing standard tensile testing and thermal cyclic testing for more precise modelling of various SMA alloys [27].

2.5 Analytical Heat Transfer Modelling

2.5.1 External Heating

SMA actuators undergo crystalline structure changes as energy is applied to or removed from the system in the form of heat or an applied stress. The heat applied to an SMA actuator is usually input via passing of electric current through the wire in robotics applications [28]. The amount of DC current (I) that passes through an SMA actuator is dictated by the resistance of the wire (Eq. 2.3.7) and the voltage across the actuator (ΔV) through Ohm's Law:

$$\Delta V = IR \tag{2.5.1.1}$$

This method of heating is known as Joule heating or Ohmic heating, and the total heating power provided by the electric current is given by:

$$P = \Delta V I = I^2 R = \frac{\Delta V^2}{R} \tag{2.5.1.2}$$

If the voltage and current vary as functions in time, such as with AC current, then the average power input can be given as:

$$P_{avg} = {I_{RMS}}^2 R \tag{2.5.1.3}$$

where I_{RMS} is the root mean squared value of the current with respect with time. It is worth noting that as the frequency of AC current increases, the current density gradually accumulates near the outer edges of a wire in what is known as the skin effect. This increases the resistance of the wire and as such, increases the heat generated within the wire (with the heat generation no longer being uniform, but instead gradually more and more localized towards the edges of the actuator).

Power can also be applied to a shape memory alloy by exposing it to an open flame, in which case the best analytical approach is to model the input power with the First Law of Thermodynamics and tabulated values regarding the heat of combustion of the ignited material:

$$P_{\text{combustion}} = \sum_p \dot{N}_p h_p - \sum_r \dot{N}_r h_r \tag{2.5.1.4}$$

where N_p and N_r are the number of moles of the combustion products and reactants, respectively, and h_p and h_r are the enthalpies of formation of the products and reactants, respectively.

If heat is applied via the application of a warmer working fluid, then the analytical approach is to model the heat input using the governing equations of convective heat transfer. If it is applied via thermal radiation such as in an oven, the analytical approach is to use the governing laws of radiative heat transfer as outlined in a later section.

2.5.2 Conductive Heat Transfer

Heat removal from the wire will occur via three means of heat transfer: conduction, convection, and radiation. Thermal conduction is the transfer of heat caused by microscopic collisions of particles inside of a body. These collisions transfer heat through the microscopic transfer of kinetic energy and potential energy, when summed are simply referred to as the internal energy of a body (*U*). Conduction of heat away from a wire actuator will occur primarily from the heated portion of the wire to the unheated portion of the wire that lies outside of where the wire is electrically connected. This effect causes a temperature gradient with noticeable boundary effects. The analytical approach to modelling thermal conduction stems from Fourier's Law, which states that the density of the heat transferred via conduction is given by:

$$q''_{cond} = -k\nabla T \tag{2.5.2.1}$$

k is the thermal conductivity of the SMA material and ∇T is the temperature gradient. When Fourier's Law is applied to a wire actuator, the temperature variance is most often modelled as lengthwise, and the rate of heat transfer is given by:

$$q_{cond} = -kA_c \frac{dT}{dx} \tag{2.5.2.2}$$

As with most macroscopic properties of an SMA, the thermal conductivity varies with the phase fraction. For example, the thermal conductivity of Martensitic nitinol (k_M) is typically given as 8.0 $\frac{\mathrm{W}}{\mathrm{mK}}$ and the thermal conductivity of Austenitic nitinol (k_A) is typically given as 18.0 $\frac{\mathrm{W}}{\mathrm{mK}}$ [15]. To maintain consistency, during transformation the thermal conductivity is said to use the Voigt model such that:

$$k = (1 - \xi)k_A + \xi k_M \tag{2.5.2.3}$$

For shape memory alloy wire actuators, thermal conduction leads to temperature gradients axially and radially along the wire. For ease of computation, it is often desirable to treat the actuator as a lumped capacitance that has a uniform temperature. This assumption grows increasingly inaccurate for shorter wires, where thermal boundary conditions become more prevalent. Research has been shown that for wire lengths above 148.8 mm this thermal boundary layer can safely be neglected [29].

2.5.3 Convective Heat Transfer

Convection is the transfer of heat to a fluid surrounding the system either through diffusion or through advection, where heat is carried away through bulk flow of the fluid. Forced convection is said to take place when advection is the dominant means of heat transfer, while natural convection is said to take place when diffusion of heat and buoyant forces are the primary means of carrying heat away from the system. Convective heat transfer is described by Newton's Law of Cooling such that:

$$q_{conv} = hA_s(T - T_{fluid}) \tag{2.5.3.1}$$

A_s denotes the surface area of the system that is exposed to the working fluid which is held at a temperature T_{fluid} when evaluated outside of the thermal boundary layer. h is the convective heat transfer coefficient, which is defined as:

$$h \equiv \frac{\overline{\mathrm{Nu}}_{L_C} k_{fluid}}{L_C} \tag{2.5.3.2}$$

k_{fluid} denotes the thermal conductivity of the working fluid evaluated at the film temperature (T_{film}), which is commonly evaluated as $\frac{T + T_{fluid}}{2}$. L_C denotes the characteristic length, which is an arbitrarily chosen length scale of the system. The characteristic length is, for many systems, generally chosen to be the volume of the body divided by its surface area. For cylinders, it is often convenient to have the diameter be the characteristic length. Nu_{L_C} denotes the Nusselt number, which is an empirically derived value based on the fluid properties. For a convection coefficient to apply over an entire surface, the surface averaged Nusselt number must be used. For SMA wire actuators, Eq. 2.5.3.2 becomes:

$$h = \frac{k_{fluid}\,\overline{\mathrm{Nu}_D}}{d} \tag{2.5.3.3}$$

An extensive set of empirical models have been developed in order to find the surface averaged Nusselt number for a cylinder in a cross-flow. These relationships typically give the surface

averaged Nusselt number as a function of two dimensionless parameters: the Prandtl number and the Reynolds number, defined by Eqs. 2.5.9 and 2.5.10, respectively.

$$\mathrm{Pr} \equiv \frac{\upsilon}{\alpha} = \frac{c_p \mu}{k} \tag{2.5.3.4}$$

$$\mathrm{Re}_D \equiv \frac{vd}{\upsilon} \tag{2.5.3.5}$$

υ is the fluid's kinematic viscosity, μ is the dynamic viscosity, c_p is the fluid's specific heat, α is the fluid's thermal diffusivity, d is the wire diameter, and v is the fluid velocity as it passed over the wire. These material properties can vary greatly depending on the temperature and pressure of the fluid. Because the Prandtl number, which is the ratio between momentum diffusivity and thermal diffusivity, only depends on the working fluid and the working fluid's state, it is often provided as a tabulated value for a fluid. The Reynolds' number, which is the ratio of inertial forces to viscous forces in a flow, always contains a length value as a scaling factor, and cannot be provided in a similar way.

These parameters can be quantified by acknowledging that the Prandtl number gives a measurement of how fast heat is transferred through a flowing material with respect to how fast mass is transferred. The Reynolds number quantifies whether the flow of the cooling fluid is laminar or turbulent. During actuation, fluid pressure can be assumed to be roughly constant at atmospheric pressure, so these fluid properties all become strong functions of temperature. For common fluids such as air or water, their values are tabulated for a variety of temperatures, and using interpolation methods, can reveal fairly accurate values for any temperature. For a cylinder in cross-flow, the onset of turbulence is caused by the presence of an adverse pressure gradient caused by increasing pressures along the cylinder surface as the flow passes over. The increase in

pressure is caused by either friction drag caused by friction with the cylinder surface, or the development of a wake.

An empirical correlation for the surface averaged Nusselt number due to Hilpert that has been modified to account for fluids of various Prandtl numbers is widely used for $\mathrm{Pr} \geq 0.7$ [30]:

$$\overline{\mathrm{Nu}_D} = C\mathrm{Re}_D{}^m \mathrm{Pr}^{1/3} \tag{2.5.3.6}$$

The constants in this equation are given in Table 1 for various ranges of Reynolds numbers:

Table 1. Constants of Eq. 2.5.11 for a circular cylinder in a cross-flow

$\mathbf{Re}_D$	C	m
0.4-4	0.989	0.330
4-40	0.911	0.385
40-4,000	0.683	0.466
4,000-40,000	0.193	0.618
40,000-400,000	0.027	0.805

Another correlation was developed by Zukauskas [31] gives that for $0.7 \leq \mathrm{Pr} \leq 500$ and $1 \leq \mathrm{Re}_D \leq 10^6$:

$$\overline{\mathrm{Nu}_D} = C\mathrm{Re}_D{}^m \mathrm{Pr}^n \left(\frac{\mathrm{Pr}}{\mathrm{Pr}_s}\right) \tag{2.5.3.7}$$

All properties are evaluated at the fluid temperature except for Pr_s, which is the Prandtl number evaluated at the surface temperature of the cylinder. The constants *C* and *m* for this correlation are given in Table 5. The constant n is given by

$$n = \begin{cases} 0.37, & \mathrm{Pr} \leq 10 \\ 0.36, & \mathrm{Pr} > 10 \end{cases} \tag{2.5.3.8}$$

Table 2. Constants of Eq. 2.5.3.8 for a circular cylinder in a cross-flow

$\mathbf{Re_D}$	C	m
1-40	0.75	0.4
40-1,000	0.51	0.5
1,000-20,000	0.26	0.6
20,000-1,000,000	0.076	0.7

One of the more widely used and accurate models is the Churchill-Bernstein relationship, typically considered valid for values of the product $\mathrm{Re}_D\mathrm{Pr}$ greater than or equal to 0.2 [32]:

$$\overline{\mathrm{Nu}_D} = 0.3 + \frac{0.62{\mathrm{Re}_D}^{1/2}\mathrm{Pr}^{1/3}}{\left[1 + \left(\frac{0.4}{\mathrm{Pr}}\right)^{2/3}\right]^{1/4}}\left[1 + \left(\frac{\mathrm{Re}_D}{282000}\right)^{5/8}\right]^{4/5} \tag{2.5.3.9}$$

The Churchill-Bernstein relationship uses all properties evaluated at film temperature and is popular because it is a single comprehensive equation and not a piecewise function. However, the relationship only promises up to 20% error when computing the heat transfer coefficient due to the averaging of the surface temperature, which in reality varies circumferentially as well as axially, as well as uncertainties associated with measuring the velocity of the air.

For very low air velocities (or still air), the Churchill-Bernstein relationship fails to accurately capture the Nusselt number because natural convection is the predominant mode of heat transfer rather than forced convection. For an isothermal cylinder undergoing free convection, Morgan suggests that the Nusselt number can be computed from [33]:

$$\overline{\mathrm{Nu}_D} = C{\mathrm{Ra}_D}^n \tag{2.5.3.10}$$

Ra denotes the Rayleigh number, defined as:

$$\mathrm{Ra}_D \equiv \mathrm{Pr}\left(\frac{d^3 g\Delta T\beta}{\upsilon^2}\right) \tag{2.5.3.11}$$

Table 3. Constants of Eq. 2.5.3.10 for an isothermal circular cylinder in free convection

$\mathbf{Ra_D}$	C	n
$\mathbf{10^{-10} – 10^{-2}}$	0.675	0.058
$\mathbf{10^{-2} – 10^{2}}$	1.02	0.148
$\mathbf{10^{2} – 10^{4}}$	0.850	0.188
$\mathbf{10^{4} – 10^{7}}$	0.480	0.250
$\mathbf{10^{7} – 10^{12}}$	0.125	0.333

To avoid the use of a piecewise function, Churchill and Chu provided a single formula for the wide range of $\mathrm{Ra}_D \leq 10^{12}$ [34, p. 18]:

$$\overline{\mathrm{Nu}_D} = \left\{ 0.6 + \frac{0.387\mathrm{Ra}_D{}^{1/6}}{\left[1 + \left(\frac{0.559}{\mathrm{Pr}}\right)^{9/16}\right]^{8/27}} \right\}^2 \tag{2.5.3.12}$$

g denotes the acceleration due to gravity and β represents the expansion coefficient, which is also a function of temperature and is generally tabulated for common working fluids. The empirical relationship for vertical cylinders is noticeably similar, being given by the following relationship for certain cases where the diameter satisfies the criteria $d > \frac{35L}{(\frac{\mathrm{Ra}}{\mathrm{Pr}})^{1/4}}$ [34, p. 19]:

$$\overline{\mathrm{Nu}_D} = \left\{ 0.825 + \frac{0.387\mathrm{Ra}^{1/6}}{\left[1 + \left(\frac{0.492}{\mathrm{Pr}}\right)^{9/16}\right]^{8/27}} \right\}^2 \tag{2.5.3.13}$$

Eq. 2.5.3.13 is often called the thick cylinder limit because it only holds when the thermal boundary layer thickness is lower than the diameter of the wire such that the natural convection can be treated as if it is passing over a flat plate. Because this is oftentimes not the case for thin wire actuators, a relationship was formulated such that [35]:

$$\overline{\mathrm{Nu}_L} = \frac{4}{3}\left[\frac{7\mathrm{Ra_L Pr}}{5(20+21\mathrm{Pr})}\right]^{1/4} + \frac{4(272+315\mathrm{Pr})\mathrm{L}}{35(64+63\mathrm{Pr})\mathrm{D}} \quad (2.5.3.14)$$

This formulation is unique when compared to the others because the characteristic length becomes the actuator length. This changes the definition of the convection coefficient so that it is defined in accordance to the actuator length instead of the actuator diameter.

For higher levels of accuracy, tabulated values of the local and surface averaged Nusselt numbers for several types of boundary conditions for vertical, slender rods have been formulated by Cebeci [36] and Sparrow [37]. Worth noting is the fact that in general, convective heat transfer is greater for vertically oriented wires than for horizontally oriented wires. This is due to the fact that horizontal wires impede the ability of air to rise and carry away heat.

2.5.4 Radiative Heat Transfer

Thermal radiation is electromagnetic radiation given off by all bodies that have a temperature above absolute zero. This is caused by charged particles accelerating or magnetic dipoles being moved during collision of these particles. The Stefan-Boltzmann equation states that radiative heat transfer between an object and its surroundings can be described when the temperatures are denoted in Kelvin by:

$$q_{rad} = \epsilon \sigma_b A_s (T^4 - {T_\infty}^4) \tag{2.5.4.1}$$

σ_b denotes the Stefan-Boltzmann constant and T_∞ denotes the temperature of the surroundings. ϵ is the object's emissivity, which is a unitless parameter bounded between zero and one that reflects how effective a surface is at emitting energy. The value of the emissivity of a shape memory alloy is dependent on the material composition, surface finish, temperature, and geometry. Experimentally determined values for the emissivity for nickel titanium alloys have varied from values of 0.66 to 0.83 [38, 39].

Because radiation provides an inherent nonlinearity by definition, efforts to linearize radiative heat transfer so that it fits a similar form as convective heat transfer have been established, which leads to the definition of the radiative heat transfer coefficient, given by:

$$h_{rad} = \epsilon \sigma_b ({T^2 + T_\infty}^2)(T + T_\infty) \tag{2.5.4.2}$$

The linearized form of the radiative heat transfer equation is given by incorporating Eq. 2.5.4.1 into Eq. 2.5.4.2 and making assumptions regarding the average temperature T inside of the radiative heat transfer coefficient:

$$q_{rad} \approx h_{rad} A_s (T - T_\infty) \tag{2.5.4.3}$$

2.5.5 Latent Heat of Transformation

As an SMA undergoes a crystalline structure change, there is energy absorbed or released over the course of the phase transformation. This energy is termed the latent heat of transformation and is denoted in energy per unit mass form, called the specific latent heat, as ΔH. Whereas the mechanisms of energy input and output reviewed thus far result in a direct change in the temperature of a material and are for this reason sometimes referred to as sources of *sensible heat*, *latent heat* is energy utilized only for the change in phase and is a constant temperature process. For nickel titanium, a typical value of the latent heat of transformation is -24.2 $\frac{\text{J}}{\text{g}}$ [40]. The power absorbed or released by the system during transformation is then given by:

$$q_{\Delta H} = m\Delta H\dot{\xi} \tag{2.5.5.1}$$

The latent heat of transformation is often neglected because it causes a nonlinearity in the analytical analyses that cannot be resolved. However, in most simulations it is not a negligible quantity as it inputs a significant amount of power to slow the heating and cooling response. It is also worth noting that even if the actuator is contained in an otherwise adiabatic enclosure, that mechanically inducing a phase transformation will work to cycle the actuator temperature. The temperature change in the adiabatic case can be found as:

$$\Delta T_{adiabatic} = \frac{\Delta H}{c_p} \tag{2.5.5.2}$$

The potential significance of neglecting the latent heat of transformation in simulation with shape memory alloys is displayed in a comparison of the heating response of a five-centimeter-long, 0.125 mm in diameter nickel titanium wire at constant load with the ambient temperature being held at twenty degrees Celsius (Figure 5).

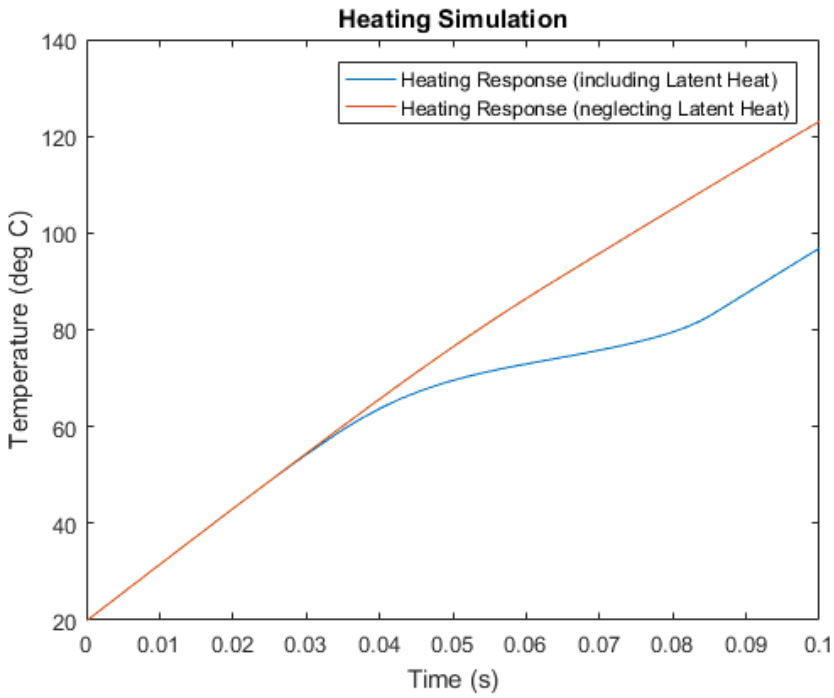

Figure 5. Simulation of Heating Response with and without Latent Heat (3.7 V applied to 5 cm span of 0.125 mm diameter NiTi wire at room temperature)

The latent heat of transformation provides an endothermic reaction within the actuator upon heating that impedes the heating of the actuator and provides an exothermic reaction upon cooling that impedes the cooling in the actuator. The steady state temperature is unaffected by these reactions, but the transient response is significantly affected.

2.5.6 First Law of Thermodynamics

The First Law of Thermodynamics is a statement of the conservation of energy in terms of the energy of a control system. The law states that the total change of the internal energy of the system is equal to the energy input into the system subtracted by the work done by the system. The various mechanisms of how energy can be input (or lost) from the system comprised of an SMA actuator have been covered, but no expression for the work done by the system has been developed in the energy balance. The mechanical power output of an SMA actuator can be readily modelled by recognizing the in a thermodynamical analysis, the work done by a system to its surroundings is given for some system pressure φ and volume Λ:

$$W = \varphi \Delta \Lambda \tag{2.5.6.1}$$

This expression is readily expressed in rate form through the use of differentials:

$$\dot{W} = \varphi \frac{d\Lambda}{dt} \tag{2.5.6.2}$$

For the shape memory actuator, the pressure and volume can be described by:

$$\varphi = \sigma A_c \tag{2.5.6.3}$$

$$\Lambda = A_c L \tag{2.5.6.4}$$

If the work done by the system is only accomplished through a phase transformation in the material, then it is often a decent assumption to state that the stress is a near constant value during the transformation because the preload stress causes the change in material stress due to the mechanical system to be negligible. In these situations, the power output of the SMA actuator is simply given by the term called the *plasticity* in literature [41]:

$$\dot{W} = \varphi \frac{d\Lambda}{dt} = \sigma A_c \frac{d(A_c L)}{dt} = \sigma A_c L \varepsilon_L \dot{\xi} \tag{2.5.6.5}$$

This type of formulation must also consider the cross-sectional area to be a constant value, thus neglecting the radial Poisson expansion that takes place during wire contraction. For a control volume made up of an SMA material heated by an electric current, the First Law of Thermodynamics then yields:

$$\frac{dU}{dt} = P - q_{conv} - q_{rad} - q_{cond} - q_{\Delta H} - \dot{W} \tag{2.5.6.6}$$

Decomposing this conservation of energy relation into its constitutive expressions and rearranging terms yields:

$$m\left(c_p \frac{\partial T}{\partial t} + \Delta H \dot{\xi}\right) = I^2 R(\xi) - hA_s(T - T_{fluid}) - \epsilon\sigma_b A_s(T^4 - T_\infty{}^4) - kA_c\left[\frac{\partial T}{\partial x}\right]_b + \sigma A_c \varepsilon_L L \dot{\xi} \tag{2.5.6.7}$$

where $\left[\frac{\partial T}{\partial x}\right]_b$ represents the temperature derivative with respect to temperature at the boundaries of the control volume. Radial variations in temperature tend to be neglected, but in cases where they are significant the analytical solutions to transient radial conduction problems with a convection boundary condition have a closed form for a constant initial temperature T_i [42]:

$$T(r,t) = T_\infty + \frac{2}{b}(T_i - T_\infty) \sum_{m=1}^{\infty} \frac{1}{\beta_m} \frac{J_1(\beta_m b) J_0(\beta_m r)}{J_0{}^2(\beta_m b) + J_1{}^2(\beta_m b)} e^{-\beta_m{}^2 \alpha t} \tag{2.5.6.8}$$

where J_0 denotes the Bessel function of the zeroth kind, J_1 denotes the Bessel function of the first kind, b represents the wire diameter, α represents the thermal diffusivity of the material, T_∞ represents the ambient temperature, and β_m represents the solutions of the transcendental equation given by:

$$\beta b J_1(\beta b) - \mathrm{Bi} J_0(\beta b) = 0 \tag{2.5.6.9}$$

where Bi is the Biot number for the problem. Due to the complexity of this solution, numerical methods are typically used for transient analysis of multidimensional problems and as such, the equation of the form Eq. 2.5.6.9 is generally not pursued here.

2.6 Discretized Heat Transfer Modelling

Because analytical approaches to modelling the thermal response of shape memory alloys fail to capture nonlinearities present when including radiation or the latent heat of transformation, and provide nontrivial closed form solutions when accounting for temperature variance along the length of the actuator, numerical methods have been researched for the analysis of the shape memory actuators. One of the more prevalent means to numerically derive solutions to the conservation of energy relations is to discretize the system into control volumes centered at nodes and to solve for the temperature of those nodes with a finite difference scheme, which takes partial differential equations and approximates them with difference equations [43]. The governing equation behind the diffusion of heat through the actuator, for example, is the one dimensional heat equation:

$$\frac{\partial T}{\partial t} = \alpha \frac{\partial^2 T}{\partial x^2} \tag{2.6.1}$$

where α is the thermal diffusivity of the medium. The second partial derivative of temperature with respect to position can be approximated for uniform grid spacing Δx and node position index *i* using the central difference method, which is accurate to $O(\Delta x^2)$:

$$\frac{\partial^2 T}{\partial x^2} \approx \frac{T_{i+1} - 2T_i + T_{i-1}}{\Delta x^2} \tag{2.6.2}$$

The first derivative of temperature with respect to time can be approximated with a first order numerical derivative that is forward in time using the forward difference method. For a time step of Δt and time index ℓ this yields:

$$\frac{\partial T}{\partial t} \approx \frac{T_i^{\ell+1} - T_i^{\ell}}{\Delta t} \tag{2.6.3}$$

There is no information given in these approximations for at what point in time that Eq. 2.6.2 should be evaluated. To account for all possibilities, a weighting factor γ that varies from zero to one can be introduced such that:

$$\frac{\partial^2 T}{\partial x^2} \approx \gamma \frac{T_{i+1}^{\ell+1} - 2T_i^{\ell+1} + T_{i-1}^{\ell+1}}{\Delta x^2} + (1-\gamma)\frac{T_{i+1}^{\ell} - 2T_i^{\ell} + T_{i-1}^{\ell}}{\Delta x^2} \tag{2.6.4}$$

For $\gamma = 1$, this approximation is forward in time and yields the Forward Time Centered Space (FTCS) scheme:

$$\frac{T_i^{\ell+1} - T_i^{\ell}}{\Delta t} = \alpha \frac{T^{\ell}{}_{i+1} - 2T^{\ell}{}_{i} + T^{\ell}{}_{i-1}}{\Delta x^2} \tag{2.6.5}$$

The discretized Fourier number is very convenient to introduce such that $\mathrm{Fo} = \frac{\Delta t}{\alpha \Delta x}$ and Eq. 2.6.4 simplifies to an explicit recurrence relation:

$$T_i^{\ell+1} = (1 - 2\mathrm{Fo})T_i^{\ell} + \mathrm{Fo}\left(T^{\ell}{}_{i+1} + T^{\ell}{}_{i-1}\right) \tag{2.6.6}$$

A well-known instability exists with this scheme in that for $\mathrm{Fo} > \frac{1}{2}$ the scheme is oscillatory and divergent due to the first coefficient in the expression.

For $\gamma = 0$, this approximation is backwards in time and yields the Backwards Time Centered Space (BTCS) scheme which can be algebraically manipulated to yield:

$$(1 + 2\mathrm{Fo})T_i^{\ell+1} - \mathrm{Fo}\left(T_{i+1}^{\ell+1} + T_{i-1}^{\ell+1}\right) = T_i^{\ell} \tag{2.6.7}$$

This scheme is implicit and always converges to a stable solution. Because it is an implicit scheme, the entire system of equations presented in Eq. 2.6.5 must be solved simultaneously, greatly increasing the computation time.

For $\gamma = \frac{1}{2}$, this approximation is centered in time and is called the Crank-Nicholson method, which is always stable but can be subject to numerical oscillations. The Crank-Nicholson method is second order accurate in time as well as space.

The heat equation can be easily appended with terms that allow for the inclusion of convection and radiation as well as volumetric heat generation (such as Ohmic heating and the latent heat of transformation), such that:

$$\rho c_p \frac{\partial T}{\partial t} = k \frac{\partial^2 T}{\partial x^2} - \frac{4h}{d}(T - T_\infty) - \frac{4\epsilon\sigma_b}{d}\left(T^4 - {T_\infty}^4\right) + \frac{4I^2R + m\Delta H\dot{\xi}}{\pi d^2 L} \tag{2.6.8}$$

Because the macroscopic property of thermal conductivity of each control volume depends on its phase composition, the discretized schemes become much more complicated because the conductivity must be allowed to vary throughout the entire material. Because properties such as the diameter and wire resistance is dependent on the kinetics and the mechanical model, each portion of the modelling must be coupled during each time step and to guarantee the stability of the solution, an implicit formulation must be crafted. For multidimensional problems, the same solution process can be followed and the results superimposed on one another.

Significant amounts of research have gone into modelling shape memory alloy actuators using finite difference schemes [44]. Huang developed a FDM scheme for lengthwise and radial conduction using the Crank-Nicholson method and allowed for varying thermal conductivities for a cooling response neglecting latent heat effects and the variation of material geometry [45]. Mirzaeifar presented an explicit first order forward-difference FDM scheme when analyzing radial conduction in actuators with uniaxial tension that accounted for latent heat effects that assumed constant material properties during phase transformation [46].

2.7 Wire Actuator Bandwidth

Because SMA actuators frequently use convection with still air at room temperature to transform from Austenite to Martensite, the transformation time is slow. This is well known as one of the biggest drawbacks of using a shape memory alloy actuator, and research has gone into empirically characterizing the system bandwidth for several situations. SMA actuators that cool down using still, ambient air typically have low bandwidths, often below 1 Hz. Because of these characteristically low bandwidths, care has to be taken to design a controller that will not operate so fast as to attenuate the system response [47]. This knowledge of the system bandwidth and how it changes with the wire diameter can also help a designer select the appropriate diameter wire for the actuator in a variety of automated mechanical systems.

A variety of methods exist to raise this bandwidth into the range of 10 Hz to 20 Hz through the use of multiple actuators in agonist-antagonist pairs [48, 49, 50, 51, 52, 53]. An analysis of force tracking control was performed and displayed a system bandwidth of an SMA actuator of approximately 2 Hz [54]. An analysis of a robotic grip using a NiTi actuator using a H_∞ control scheme revealed a system bandwidth of 0.48 Hz [55]. An anti-slack, rapid-heating, anti-overload differential PID control scheme acting on an antagonist pair of SMA actuators showed the ability to get 2 Hz tracking bandwidths [56, 57]. A neural network feedforward control scheme acting on an SMA actuator with an antagonist spring achieved a bandwidth of only 0.1 Hz [58]. Several takes on self-sensing with SMA actuators have been used in control schemes, yielding bandwidths between 0.15 Hz and 1 Hz [59, 60, 61]. An analysis on the frequency response of several SMA actuators of different diameters showed in detail how these actuators perform at frequencies ranging from 0.1 Hz to 100 Hz [62]. The system bandwidth of an SMA actuator has been shown

to increase as the wire diameter decreases for passively cooled systems, because the rate at which energy is transferred away from the wire is the limiting factor to system bandwidth [63].

2.8 Temperature Measurement

Because shape memory actuators are most commonly found as wire actuators of small diameters, direct measurement of temperature for characterization in experiment has proved a difficult task. Temperature measurements with IR sensors are usually distorted because the wire takes up a small field of view of the IR sensor, which averages the temperature of everything inside of its field of view. Likewise, direct measurement of the temperature with devices such as thermistors, RTDs, or a thermocouple can prove difficult because the temperature measurement device must be small enough to only attach to the wire actuator and not distort the temperature of the wire actuator via thermal conduction into the device. Particular interest has been paid to the use of small thermocouple probes due to their low cost and robustness.

Analytical approaches to the modelling of the errors encountered by probing a shape memory alloy with a thermocouple have been done by treating the thermocouple as a long, cylindrical fin [64]. Because the thermocouple by design consists of two metallic wires, often of the same diameter, an effective diameter of the thermocouple is typically denoted in the literature such that for metallic wire diameters d_1 and d_2 the effective thermocouple diameter is:

$$d_{eff} = d_1\sqrt{2} = d_2\sqrt{2} \tag{2.8.1}$$

The localized loss of heat via conduction to the thermocouple has been modelled as infinitely long fin such that:

$$Q = \sqrt{kA_c hP}(T_b - T_\infty) \tag{2.8.2}$$

Analytical solutions that account for this loss of heat are possible for simplified situations such as when the shape memory actuator is considered adiabatic except for the heat loss to the

thermocouple and the SMA actuator is considered a semi-infinite body [65]. Other approaches have tended towards numerical analysis such as through FEM [64].

2.8 Multibody Dynamics Software and Numerical Simulation

Multibody dynamic (MBD) systems consist of solid bodies, or links, that are connected to each other by joints that restrict their relative motion. The study of MBD is the analysis of how a system comprised of defined constraints (in the form of joints and prescribed motions between interconnected rigid or flexible bodies), move under the influence of forces [66]. Software packages such as ADAMS (Automated Dynamic Analysis of Mechanical Systems), DADS [67], COMSOL [68], ANSYS Rigid Body Dynamics [69] , and others enable these systems to recreate the dynamics of a wide variety of controlled systems with actuators such as electric motors or pneumatics. User-written subroutines and function expressions can be used to develop custom modules that work to recreate more complex interactions between sensors, shape memory actuators, and control laws that are not readily available in the program such as a mathematical model of the behavior of a shape memory alloy. Once these modules are created, it becomes much simpler to implement the actuator into complex multibody mechanical systems with multiple links and joints. A multibody dynamics model was created for use in COMSOL to model the actuation of an end effector for a deployable system that would be used to collect small body samples from other planets, but this model was limited in scope because it failed to work for situations where the stress profile changed during operation [70].

Shape memory actuator models have been created and used in finite element analysis software simulations. Examples include micro-actuators working as a regulator valve in passing fluid flow [71], using an exponential model for general SMA behavior [8], and modelling a shape memory actuator in non-isothermal loading in ANSYS using a partial differential equation method [72].

Because the relationships that dictate the behavior of SMA actuators are highly nonlinear, accurate simulation of these actuators in actual dynamic systems is difficult and requires the storage of many parameters that vary over time. One of the biggest benefits to using a program like MSC ADAMS is the presence of accurate, easy to use, variable order and variable time step integrators suited for solving stiff differential equations. Two of the most prominent of these integrators are termed the GSTIFF integrator, developed by C.W. Gear, and the WSTIFF integrator. GSTIFF and WSTIFF are similar in formulation and behavior in that both use a backwards difference formulation. The main difference between the two is that the GSTIFF coefficients are calculated assuming a constant step size, whereas WSTIFF coefficients are a function of the step size. If the step size changes suddenly during integration, GSTIFF introduces a small error, while WSTIFF can handle step size changes without loss of accuracy. Sudden step size changes occur whenever there are discontinuous forces, discontinuous motions or abrupt events such as contact in the model.

Chapter 3: Heat Transfer Analysis

3.1 Analytical Analysis and Approximate Solutions

3.1.1 Analytically Derived Temperature Response

The lumped capacitance heat transfer model of a constant cross-section SMA wire undergoing Ohmic heating from an electrical power source and cooling via convection from the surrounding air is typically given in the following form, which neglects radiation and conduction:

$$m\left(c_p\frac{dT}{dt}+\Delta H\dot{\xi}\right)=I^2R(\xi)-hA_s(T-T_\infty) \tag{3.1.1.1}$$

If the SMA actuator cannot be considered to be of uniform temperature, a more complicated model can be invoked with the remaining assumption that radial conduction is negligible:

$$m\left(c_p\frac{\partial T}{\partial t}+\Delta H\frac{\partial \xi}{\partial t}\right)-k\frac{\partial^2 T}{\partial x^2}=I^2R(\xi)-hA_s(T-T_\infty) \tag{3.1.1.2}$$

These models can be simplified by making some significant assumptions regarding the convection coefficient, *h*. The $\Delta H\dot{\xi}$ term in the formulation represents the specific latent heat of transformation from one crystalline phase to another, which is often an ignored quantity so that the models become linear. However, a shape memory alloy such as nickel titanium will have a latent heat of transformation of roughly 24.2 Joules per gram, which is generally a non-negligible quantity [40]. The simplest analytical solution emerges when this quantity is neglected, the wire is assumed to be at uniform temperature, boundary effects are neglected. The assumption that the wire can be treated as uniform in temperature radially has been shown to typically match experimental results for wires with Biot numbers smaller than 0.1 where the Biot number is defined as:

$$\mathrm{Bi}=\frac{hd}{2k} \tag{3.1.1.3}$$

One consideration to note is that for shorter wire lengths, there will be thermal boundary effects to take into account that will prevent the wire from being at a uniform temperature. These boundary effects will also be neglected in the analysis, as it has been shown that for wire lengths above 148.8 mm this thermal boundary layer can safely be neglected [73]. These assumptions lead to the homogeneous form of the heat transfer equation:

$$mc_p \frac{dT}{dt} + hA_s T = I^2 R(\xi) + hA_s T_\infty \tag{3.1.1.4}$$

This takes the form of a simple ordinary linear first order differential equation and can be rewritten into the following form to reveal the time constant:

$$\frac{dT}{dt} + \left(\frac{hA_s}{mc_p}\right) T = \frac{I^2 R(\xi)}{mc_p} + \left(\frac{hA_s}{mc_p}\right) T_\infty \tag{3.1.1.5}$$

Because the SMA wire can be considered as having a uniform cross-sectional area throughout its length, the surface area available for convection (A_s) and the wire mass (m) can be expressed as a function of wire diameter (d) and wire length (L):

$$A_s = \pi dL \text{ and } m = \rho\pi \left(\frac{d}{2}\right)^2 L \tag{3.1.1.6}$$

ρ denotes the wire's volumetric density. Substituting these values into Eq. 3.1.1.5 allows the heat transfer model to take the following form:

$$\frac{dT}{dt} + \left(\frac{4h\pi dL}{\rho\pi L d^2 c_p}\right) T = \frac{4I^2 R(\xi)}{\rho\pi L d^2 c_p} + \left(\frac{4h\pi dL}{\rho\pi L d^2 c_p}\right) T_\infty \tag{3.1.1.7}$$

The solution to this differential equation, with the initial condition that the wire starts at a uniform temperature of T_0 takes the following form:

$$T(t) = T_\infty + \frac{I^2R}{h\pi dL} + \left(T_0 - T_\infty - \frac{I^2R}{h\pi dL}\right) e^{-\left(\frac{4h}{\rho d c_p}\right)t} \quad (3.1.1.8)$$

The basic observation are that the larger the diameter wire, the longer it takes to both heat and cool the system, and that the cooling response allows the wire temperature to exponentially decay to room temperature, with the response being independent of the length of the wire due to neglecting lengthwise variation in the temperature profile (Figure 6).

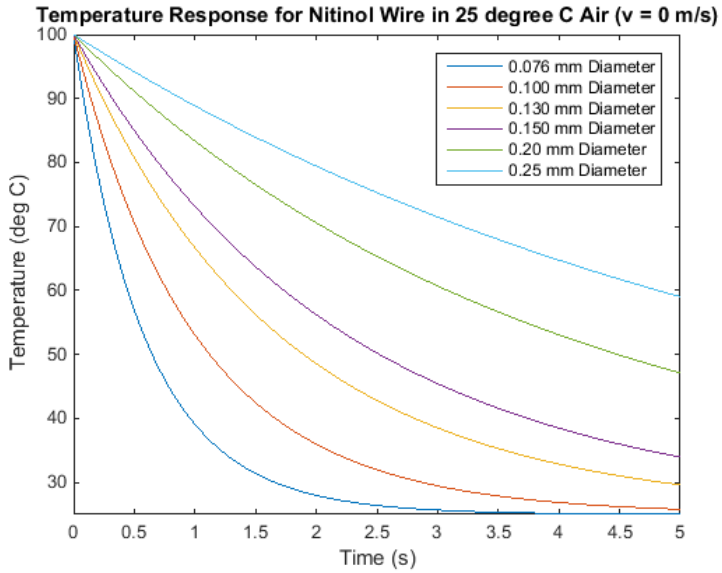

Figure 6. Cooling Response from Analytical Solution

An analytical solution can also be found for the case where the wire is not treated as a uniform temperature lengthwise, therein allowing for boundary effects to be accounted for. By assuming the initial conditions of the wire can fit a linear distribution plus an infinite sum of sinusoids of varying amplitude and frequency, the closed form solution of this equation is found to be [27]:

$$T(t,x) = \sum_{n=1}^{\infty} \frac{4}{B_1 n\pi} \int_0^t e^{\left(B_2 - \left(\frac{n\pi}{L}\right)^2\right)\frac{t-\tau}{B_1}} \left[Q(\tau) - B_2 T_0 - B_1 \frac{dT_1}{d\tau} + B_2 T_1(\tau) \right] \sin\left(\frac{n\pi x}{L}\right) d\tau + \sum_{n=1}^{\infty} (-1)^{n+1} \frac{2}{B_1 n\pi} \int_0^t e^{\left(B_2 - \left(\frac{n\pi}{L}\right)^2\right)\frac{t-\tau}{B_1}} \left[B_1 \left(\frac{dT_2}{d\tau} - \frac{dT_1}{d\tau} \right) - B_2 (T_2(\tau) - T_1(\tau)) \right] \sin\left(\frac{n\pi x}{L}\right) d\tau + T_1(t) + \left(\frac{x}{L}\right)[T_2(t) - T_1(t)] + \sum_{n=1}^{\infty} \left[a_n \sin\left(\frac{n\pi x}{L}\right) \right] e^{\left(B_2 - \left(\frac{n\pi}{L}\right)^2\right)\frac{t}{B_1}} \quad (3.1.9)$$

where $Q(\tau) = \frac{4I^2R}{kL\pi d^2}, B_1 = \frac{\rho c_p}{k}, B_2 = -\frac{hL}{\pi dLk}$

For temperature function $u_i(t,x)$ being one of the solutions to the partial differential equation presented in Eq. 3.1.1.2 that necessarily satisfies the boundary conditions but not the initial conditions (only the infinite sum of all solutions can satisfy the initial conditions in most cases), the cooling response of this form will have the following appearance [74]:

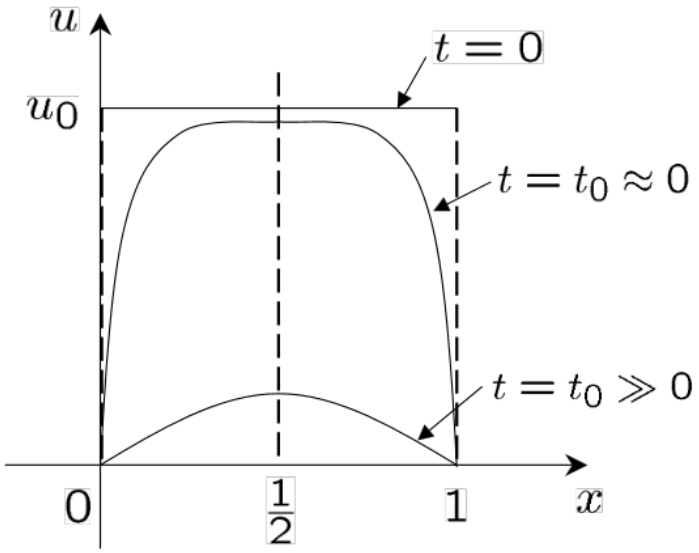

Figure 7. Cooling Response from Analytical Solution with Boundary Effects [74]

3.1.2 Convective Heat Transfer Coefficient

Both analytical solutions are only as accurate as the approximation of the heat transfer coefficient. Utilizing the Nusselt number relationships established in Chapter 2, the convection coefficient can be computed for a wire in still air for a variety of wire diameters and temperatures:

Table 4. Convection Coefficients in $\frac{\mathbf{W}}{\mathbf{m^2K}}$

Convection Coefficient						
	Wire Temperature relative to Ambient Air					
Diameter (mm)	**10°C**	**20°C**	**30°C**	**40°C**	**50°C**	**60°C**
0.050	234.94	243.61	250.10	255.63	260.59	265.18
0.075	164.21	171.04	176.04	180.23	183.96	187.37
0.125	105.97	111.11	114.79	117.82	120.47	122.87
0.250	60.17	63.79	66.31	68.30	70.08	71.64
0.300	52.18	55.50	57.80	59.64	61.21	62.61
0.375	44.00	47.00	49.06	50.70	52.10	53.33
0.500	35.56	38.20	40.01	41.44	42.64	43.70

Utilizing the empirical relations for the surface averaged Nusselt number, a rough approximation for the heat transfer coefficient for use in the analytical solutions can be obtained for cases where natural convection with air as the working fluid is the dominant means of heat transfer. This approximation can be presented as a function of the wire diameter in millimeters, wire temperature in degrees Celsius (or Kelvin), and fluid temperature in degrees Celsius (or Kelvin) from fitting the data [75]:

$$h(T,\ T_\infty, d) = \frac{14.6(T - T_\infty)^{\frac{1}{8}}}{d^{-4/5}} \left[\frac{\mathrm{W}}{\mathrm{m^2K}}\right] \tag{3.1.2.1}$$

This expression indicates that the heat transfer coefficient is a much stronger function of the wire diameter than of the temperature differential (Figure 8).

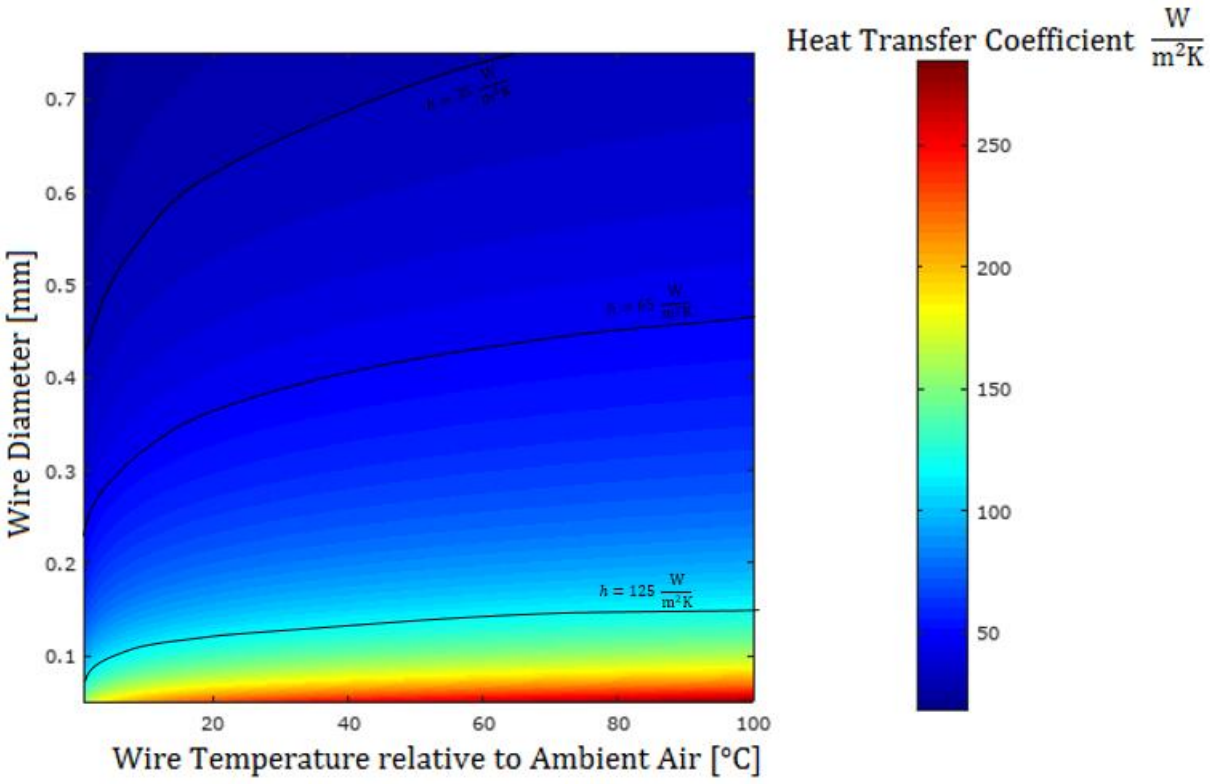

Figure 8. Convection Coefficient as a Function of Wire Diameter and Temperature Differential

3.1.2 Analytical Modelling of Thermal and Transformation Bandwidths

Utilizing the simplified form of the thermal model from Eq. 3.1.1.8, the heating and cooling bandwidth of the system can be found to be the inverse of the system eigenvalue such that:

$$\lambda_{cooling} = \frac{4h}{2\pi\rho d c_p} \tag{3.1.2.1}$$

Because the wire does not need to completely cool to its steady state temperature in order to actuate, the heating and cooling bandwidth does not accurately predict the system bandwidth. Neglecting the effects of latent heat of transformation and of radiation, the cooling response is that of exponential decay with a time constant ($\tau_{cooling}$) given by the inverse of the cooling bandwidth. The transformation times can also be visually demonstrated for this cooling response.

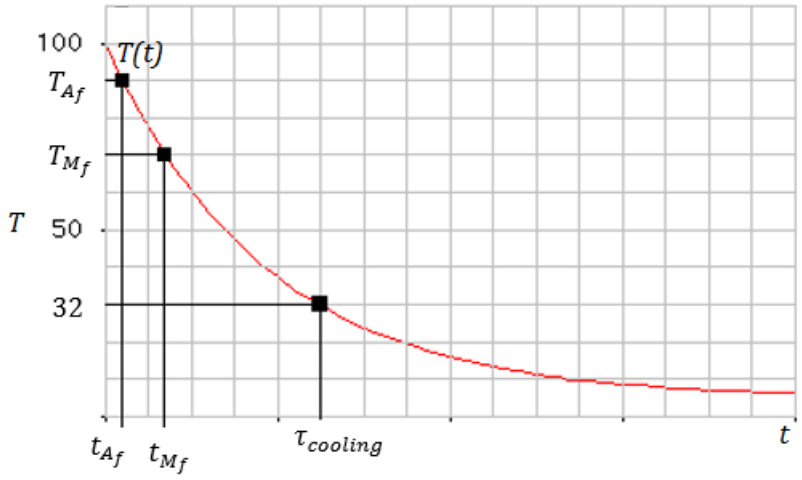

Figure 9. Newtonian Cooling with Transformation Times Labelled

To accommodate for this fact, a corrected thermal bandwidth is crafted that linearly scales the cooling bandwidth based on the range of temperatures the wire is exposed to and the range of temperatures it must traverse in order to actuate (denoted here as the mean transformation temperatures *A* and *M*), such as:

$$\lambda_{thermal} = \begin{cases} \left(\frac{2\left(\frac{M+A}{2} - T_\infty\right)}{A-M}\right)\frac{4h}{2\pi\rho d c_p}, & T_\infty < \frac{M+A}{2} \\ 0, & T_\infty \geq \frac{M+A}{2} \end{cases} \quad (3.1.2.2)$$

This type of scaling should give an upper estimate to the transformation bandwidth based on the fact that the upper temperature in the operating range and ambient temperature create bounds in which the transformation region lies centered. Obviously, T_∞ lies outside of the transformation region the system cannot transform and the bandwidth is zero as a result. Because the transformation bounds are dependent on the stress which varies in operation, it is not possible to approximate the bandwidth without approximating the terms for the transformation boundaries. Eq. 3.1.12 was evaluated for three distinct cases of ambient air conditions, with an average actuator stress of 150 MPa, and a transformation band of high temperature nickel titanium with a ten-degree transformation band gap. The results were plotted in Figure 10.

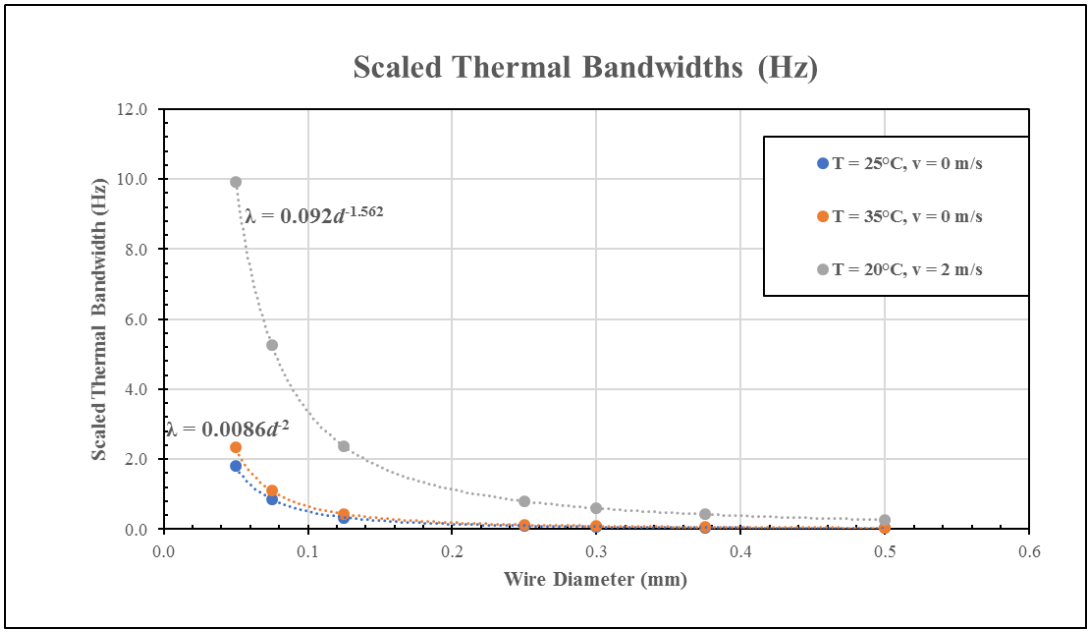

Figure 10. Thermal Transformation Bandwidths (Hz)

In stationary air, the bandwidth is not predicted to be a strong function of air temperature. By fitting the data with a power series, an approximation to the system bandwidth can be realized for natural convection in still air as a function of wire diameter (where the diameter is given in millimeters):

$$\lambda_{thermal} \approx \frac{0.0086 \ \frac{\text{mm}^2}{\text{s}}}{d^2} \ [\text{Hz}] \tag{3.1.2.3}$$

A different analytical approach to solving for the bandwidth of the system given in Eq. 3.1.1.4 is to directly solve for the cycle time to complete transformation and designate the system bandwidth equal to:

$$\lambda_{transform} \approx \frac{1}{t_{A\to M} + t_{M\to A}} \tag{3.1.2.4}$$

$t_{A\to M}$ denotes the minimum 100% Martensite transformation time and $t_{M\to A}$ denotes the minimum Austenite transformation time. For cases where the input power is selected such that the transformation times are roughly equal to one another, which is desirable when using control laws such as sliding mode control, only the cooling response needs to be numerically analyzed and:

$$\lambda_{transform} \approx \frac{1}{2t_{A\to M}} \tag{3.1.2.5}$$

Taking Eq. 3.1.2.5 and setting the applied current to zero and the initial temperature to the Austenite transformation bound and the final temperature to the Martensite transformation bound yields:

$$M = T_\infty + (A - T_\infty)e^{-\left(\frac{4h}{\rho d c_p}\right)t} \tag{3.1.2.6}$$

Solving for the transformation time then yields:

$$t_{A\to M} \approx -\left(\frac{\rho d c_p}{4h}\right)\ln\left(\frac{M-T_\infty}{A-T_\infty}\right) \tag{3.1.2.7}$$

The results of this analysis for nickel titanium alloys are presented in Table 5 for selected cases and includes a correction term for wire orientations of an angle θ. Analytically, the bandwidths differ because the empirically derived Nusselt numbers differ for a change in this angle.

Table 5. Transformation Bandwidths of Selected Cases

	Bandwidths (Hz)		
Wire Diameter (mm)	20 C, v = 2 m/s, 350 MPa	25 C, still air, 200 MPa	35 C, still air, 50 MPa
0.076	25.000	$1.667 + 1.275\sin(\theta)$	$0.581 + 0.623\sin(\theta)$
0.1	16.667	$0.980 + 0.687\sin(\theta)$	$0.336 + 0.182\sin(\theta)$
0.13	10.000	$0.575 + 0.425\sin(\theta)$	$0.198 + 0.146\sin(\theta)$
0.15	8.333	$0.435 + 0.301\sin(\theta)$	$0.149 + 0.111\sin(\theta)$
0.2	5.000	$0.244 + 0.176\sin(\theta)$	$0.100 + 0.046\sin(\theta)$
0.25	3.571	$0.156 + 0.114\sin(\theta)$	$0.0985 + 0.003\sin(\theta)$

In order to achieve a simple equation in the form of Eq 3.1.2.3, a power series fit was placed through the results of the second case due to the commonality of its conditions. The resulting expression for the transformation bandwidth is given by:

$$\lambda_{transform} \approx \frac{0.0099\ \frac{\text{mm}^2}{\text{s}} + 0.0068\sin(\theta)\frac{\text{mm}^2}{\text{s}}}{d^2}\ [\text{Hz}] \tag{3.1.2.8}$$

3.1.3 Analytical Modelling of Wire Efficiency

An approximation to the efficiency of an SMA wire by acknowledging that the work done by an SMA actuator that undergoes full transformation is given by:

$$W = L\varepsilon_L \Omega A_c \tag{3.1.3.1}$$

The efficiency can then be found assuming radiation and temperature variations through the material to be negligible:

$$\eta = \frac{\varepsilon_L \Omega d}{4h(T - T_\infty)t_{M\to A} + \rho d(c_p \Delta T + \Delta H)} \tag{3.1.3.2}$$

$t_{M\to A}$ denotes the time taken for the actuation to occur. This value can be approximated by assuming the input power does not have to overcome convection to heat up the actuator:

$$t_{M\to A} \approx \frac{m\left(c_p \Delta T + \Delta H\right)}{VI} = \frac{\rho \pi d^2 L\left(c_p (A - T_\infty) + \Delta H\right)}{4VI} \tag{3.1.3.2}$$

Substitution of this expression into Eq. 3.1.3.2 and substituting material properties of Flexinol High Temperature Nitinol [76] yields:

$$\eta \approx \frac{0.025309}{\left[\frac{0.026 \frac{\mathrm{m}}{\mathrm{V}^2}}{d}\left(\frac{L}{V}\right)^2 + 1\right]} \tag{3.1.3.3}$$

The notable aspect about this expression is that it estimates that the maximum efficiency that the actuator can achieve is 2.531%. This characteristically low efficiency is often cited as one of the biggest detriments to using a shape memory alloy actuator outside of the slow bandwidth.

3.1.4 Analytical Modelling of Thermocouple Measurement Distortion

An analytical approach to the modelling of a disturbance in the form of thermocouple connected directly to a wire actuator can be analytically modelled as an infinitely long fin connected to a heated base. This type of model would then yield an expression for the heat carried away from the wire actuator:

$$\dot{Q} = \sqrt{kA_c hP}\tanh(\chi L)(T_{SMA} - T_\infty) \tag{3.1.4.1}$$

where all properties are of the thermocouple, P represents the perimeter of the thermocouple, L represents the length of the thermocouple, and χ is a dimensionless parameter given by $\chi = \frac{hP}{kA_c}$. Given that a thermocouple consists of two separate wires of material, the average thermal conductivity between the materials should be used when performing the heat transfer analysis. For the most commonly used thermocouple, the K-type, these two wires are made of chromel ($k = 19\ \frac{\mathrm{W}}{\mathrm{mK}}$) and alumel ($k = 30\ \frac{\mathrm{W}}{\mathrm{mK}}$) which means the effective thermal conductivity can be modelled as two materials in parallel, such that:

$$k_{TC} = \frac{k_1 A_{c,1} + k_2 A_{c,2}}{A_{c,1} + A_{c,2}} \tag{3.1.4.2}$$

Because the cross-sectional areas of the wires can often be considered identical in a thermocouple, the equivalent thermal conductivity can simply be analyzed as the average thermal conductivity between the two wires. For the K-type thermocouple, the equivalent thermal conductance is then $k_{TC,K} \approx 25.5\ \frac{\mathrm{W}}{\mathrm{mK}}$. The average steady state temperature of a span of wire losing heat to the thermocouple and through convection is given by:

$$T_{SMA,TC} = \frac{\Delta V^2}{R}\left[\frac{1}{h_{SMA}\pi d_{SMA} L_{SMA} + \sqrt{k_{TC} A_{c_{TC}} h_{TC} P_{TC}}\tanh(\chi L_{TC})}\right] + T_\infty \tag{3.1.4.3}$$

The temperature disturbance caused at steady state is given by:

$$\Delta T_{dist} = \frac{\Delta V^2}{R}\left[\frac{1}{h_{SMA}\pi d_{SMA}L_{SMA} + \sqrt{k_{TC}A_{c_{TC}}h_{TC}P_{TC}}\tanh(\chi L_{TC})} - \frac{1}{h_{SMA}\pi d_{SMA}L_{SMA}}\right] \quad (3.1.4.4)$$

The thermocouple probe can be modelled as a horizontal cylinder in crossflow and the equation becomes:

$$\Delta T_{dist} = \frac{\Delta V^2}{R}\left[\frac{2}{2\pi h_{SMA}d_{SMA}L_{SMA} + \pi d_{TC}^{3/2}\sqrt{k_{TC}h_{TC}}\tanh\left(\frac{4h_{TC}L_{TC}}{k_{TC}d_{TC}}\right)} - \frac{1}{\pi h_{SMA}d_{SMA}L_{SMA}}\right] \quad (3.1.4.5)$$

Labelling the electric power generation of the small span of wire covered by the thermocouple as Q_{gen} and invoking Eq. 3.1.2.1 for approximations for the convection coefficient where the actuator is operating in still room temperature air (and approximating the convection coefficient dependence on ambient air temperature such that $h = 23d^{-4/5}$ where the diameter is expressed in meters), the expression then simplifies to:

$$\Delta T_{dist} = \frac{Q_{gen}}{\pi}\left[\frac{1}{23{d_{SMA}}^{1/5}L_{SMA} + 4.8d_{TC}^{11/10}\sqrt{k_{TC}}\tanh\left(\frac{4h_{TC}L_{TC}}{k_{TC}d_{TC}}\right)} - \frac{1}{23{d_{SMA}}^{1/5}L_{SMA}}\right] \quad (3.1.4.6)$$

For the measurement of fine SMA wires, the thermocouple probe diameter is often very small and the ratio $\frac{L_{TC}}{d_{TC}}$ is often a large number as a result. The hyperbolic tangent function acts as a sigmoid function in that $\lim_{x\to\infty}\tanh x = 1$. As a result, it is oftentimes a decent approximation to state that $\tanh(\frac{4h_{TC}L_{TC}}{k_{TC}d_{TC}}) \approx 1$ and:

$$\Delta T_{dist} = \frac{Q_{gen}}{\pi}\left[\frac{1}{(23\ \mathrm{m}^{\frac{5}{6}}){d_{SMA}}^{1/5}L_{SMA} + \left(4.8\frac{\mathrm{m}^{22/9}\mathrm{K}^{1/2}}{\mathrm{W}^{1/2}}\right)d_{TC}^{11/10}\sqrt{k_{TC}}} - \frac{1}{\left(23\ \mathrm{m}^{\frac{5}{6}}\right){d_{SMA}}^{1/5}L_{SMA}}\right] \quad (3.1.4.7)$$

Eq. 3.1.4.6 gives the average temperature drop for the entire span of wire. The localized temperature disturbance can be very roughly approximated by setting $L_{SMA} = 5d_{TC}$ and scaling the generated heat term to accurately reflect the heat generation of just the small span of wire. This

type of approximation was performed for an example computation for a ten-centimeter span of wire subjected to one Watt of power generation and measured with various thermocouple types (Table 6).

Table 6. Localized Temperature Drops of 10 cm SMA actuator due to Presence of Thermocouple

Approximate Steady State Localized Temperature Disturbance (deg C) K-Type Thermocouple, 10 cm long SMA actuator in room temperature air, 1 W applied power							
	SMA Diameter (m)						
Thermocouple Diameter (m)	0.000025	0.000038	0.00005	0.000125	0.0002	0.00025	0.0005
0.00001	-0.891	-0.389	-0.226	-0.038	-0.015	-0.010	-0.003
0.000025	-	-2.392	-1.396	-0.234	-0.095	-0.062	-0.018
0.00005	-	-	-	-0.918	-0.375	-0.247	-0.070
0.000075	-	-	-	-2.009	-0.829	-0.547	-0.157
0.0001	-	-	-	-3.439	-1.437	-0.953	-0.275
0.000125	-	-	-	-	-2.177	-1.451	-0.424
0.00015	-	-	-	-	-3.023	-2.027	-0.600
0.000175	-	-	-	-	-3.949	-2.665	-0.801
0.0002	-	-	-	-	-	-3.351	-1.023
0.000225	-	-	-	-	-	-4.070	-1.263
0.00025	-	-	-	-	-	-	-1.519
J-Type Thermocouple, 10 cm long SMA actuator in room temperature air, 1 W applied power							
	SMA Diameter (m)						
Thermocouple Diameter (m)	0.000025	0.000038	0.00005	0.000125	0.0002	0.00025	0.0005
0.00001	-1.256	-0.548	-0.319	-0.053	-0.022	-0.014	-0.004
0.000025	-	-3.352	-1.959	-0.329	-0.134	-0.088	-0.025
0.00005	-	-	-	-1.285	-0.527	-0.347	-0.099
0.000075	-	-	-	-2.781	-1.155	-0.764	-0.220
0.0001	-	-	-	-4.696	-1.985	-1.321	-0.385
0.000125	-	-	-	-	-2.973	-1.993	-0.590
0.00015	-	-	-	-	-4.078	-2.755	-0.830
0.000175	-	-	-	-	-5.257	-3.582	-1.099
0.0002	-	-	-	-	-	-4.449	-1.393
0.000225	-	-	-	-	-	-5.336	-1.707
0.00025	-	-	-	-	-	-	-2.034
T-Type Thermocouple, 10 cm long SMA actuator in room temperature air, 1 W applied power							
	SMA Diameter (m)						
Thermocouple Diameter (m)	0.000025	0.000038	0.00005	0.000125	0.0002	0.00025	0.0005
0.00001	-2.544	-1.113	-0.648	-0.108	-0.044	-0.029	-0.008
0.000025	-	-6.663	-3.917	-0.666	-0.271	-0.178	-0.051
0.00005	-	-	-	-2.539	-1.052	-0.696	-0.200
0.000075	-	-	-	-5.306	-2.255	-1.503	-0.440
0.0001	-	-	-	-8.584	-3.758	-2.533	-0.759
0.000125	-	-	-	-	-5.438	-3.711	-1.142
0.00015	-	-	-	-	-7.184	-4.966	-1.574
0.000175	-	-	-	-	-8.910	-6.239	-2.040
0.0002	-	-	-	-	-	-7.485	-2.526
0.000225	-	-	-	-	-	-8.675	-3.019
0.00025	-	-	-	-	-	-	-3.509

The chosen power supply of one Watt is convenient because it allows for these values to linearly scale with the power supplied to the SMA actuator for a ten-centimeter span of wire. The basic observations of the values listed are first that the selected thermocouple should have a low a

thermal conductivity as is possible to limit the amount of heat that is dissipated from the shape memory actuator. Secondly, the temperature profile becomes more distorted as the thermocouple probe diameter increases in size with respect to the actuator diameter. For example, in order to obtain less than one degree Celsius of temperature disturbance per Watt of power supplied for a K-type thermocouple on a ten-centimeter span of wire, the diameter of the shape memory alloy actuator must be approximately five times the diameter of the thermocouple probe. As the span of wire increases, the localized temperature disturbance will also decrease as a result of the steady state temperature going down across the entire wire.

The overall temperature disturbance to the measurement for a thermocouple placed onto a portion of an SMA actuator is quantified by comparison of the heat transfer lost to the thermocouple to the convective heat transfer that would take place if the thermocouple was not present (the fin effectiveness, denoted here as ϱ_{fin}):

$$\varrho_{fin} = \frac{\sqrt{kA_c hP}\tanh(\chi L)}{hA_b} \text{ [unitless]} \tag{3.1.4.8}$$

Simplifying this expression in terms of the geometrical properties of the thermocouple and the SMA actuator yields:

$$\varrho_{fin} = \frac{2\sqrt{k_{TC}h_{TC}}\tanh(\frac{4h_{TC}L_{TC}}{k_{TC}d_{TC}})}{h_{SMA}{d_{TC}}^{1/2}} \tag{3.1.4.9}$$

Again, the hyperbolic tangent term can be set to unity for an infinitely long fin:

$$\varrho_{fin} = \frac{2\sqrt{k_{TC}h_{TC}}}{h_{SMA}{d_{TC}}^{1/2}} \tag{3.1.4.10}$$

The convection coefficient can be estimated for the thermocouple wires using Eq. 3.1.2.1 if the working fluid surrounding the SMA actuator is air, otherwise it can be found by using the appropriate empirical relationship for the Nusselt number. For situations where Eq. 3.1.2.1 is a valid approximation, the temperature disturbance can be modelled as:

$$\varrho_{fin} \approx \left(0.417 \frac{\mathrm{m}^{11/5}\mathrm{K}^{9/16}}{\mathrm{W}^{1/2}}\right) \frac{\sqrt{k_{TC}}}{{d_{SMA}}^{4/5} {d_{TC}}^{9/10}} (T - T_{\infty})^{-1/16} \tag{3.1.4.11}$$

For the K-type thermocouple, this relationship becomes:

$$\varrho_{TC,K} \approx \frac{2.105\ \mathrm{m}^{17/10}\mathrm{K}^{1/16}}{{d_{SMA}}^{4/5} {d_{TC}}^{9/10}} (T - T_{\infty})^{-1/16} \tag{3.1.4.12}$$

For an average case where $T - T_{\infty} = 50℃$, such a relationship for a K-type thermocouple becomes:

$$\varrho_{TC,K}{}^{avg} \approx \frac{1.648\ \mathrm{m}^{17/10}}{{d_{SMA}}^{4/5} {d_{TC}}^{9/10}} \tag{3.1.4.13}$$

In general, the thermocouple effectiveness at removing heat can be expressed in this way as the following equation:

$$\varrho_{TC} \approx \frac{A}{{d_{SMA}}^{4/5} {d_{TC}}^{9/10}} \tag{3.1.4.14}$$

This constant can be derived for the commonly used thermocouple types for a variety of temperature ranges. The results are tabulated in Table 7.

Table 7. Constant *A* in $\mathbf{m^{1.7}}$ for Thermocouple Fin Effectiveness Model

	$T - T_{\infty} = 0℃$	$T - T_{\infty} = 10℃$	$T - T_{\infty} = 50℃$	$T - T_{\infty} = 100℃$
K-Type	0	1.824	1.649	1.579
J-Type	0	2.574	2.327	2.229
N-Type	0	1.670	1.510	1.446
T-Type	0	5.246	4.744	4.543

The analysis of the fin effectiveness reiterates that a thermocouple with low thermal conductivity constituent metals, such as the N-type or K-type thermocouple, will have a lower fin effectiveness and therefore not distort the temperature as much (with the heat loss due to convection being increased by 50% for these thermocouple types) when compared to thermocouples with higher thermal conductivities (such as the J-type or T-type, which can increase the local heat loss by well over 100% what it would have been from convection of the actuator alone).

3.2 Numerical Analysis with Finite Difference Method

Even with the lumped capacitance model presented in Equation 3.1.1, the response of a wire actuator cannot be obtained analytically. When radiation is also accounted for, the equations become even more nonlinear and a numerical approach becomes superior to an analytical approach. Using Eq. 2.5.22 as the basis of formulation for the lumped capacitance, or 0-D model, a numerical solution can be obtained through numerical integration of the following equation which represents an SMA wire actuator that is electrically crimped and tied off to one fixed end and the system plant (Figure 11).

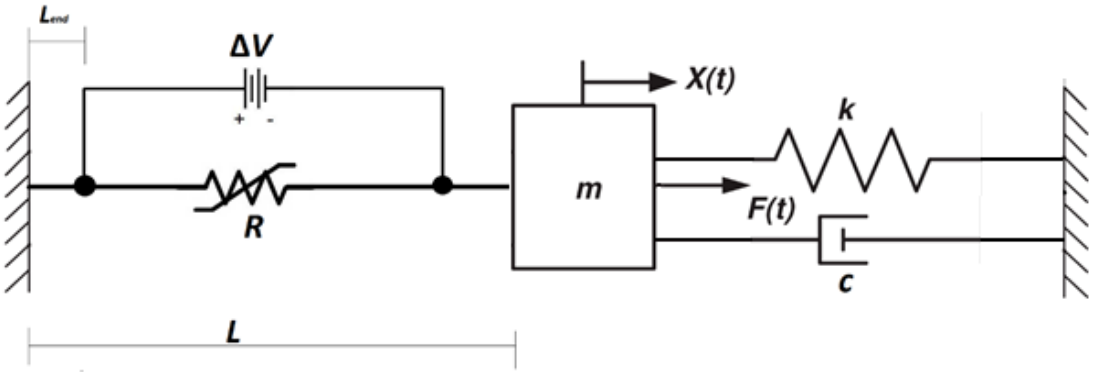

Figure 11. Simulation Test Case

The equation of motion for the mass is given by:

$$m\ddot{x} = kx + c\dot{x} + F(t) - K_{SMA}L(\varepsilon - \varepsilon_L\xi) - \theta E A_c(T - T_0) - F_{preload} \tag{3.2.1}$$

where k is the spring rate, c is the damping coefficient, x is the position of the mass, m is the mass, $F(t)$ is any time-varying applied force to the mass, ε is the total strain of the wire which is defined as zero when the wire is in the Austenite phase with no elastic deformation, $\varepsilon_L\xi$ is the wire deformation caused by the phase change, A_c is the cross-sectional area, θ is the thermal expansion

coefficient in terms of the stress imparted onto the actuator due to the temperature change in the actuator, T is the temperature of the actuator, T_0 is the initial actuator temperature, and $F_{preload}$ is the preload force. The proceeding sections will derive schemes that can numerically solve for the temperature response in the wire for use in these equations of motion.

3.2.1 Lumped Capacitance Modelling [0-D Model]

The simulation process would then solve for the time derivative of temperature at each time step using:

$$\frac{dT}{dt} = \left(\frac{1}{mc_p}\right)\left\{\frac{\Delta V^2}{R} - \left[hA_s + 2k\left(\frac{A_c}{L_{end}}\right)\right](T - T_{air}) - \epsilon\sigma_b A_s\left(T^4 - {T_{air}}^4\right) - m\Delta H\dot{\xi} + \sigma A_c \varepsilon_L \dot{\xi}\right\} \quad (3.2.1.1)$$

The temperature can then be numerically integrated using a variety of integration schemes such as the Trapezoidal Method or Simpson's Rule:

$$T(t) = T_{t-\Delta t} + \int_{t-\Delta t}^{t} \frac{dT}{dt}dt \approx T_{t-\Delta t} + \frac{1}{2}\left(\frac{dT}{dt}_{t-\Delta t} + \frac{dT}{dt}_{t}\right) \quad (3.2.1.2)$$

The kinetics model described by Eq. 2.4.5a and Equation 2.4.5b could then be used to define the new phase fraction of the lumped mass, which in turn can yield the new macroscopic properties for the next time step, as well as a value for $\dot{\xi}$. The temperature equation can then be recursively solved for the same time step with an updated phase fraction derivative for more accurate results. The strain can then be computed with Eq. 2.2.5, which in turn cause Poisson expansion and changes the values of both the cross-sectional area and the surface area of the wire.

3.2.2 Axially Discretized Modelling [1-D Model]

The shortcomings of the lumped capacitance model is that it does not provide a good way to model disturbances along the wire like those that would be present from any sort of probe as part of a measurement device and it does not take into account boundary effects at the edges of the wire. In order to take into account these considerations, a 1-D model discretizes the SMA wire actuator along its length into a series of control volumes. The position index of each node will be denoted with *i* corresponding to a grid spacing of $\Delta x = \frac{L}{n-1}$ where *n* is the total number of nodes. This discretization is illustrated in Figure 12, and n_b is used to denote the boundary at which electricity is used to heat the wire.

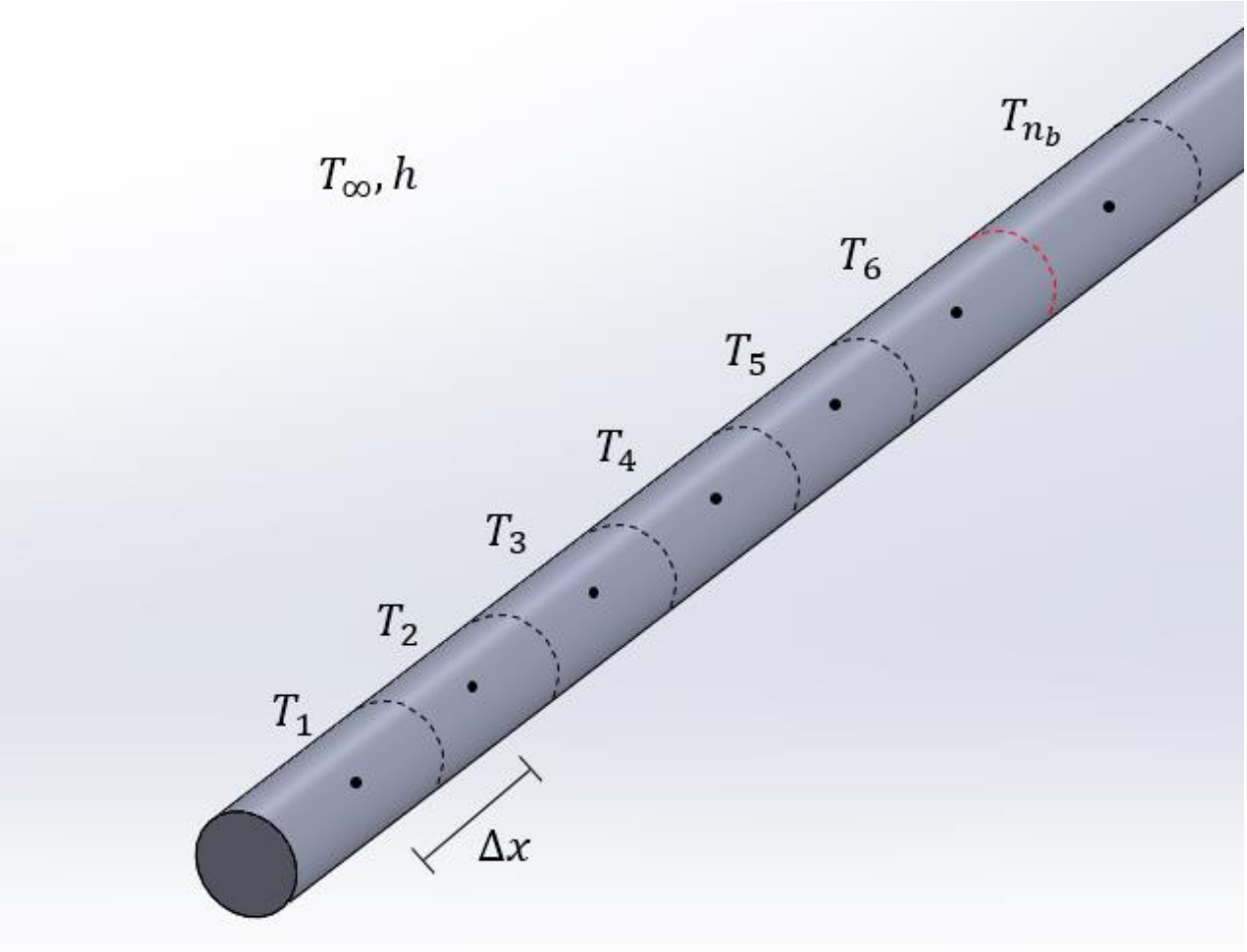

Figure 12. Axial Discretization of Wire Actuator

The time step index is denoted with ℓ which corresponds to a time step of Δt seconds after the preceding time step. The following equations are derived from the conservation of energy about a control volume centered around a node and are valid from nodes $i = 2$ to $i = n - 1$:

$$\dot{q}_{cond,\ i-1/2} = \dot{q}_{cond,\ i+1/2} + \dot{q}_{conv,\ i} + \dot{q}_{rad,\ i} + \dot{q}_{electric,\ i} + \dot{q}_{latent\ heat,\ i} + \dot{q}_{stored,\ i} \qquad (3.2.2.1)$$

Upon evaluation of each expression, a number of them are found to contain derivatives of temperature curve with respect to *x*. These derivatives are evaluated for a general case of time between the current time step ℓ and the time step $\ell + 1$ by utilizing a weighting factor γ, where $0 \leq \gamma \leq 1$, and evaluating the nodal temperatures at a time step of $\ell + \gamma$. Therefore, the conservation of energy equation given in Eq. 3.2.2.1 becomes:

$$\begin{aligned} k_{i-\frac{1}{2}}\pi r^2 \frac{T_{i-1}^{\ell+\gamma} - T_i^{\ell+\gamma}}{\Delta x} + \left(I^2R + \sigma A_c L \varepsilon_L \frac{\xi_i^{\ell+1} - \xi_i^{\ell}}{\Delta t}\right)\left(\frac{\Delta x}{L}\right) \\ = k_{i+\frac{1}{2}}\pi r^2 \frac{T_i^{\ell+\gamma} - T_{i+1}^{\ell+\gamma}}{\Delta x} + 2h_i \pi r \Delta x \left(T_i^{\ell+\gamma} - T_{air}\right) + 2\epsilon\sigma_b \pi r \Delta x \left(\left[T_i^{\ell+\gamma}\right]^4 - {T_{air}}^4\right) \\ + \rho\pi r^2 \Delta x \Delta H \frac{\xi_i^{\ell+1} - \xi_i^{\ell}}{\Delta t} + \rho c_p \pi r^2 \Delta x \frac{T_i^{\ell+1} - T_i^{\ell}}{\Delta t} \end{aligned} \qquad (3.2.2.2)$$

While this is an adequate discretized model, a more accurate model can be developed by viewing the temperature profile in the wire as a series of lines that connect each nodal temperature and integrating the heat equation over the entire control volume. Formally, this is termed the weak form of the solution and is expressed as:

$$\int_{x_i-\Delta x/2}^{x_i+\Delta x/2} \left\{ \rho c_p \frac{\partial T}{\partial t} - \frac{\partial}{\partial x}\left[k\frac{\partial T}{\partial x}\right] - \frac{4h}{d}(T - T_\infty) - \frac{4\epsilon\sigma_b}{d}\left(T^4 - {T_\infty}^4\right) - \dot{q}'''_{gen} \right\} dx = 0 \qquad (3.2.1.3)$$

Performing this integration and discretizing the solution, the following system is obtained:

$$\begin{aligned} k_{i-\frac{1}{2}}\frac{T_{i-1}^{\ell+\gamma}-T_i^{\ell+\gamma}}{\Delta x}+I^2R\left(\frac{\Delta x}{\pi r^2 L}\right)+\sigma\varepsilon_L\Delta x\frac{\xi_i^{\ell+1}-\xi_i^{\ell}}{\Delta t} \\ =k_{i+\frac{1}{2}}\frac{T_i^{\ell+\gamma}-T_{i+1}^{\ell+\gamma}}{\Delta x}+\frac{2h_i\Delta x}{r}\left(3T_i^{\ell+1}+\frac{T_{i+1}^{\ell+\gamma}+T_{i-1}^{\ell+\gamma}}{2}-4T_{air}\right) \\ +\frac{2\epsilon\sigma_b\Delta x}{r}\left(\left[T_i^{\ell+\gamma}\right]^4-{T_{air}}^4\right)+\rho\Delta x\Delta H\frac{\xi_i^{\ell+1}-\xi_i^{\ell}}{\Delta t} \\ +\rho c_p\frac{\Delta x}{\Delta t}\left[\frac{1}{8}\left(\left(T_{i+1}^{\ell+1}+T_{i-1}^{\ell+1}\right)-\left(T_{i+1}^{\ell}+T_{i-1}^{\ell}\right)\right)+\frac{3}{4}\left(T_i^{\ell+1}-T_i^{\ell}\right)\right] \end{aligned} \tag{3.2.2.4}$$

This can be algebraically manipulated to form an energy balance equation for each node:

$$\begin{aligned} f_i=0=\left(1-\frac{h_i\Delta x^2}{k_{i-\frac{1}{2}}r}\right)T_{i-1}^{\ell+\gamma}-\left(1+\frac{k_{i+\frac{1}{2}}}{k_{i-\frac{1}{2}}}+\frac{6h_i\Delta x^2}{k_{i-\frac{1}{2}}r}\right)T_i^{\ell+\gamma}-\frac{2\epsilon\sigma_b\Delta x^2}{k_{i-\frac{1}{2}}r}\left(T_i^{\ell+\gamma}\right)^4 \\ +\left(\frac{k_{i+\frac{1}{2}}}{k_{i-\frac{1}{2}}}-\frac{h_i\Delta x^2}{k_{i-\frac{1}{2}}r}\right)T_{i+1}^{\ell+\gamma}+\frac{8h_i\Delta x^2}{k_{i-\frac{1}{2}}r}T_{air}+\frac{2\epsilon\sigma_b\Delta x^2}{k_{i-\frac{1}{2}}r}(T_{air})^4+\left(\frac{\Delta x^2}{Lk_{i-\frac{1}{2}}\pi r^2}\right)I^2R \\ +\left(\frac{\Delta x^2}{k_{i-\frac{1}{2}}}\right)\left[\sigma\varepsilon_L\frac{\xi_i^{\ell+1}-\xi_i^{\ell}}{\Delta t}\right]-\frac{\rho\Delta x^2\Delta H}{k_{i-\frac{1}{2}}}\left(\frac{\xi_i^{\ell+1}-\xi_i^{\ell}}{\Delta t}\right) \\ -\frac{\rho c_p\Delta x^2}{k_{i-\frac{1}{2}}\Delta t}\left[\frac{1}{8}\left(\left(T_{i+1}^{\ell+1}+T_{i-1}^{\ell+1}\right)-\left(T_{i+1}^{\ell}+T_{i-1}^{\ell}\right)\right)+\frac{3}{4}\left(T_i^{\ell+1}-T_i^{\ell}\right)\right] \end{aligned} \tag{3.2.2.5}$$

Because the thermal conductivity is likely to be different for control volumes in contact, an equivalent thermal conductivity is used that reflects the abrupt change for control volume interface between nodes i and $i+1$:

$$k_{i+\frac{1}{2}}=\frac{2k_{i+1}k_i}{k_{i+1}+k_i} \tag{3.2.2.6}$$

In order to simplify the system the following constants can be defined:

$$C_1 = \frac{2h_i\Delta x^2}{k_{i-\frac{1}{2}}r} = \mathrm{Bi}\left(\frac{\Delta x}{r}\right)^2 \text{ [dimensionless]} \tag{3.2.2.7}$$

$$C_2 = \frac{2\epsilon\sigma_b\Delta x^2}{k_{i-\frac{1}{2}}r} \ [K^{-3}] \tag{3.2.2.8}$$

$$C_3 = \frac{\rho c_p\Delta x^2}{k_{i-\frac{1}{2}}\Delta t} = \frac{1}{\mathrm{Fo}} \text{ [dimensionless]} \tag{3.2.2.9}$$

$$k_r = \frac{k_{i+\frac{1}{2}}}{k_{i-\frac{1}{2}}} = \frac{k_{i+1}}{k_{i-1}}\left(\frac{k_i + k_{i-1}}{k_i + k_{i+1}}\right) \text{ [dimensionless]} \tag{3.2.2.10}$$

$$C_H = \frac{\rho\Delta x^2\Delta H}{k_{i-\frac{1}{2}}} \ [\mathrm{K}\cdot\mathrm{s}] \tag{3.2.2.11}$$

$$C_e = \frac{\Delta x^2}{Lk_{i-\frac{1}{2}}\pi r^2} \ [\frac{\mathrm{K}}{\mathrm{W}}] \tag{3.2.2.12}$$

$$C_W = \frac{\Delta x^2}{k_{i-\frac{1}{2}}} \ [\frac{\mathrm{K\,m^2}}{\mathrm{W}}] \tag{3.2.2.13}$$

The system then becomes:

$$\begin{aligned} f_i = 0 = {} & \left(1 - \frac{C_1}{2}\right)T_{i-1}^{\ell+\gamma} - (1 + k_r + 3C_1)T_i^{\ell+\gamma} - C_2\left(T_i^{\ell+\gamma}\right)^4 + \left(k_r - \frac{C_1}{2}\right)T_{i+1}^{\ell+\gamma} + 4C_1T_{air} \\ & + C_2(T_{air})^4 + C_eI^2R + C_W\left[\sigma\varepsilon_L\frac{\xi_i^{\ell+1} - \xi_i^{\ell}}{\Delta t}\right] - C_H\left(\frac{\xi_i^{\ell+1} - \xi_i^{\ell}}{\Delta t}\right) \\ & - C_3\left[\frac{1}{8}\left((T_{i+1}^{\ell+1} + T_{i-1}^{\ell+1}) - (T_{i+1}^{\ell} + T_{i-1}^{\ell})\right) + \frac{3}{4}(T_i^{\ell+1} - T_i^{\ell})\right] \end{aligned} \tag{3.2.2.14}$$

For this analysis, it is preferred to let $\gamma = 1$, which is the Backward Time Centered Space solution method for the transient response of the thermal system, because it can be shown that this methodology is unconditionally stable for all grid spacing and time step increments. For contrast, letting $\gamma = 0$ would yield an explicit equation for the temperature at each node at the next time

step, but it can be shown that this method is unstable for $\mathrm{Fo} > \frac{1}{2}$. The conservation of energy equations then become:

$$f_i = 0 = \left(1 - \frac{C_1}{2}\right) T_{i-1}^{\ell+1} - (1 + k_r + 3C_1) T_i^{\ell+1} - C_2 \left(T_i^{\ell+1}\right)^4 + \left(k_r - \frac{C_1}{2}\right) T_{i+1}^{\ell+1} + 4C_1 T_{air} + C_2 (T_{air})^4 + C_e I^2 R + C_W \left[\sigma \varepsilon_L \frac{\xi_i^{\ell+1} - \xi_i^{\ell}}{\Delta t}\right] - C_H \left(\frac{\xi_i^{\ell+1} - \xi_i^{\ell}}{\Delta t}\right) - C_3 \left[\frac{1}{8}\left(\left(T_{i+1}^{\ell+1} + T_{i-1}^{\ell+1}\right) - \left(T_{i+1}^{\ell} + T_{i-1}^{\ell}\right)\right) + \frac{3}{4}\left(T_i^{\ell+1} - T_i^{\ell}\right)\right] \tag{3.2.2.15}$$

Due to the nature of the third constant, it is more convenient to utilize the Fourier number and rewrite the constants such that:

$$C_1 = \frac{2h_i \Delta x^2}{k_{i-\frac{1}{2}} r} \mathrm{Fo} = \mathrm{BiFo} \left(\frac{\Delta x}{r}\right)^2 \tag{3.2.2.16}$$

$$C_2 = \frac{2\epsilon \sigma_b \Delta x^2}{k_{i-\frac{1}{2}} r} \mathrm{Fo} \tag{3.2.2.17}$$

$$C_H = \frac{\rho \Delta x^2 \Delta H}{k_{i-\frac{1}{2}}} \mathrm{Fo} = \frac{\Delta H \Delta t}{c_p} \tag{3.2.2.18}$$

$$C_e = \frac{\Delta x^2}{L k_{i-\frac{1}{2}} \pi r^2} \mathrm{Fo} = \frac{\Delta t}{\rho c_p L \pi r^2} \tag{3.2.2.19}$$

$$C_W = \frac{\Delta x^2}{L k_{i-\frac{1}{2}}} \mathrm{Fo} = \frac{\Delta t}{\rho c_p L} \tag{3.2.2.20}$$

Now, the system of conservation of energy equations for the inner nodes becomes:

$$f_i = 0 = \left(\frac{1}{8} - \mathrm{Fo} + \frac{C_1}{2}\right) T_{i-1}^{\ell+1} + \left(\frac{3}{4} + \mathrm{Fo} k_r + \mathrm{Fo} + 3C_1\right) T_i^{\ell+1} - C_2 \left(T_i^{\ell+1}\right)^4 + \left(\frac{1}{8} - \mathrm{Fo} k_r + \frac{C_1}{2}\right) T_{i+1}^{\ell+1} - 4C_1 T_{air} - C_2 (T_{air})^4 - C_e I^2 R - C_W \left[\sigma \varepsilon_L \frac{\xi_i^{\ell+1} - \xi_i^{\ell}}{\Delta t}\right] + C_H \left(\frac{\xi_i^{\ell+1} - \xi_i^{\ell}}{\Delta t}\right) - \frac{1}{8}\left(\left(T_{i+1}^{\ell} + T_{i-1}^{\ell}\right)\right) - \frac{3}{4} T_i^{\ell} \tag{3.2.2.21}$$

It is worth noting that although Eq. 3.2.2.19 is derived using a first order backwards difference method computation of both the actuator stress and nodal phase fraction, higher order numerical differentiation methods are utilized in simulations for numerical stability and smoothness of the solution. These numerical derivatives, all backwards in time of varying orders of accuracy are given for some time varying property $\psi(t)$ [77]:

First Order: $$\frac{\partial \psi}{\partial \mathrm{t}} \approx \frac{\psi^{\ell+1} - \psi^{\ell}}{\Delta t} \tag{3.2.2.22a}$$

Second Order: $$\frac{\partial \psi}{\partial \mathrm{t}} \approx \frac{3\psi^{\ell+1} - 4\psi^{\ell} + \psi^{\ell+1}}{2\Delta t} \tag{3.2.2.22b}$$

Third Order: $$\frac{\partial \psi}{\partial \mathrm{t}} \approx \frac{22\psi^{\ell+1} - 36\psi^{\ell} + 18\psi^{\ell-1} - 4\psi^{\ell-2}}{12\Delta t} \tag{3.2.2.22c}$$

Fourth Order: $$\frac{\partial \psi}{\partial \mathrm{t}} \approx \frac{25\psi^{\ell+1} - 48\psi^{\ell} + 36\psi^{\ell-1} - 16\psi^{\ell-2} + 3\psi^{\ell-3}}{12\Delta t} \tag{3.2.2.22d}$$

Fifth Order: $$\frac{\partial \psi}{\partial \mathrm{t}} \approx \frac{137\psi^{\ell+1} - 300\psi^{\ell} + 300\psi^{\ell-1} - 200\psi^{\ell-2} + 75\psi^{\ell-3} - 12\psi^{\ell-4}}{60\Delta t} \tag{3.2.2.22e}$$

Sixth Order: $$\frac{\partial \psi}{\partial \mathrm{t}} \approx \frac{147\psi^{\ell+1} - 360\psi^{\ell} + 450\psi^{\ell-1} - 400\psi^{\ell-2} + 225\psi^{\ell-4} - 72\psi^{\ell-4} + 10\psi^{\ell-5}}{60\Delta t} \tag{3.2.2.22f}$$

For smoother solutions, it is suggested that a linear relationship be assumed for the phase fraction between each node such that the average phase fraction inside of each control volume is given by:

$$\left[\xi_i^{eff}\right]^{\ell} = \frac{2\xi_i^{\ell} + \xi_{i-1}^{\ell} + \xi_{i+1}^{\ell}}{4} \tag{3.2.2.23}$$

This expression can then be differentiated to compute the phase fraction time derivative in recursive fashion in order to compute more accurate expressions for the nodal temperatures. However, it has been found through a number of simulations that this technique results in artificial cooling of the first unheated node outside of the electrically heated domain and artificial heating of the first heated node inside of the electrically heated domain. These errors at the interface are a result of a misrepresentation of the phase composition of the interface and a misapplication of the

latent heat of transformation as a result. Because of this, it is recommended that $\xi_{n_b}^{eff} = \xi_{n_b}^{\ell}$ and $\xi_{n_b-1}^{eff} = \xi_{n_b-1}^{\ell}$.

The two equations that define the boundary conditions for $i = 1$ and $i = n$ will be established based on the fact that the two boundary conditions must be explicitly given. The governing assumption for the boundary conditions will be that the boundaries are far enough from the electric crimps so as to be considered constant at the ambient temperature of the air. Therefore:

$$f_1 = 0 = T_1^{\ell+1} - T_{air} \tag{3.2.2.24}$$

$$f_n = 0 = T_n^{\ell+1} - T_{air} \tag{3.2.2.25}$$

The partial derivatives of f_i with respect to nodal temperatures for the nodes ranging from $i = 1$ and $i = n - 1$ are given by:

$$\frac{\partial f_i}{\partial T_{i-1}^{\ell+1}} = \frac{1}{8} - \mathrm{Fo} + \frac{C_1}{2} \tag{3.2.2.26}$$

$$\frac{\partial f_i}{\partial T_i^{\ell+1}} = \frac{3}{4} + \mathrm{Fo}k_r + k_r + 3C_1 + 4C_2(T_i^{\ell+1})^3 \tag{3.2.2.27}$$

$$\frac{\partial f_i}{\partial T_{i+1}^{\ell+1}} = \frac{1}{8} - \mathrm{Fo}k_r + \frac{C_1}{2} \tag{3.2.2.28}$$

The partial derivatives of f_i with respect to nodal temperatures for the boundary nodes at $i = 1$ and $i = n - 1$ are given by:

$$\frac{\partial f_i}{\partial T_{i-1}^{\ell+1}} = 0 \tag{3.2.2.29}$$

$$\frac{\partial f_i}{\partial T_i^{\ell+1}} = 1 \tag{3.2.2.30}$$

$$\frac{\partial f_i}{\partial T_{i+1}^{\ell+1}} = 0 \tag{3.2.2.31}$$

The Jacobian, $\bar{\bar{J}}$, of the system will take the form of a tridiagonal matrix and is invertible. Therefore, if an initial guess is made for the change in temperature of each node for the next time step which will be a vector of temperatures termed $\overline{\Delta T^{\ell+1}}$, Newton's method allows for the values of $\overline{\Delta T}$ to be improved through an iterative process such that:

$$\overline{f^{\ell+1,\ \text{new}}} = \overline{f^{\ell+1,\ \text{old}}} + \bar{\bar{J}}\,\overline{\Delta T^{\ell+1}} \tag{3.2.2.32}$$

$$\overline{\Delta T^{\ell+1}} = \bar{\bar{J}}^{-1}\left(\overline{f^{\ell+1,\ \text{new}}} - \overline{f^{\ell+1,\ \text{old}}}\right) \tag{3.2.2.33}$$

Because the conservation of energy equations should sum to zero, $\overline{f^{\ell+1,\ \text{new}}}$ is set to zero and:

$$\overline{\Delta T^{\ell+1}} = -\bar{\bar{J}}^{-1}\overline{f^{\ell+1,\ \text{old}}} \tag{3.2.2.34}$$

This process may be iterated through as many times is required until the temperature at each node at the proceeding time step converges to a solution. The first iteration will use $\overline{T^{\ell+1,\ \text{old}}} = \overline{T^{\ell}}$ and compute the Jacobian that reflects this condition. The Jacobian is also updated upon updating the nodal temperatures with each iteration because the Jacobian is dependent on the nodal temperatures at the time step $\ell + 1$ due to the radiation term. In order to check for the convergence of the simulation at each time step, the root mean squared value of the $\overline{\Delta T^{\ell+1}}$ vector is used to evaluate the error for each iteration. The iterations at a given time step will cease when this value falls below a maximum allowable error band.

Similarly to the lumped capacitance model, once the new temperatures are found, the phase fraction at the next time step can be computed. The solution the temperature and phase fraction are intertwined by definition due to latent heat, so as the phase fraction is solved for it must be used to recursively solve for the temperature. As the wire length changes, uniform spacing of the nodes is important to maintain the form of the system of equations, so grid spacing changes after every time step to reflect to resizing of the wire.

In order to reflect the fact that there are lengths of wire outside of where the electric crimps connect, a group of nodes are placed on both sides of the geometry outside of the inner nodes and their lengths of wire do not contribute to the computed resistance of the wire, nor does any current pass through them. Therefore, Equation 95 still applies to these nodes, but the term representing the electric power will be removed. In this way, the boundary effects can be numerically solved for.

The resistance of the electrically heated portion of wire is computed by summing the resistance of each control volume as though they were resistors in series such that:

$$R = \sum_{i=1}^{n} [\rho_e]_i \frac{\Delta x}{\pi r^2} \tag{3.2.2.35}$$

Once the nodal temperatures are solved for, the conductive heat transfer out of each face of the actuator, the heat transfer off of the wire, and the absorbed heat can be solved for:

$$\dot{q}_{cond,left} = -kA_c \left.\frac{dT}{dx}\right|_{x=0} \tag{3.2.2.36}$$

$$\dot{q}_{cond,right} = -kA_c \left.\frac{dT}{dx}\right|_{x=L} \tag{3.2.2.37}$$

$$\dot{q}_{off} = \int_0^L hA_s\left(T_i - T_{fluid}\right)dx + \int_0^L \epsilon\sigma_b A_s\left({T_i}^4 - {T_{fluid}}^4\right)dx \tag{3.2.2.38}$$

$$\dot{q}_{stored} = \int_0^L \rho A_c \Delta x c_p \frac{dT_i}{dt}dx + \int_0^L \rho A_c \Delta x \frac{d\xi_i}{dt}dx \tag{3.2.2.39}$$

Conservation of energy will dictate the following relationship between the quantities while transient effects are still noticeable (and the rate of energy storage in the actuator is not negligible):

$$\dot{q}_{cond,left} - \dot{q}_{cond,right} - \dot{q}_{off} = \dot{q}_{stored} + \dot{q}_{plasticity} + I^2R \tag{3.2.2.40}$$

If steady state is reached and the time derivative of temperature at each node tends towards zero, the rate of energy storage in the actuator becomes negligible and the steady state relation between these quantities can be obtained:

$$\dot{q}_{cond,left} - \dot{q}_{cond,right} = \dot{q}_{off} + I^2R \tag{3.2.2.41}$$

Note that the effects of plasticity have been considered negligible due to their small contribution to the energy balance. These procedures will need to run until steady state is reached or until the controller stabilizes the system. To test for convergence of the solutions to steady state, a dimensionless heat transfer ratio is defined:

$$q^* = \frac{\dot{q}_{stored}}{\dot{q}_{cond,left}} \tag{3.2.2.42}$$

Steady state can be said to have been reached as this quantity tends towards zero. For simulations that analyze a pure heating or cooling response, as time increases towards infinity the system should always tend towards steady state. This cannot be the only check for steady state, because as the number of nodes is reduced errors in the $\dot{q}_{stored}$ term emerge due to the lower resolution and numerical errors with the integration. In lieu of utilizing this parameter to check for steady state, two more reliable parameters can be developed instead:

$$(q^*)^{\ell+1} - (q^*)^{\ell} \approx 0 \text{ as } t \to t_{steady\ state} \tag{3.2.2.43}$$

$$\left[\frac{dT_i}{dt}\right]_{avg} = \frac{\sum_{i=1}^{i=n}\left(\frac{dT_i}{dt}\right)}{n} \to 0 \text{ as } t \to t_{steady\ state} \tag{3.2.2.44}$$

3.2.3 Axially and Radially Discretized Modelling [2-D Model]

In order to capture the distribution of temperatures radially as well as lengthwise in an SMA actuator, the system must be discretized radially as well as lengthwise. Due to symmetry, these radial control volumes can be viewed as thin disks around the actuator centerline. The solution process is very similar to the 1-D case, except now the lengthwise temperature profiles are found for each line of nodes radially and then the radial effects are accounted for by moving line by line across each column of nodes lengthwise. The nodal position indices lengthwise and radially are denoted (i, j) and correspond with grid spacing of $\Delta x = \frac{L}{n_L - 1}$ and $\Delta r = \frac{r}{n_r - 1}$, respectively, where n_L denotes the number of nodes lengthwise and n_r denotes the number of nodes radially. The position $j = 1$ corresponds with the centerline of the actuator. The time index is again denoted ℓ which corresponds to a time step of Δt.

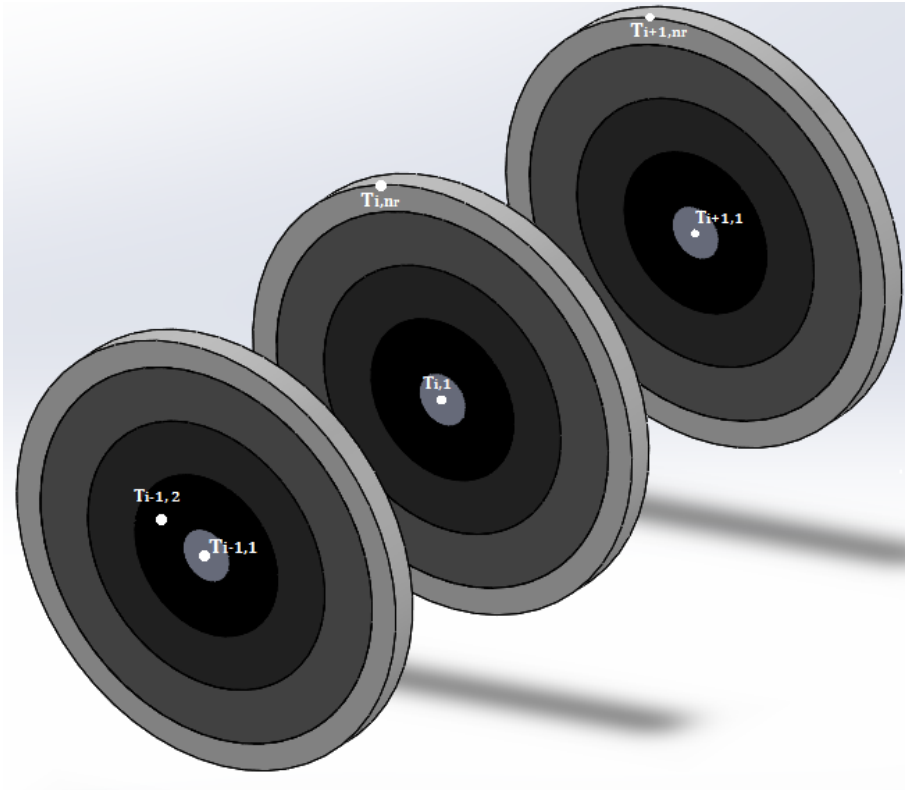

Figure 13. 2-D Discretization of Wire Actuator

The first portion of the solution process is to compute the effects of lengthwise thermal conduction and electric energy generation as well as the latent heat of transformation for all rows of nodes, as well as convection and radiation for the surface nodes, by solving conservation of energy relations for each line of nodes along the length of the wire. By integrating the heat equation over the control volumes for the inner nodes described by $i \in [2, n_L - 1]$ and $j \in [1, n_L - 1]$, the conservation of energy equations are given by:

$$\begin{aligned} & k_{i-\frac{1}{2},\ j}\pi\left((r_j + \frac{\Delta r}{2})^2 - (r_j - \frac{\Delta r}{2})^2\right)\frac{T^{\ell+\gamma}_{i-1,\ j} - T^{\ell+\gamma}_{i,\ j}}{\Delta x} \\ & \qquad = k_{i+\frac{1}{2},\ j}\pi\left((r_j + \frac{\Delta r}{2})^2 - (r_j - \frac{\Delta r}{2})^2\right)\frac{T^{\ell+\gamma}_{i,\ j} - T^{\ell+\gamma}_{i+1,\ j}}{\Delta x} \\ & \qquad - \left[I^2R + \sigma A_c L \varepsilon_L \frac{\xi_i^{\ell+1} - \xi_i^{\ell}}{\Delta t}\right]\left(\frac{\Delta x}{L}\right)\left(\frac{\left((r_j + \frac{\Delta r}{2})^2 - (r_j - \frac{\Delta r}{2})^2\right)}{r^2}\right) \\ & \qquad + \rho\pi\left((r_j + \frac{\Delta r}{2})^2 - (r_j - \frac{\Delta r}{2})^2\right)\Delta x \Delta H \frac{\xi^{\ell+1}_{i,\ j} - \xi^{\ell}_{i,\ j}}{\Delta t} \\ & \qquad + \rho c_p \pi\left((r_j + \frac{\Delta r}{2})^2 - (r_j - \frac{\Delta r}{2})^2\right)\frac{\Delta x}{\Delta t}\left[\frac{1}{8}\left(\left(T^{\ell+1}_{i,j} + T^{\ell+1}_{i,j}\right) - \left(T^{\ell}_{i,j} + T^{\ell}_{i,j}\right)\right)\right. \\ & \qquad \left. + \frac{3}{4}\left(T^{\ell+1}_{i,j} - T^{\ell}_{i,j}\right)\right] \end{aligned} \tag{3.2.3.1}$$

r_j denotes the position of the node that composes each discretized disk such that $r_j = 0, \Delta r, 2\Delta r, \ldots, r$. Note that the effects of radiation and convection are neglected because these nodes only transfer heat between them via conduction. This can be algebraically manipulated to form an energy balance equation for each node:

$$f_{i,j} = 0 = T_{i-1,j}^{\ell+\gamma} - \left(1 + \frac{k_{i+1,j}}{k_{i-1,j}}\left(\frac{k_{i,j} + k_{i-1,j}}{k_{i,j} + k_{i+1,j}}\right)\right) T_{i,j}^{\ell+\gamma} + \left(\frac{k_{i+1,j}}{k_{i-1,j}}\left(\frac{k_{i,j} + k_{i-1,j}}{k_{i,j} + k_{i+1,j}}\right)\right) T_{i+1,j}^{\ell+\gamma}$$
$$+ \left(\frac{\Delta x^2}{L k_{i-\frac{1}{2},j} \pi r^2}\right)\left[I^2 R + \sigma A_c L \varepsilon_L \frac{\xi_i^{\ell+1} - \xi_i^{\ell}}{\Delta t}\right] - \frac{\rho \Delta x^2 \Delta H}{k_{i-\frac{1}{2},j}}\left(\frac{\xi_i^{\ell+1} - \xi_i^{\ell}}{\Delta t}\right) \quad (3.2.3.2)$$
$$- \frac{\rho c_p \Delta x^2}{k_{i-\frac{1}{2},j} \Delta t}\left[\frac{1}{8}\left(\left(T_{i,j}^{\ell+1} + T_{i,j}^{\ell+1}\right) - \left(T_{i,j}^{\ell} + T_{i,j}^{\ell}\right)\right) + \frac{3}{4}\left(T_{i,j}^{\ell+1} - T_{i,j}^{\ell}\right)\right]$$

This expression is simplified through the use of the discretized lengthwise Fourier number:

$$\mathrm{Fo}_{\Delta \mathrm{x}} = \frac{k_{i-\frac{1}{2},j} \Delta t}{\rho c_p \Delta x^2} \quad (3.2.3.3)$$

$$k_r = \frac{k_{i+\frac{1}{2},j}}{k_{i-\frac{1}{2},j}} = \frac{k_{i+1,j}}{k_{i-1,j}}\left(\frac{k_{i,j} + k_{i-1,j}}{k_{i,j} + k_{i+1,j}}\right) \quad (3.2.3.4)$$

The lengthwise conservation of energy equations for the inner nodes then becomes for $\gamma = 1$:

$$f_{i,j} = 0 = \left(\frac{1}{8} - \mathrm{Fo}_{\Delta \mathrm{x}}\right) T_{i-1,j}^{\ell+1} + \left(\frac{3}{4} + \mathrm{Fo} k_r + k_r\right) T_{i,j}^{\ell+1} + \left(\frac{1}{8} - \mathrm{Fo} k_r\right) T_{i+1,j}^{\ell+1} - C_e I^2 R - C_W \left[\sigma \varepsilon_L \frac{\xi_i^{\ell+1} - \xi_i^{\ell}}{\Delta t}\right]$$
$$+ C_H \left(\frac{\xi_{i,j}^{\ell+1} - \xi_{i,j}^{\ell}}{\Delta t}\right) - \frac{1}{8}\left(\left(T_{i+1,j}^{\ell} + T_{i-1,j}^{\ell}\right)\right) - \frac{3}{4} T_{i,j}^{\ell} \quad (3.2.3.5)$$

For the surface nodes described by $i \in [2, n_L - 1]$ and $j = n_r$, energy loss from convection and radiation are taken into account such that:

$$
\begin{aligned}
&k_{i-\frac{1}{2},\ j}\pi\left(r^2-(r_j-\frac{\Delta r}{2})^2\right)\frac{T_{i-1,j}^{\ell+\gamma}-T_{i,j}^{\ell+\gamma}}{\Delta x}\\
&\quad=k_{i+\frac{1}{2},\ j}\pi\left(r^2-(r_j-\frac{\Delta r}{2})^2\right)\frac{T_{i,j}^{\ell+\gamma}-T_{i+1,j}^{\ell+\gamma}}{\Delta x}\\
&\quad++2h_{i,n_r}\pi r\Delta x\left(3T_{i,n_r}^{\ell+\gamma}+\frac{T_{i-1,j}^{\ell+\gamma}+T_{i+1,j}^{\ell+\gamma}}{2}-T_{air}\right)+2\epsilon\sigma_b\pi r\Delta x\left(\left[T_{i,n_r}^{\ell+\gamma}\right]^4-{T_{air}}^4\right)\\
&\quad+\left[I^2R+\sigma A_cL\varepsilon_L\frac{\xi_i^{\ell+1}-\xi_i^{\ell}}{\Delta t}\right]\left(\frac{\Delta x}{L}\right)\left(\frac{\left(r^2-(r_j-\frac{\Delta r}{2})^2\right)}{r^2}\right)\\
&\quad+\rho\pi\left((r_j+\frac{\Delta r}{2})^2-(r_j-\frac{\Delta r}{2})^2\right)\Delta x\Delta H\frac{\xi_{i,j}^{\ell+1}-\xi_{i,j}^{\ell}}{\Delta t}\\
&\quad+\rho c_p\pi\left(r^2-(r_j-\frac{\Delta r}{2})^2\right)\frac{\Delta x}{\Delta t}\left[\frac{1}{8}\left(\left(T_{i,j}^{\ell+1}+T_{i,j}^{\ell+1}\right)-\left(T_{i,j}^{\ell}+T_{i,j}^{\ell}\right)\right)+\frac{3}{4}\left(T_{i,j}^{\ell+1}-T_{i,j}^{\ell}\right)\right]
\end{aligned}
\tag{3.2.3.6}
$$

In order to simplify the system the following constants can be defined:

$$C_1=\frac{2h_{i,n_r}\Delta x^2}{k_{i-\frac{1}{2}j}r}\mathrm{Fo}_{\Delta x}=\mathrm{BiFo}_{\Delta x}\left(\frac{\Delta x}{r}\right)^2 \tag{3.2.3.7}$$

$$C_2=\frac{2\epsilon\sigma_b\Delta x^2}{k_{i-\frac{1}{2}j}r}\mathrm{Fo}_{\Delta x} \tag{3.2.3.8}$$

$$C_H=\frac{\rho\Delta x^2\Delta H}{k_{i-\frac{1}{2}j}}\mathrm{Fo}_{\Delta x}=\frac{\Delta H\Delta t}{c_p} \tag{3.2.3.9}$$

$$C_e=\frac{\Delta x^2}{Lk_{i-\frac{1}{2}j}\pi r^2}\mathrm{Fo}_{\Delta x}=\frac{\Delta t}{\rho c_pL\pi r^2} \tag{3.2.3.10}$$

$$C_W=\frac{\Delta x^2}{k_{i-\frac{1}{2}j}}\mathrm{Fo}_{\Delta x}=\frac{\Delta t}{\rho c_p} \tag{3.2.3.11}$$

The lengthwise conservation of energy equations for the inner nodes then becomes for $\gamma = 1$:

$$f_{i,j} = 0 = \left(\frac{1}{8} - \mathrm{Fo}_{\Delta x} + \frac{C_1}{2}\right) T_{i-1,j}^{\ell+1} + \left(\frac{3}{4} + \mathrm{Fo}_{\Delta x} k_r + \mathrm{Fo}_{\Delta x} + 3C_1\right) T_{i,j}^{\ell+1} + \left(\frac{1}{8} - \mathrm{Fo}_{\Delta x} k_r + \frac{C_1}{2}\right) T_{i+1,j}^{\ell+1}$$
$$- C_e I^2 R - 4C_1 T_\infty - C_W \left[\sigma \varepsilon_L \frac{\xi_i^{\ell+1} - \xi_i^{\ell}}{\Delta t}\right] + C_H \left(\frac{\xi_{i,j}^{\ell+1} - \xi_{i,j}^{\ell}}{\Delta t}\right) - \frac{1}{8}\left(\left(T_{i+1,j}^{\ell} + T_{i-1,j}^{\ell}\right)\right) \quad (3.2.3.12)$$
$$- \frac{3}{4} T_{i,j}^{\ell}$$

The two equations that define the boundary conditions for $i = 1$ and $i = n$ for all j will be established based on the fact that the two boundary conditions must be explicitly given. The governing assumption for the boundary conditions will be that the boundaries are far enough from the electric crimps so as to be considered constant at the ambient temperature of the air. Therefore:

$$f_{1,j} = 0 = T_{1,j}^{\ell+1} - T_{air} \quad (3.2.3.13)$$

$$f_{n_x,j} = 0 = T_{n_x,j}^{\ell+1} - T_{air} \quad (3.2.3.14)$$

The Jacobian can then be formulated for each row of nodes and the temperature profile after lengthwise conduction is accounted for can be solved through Euler's method using the form presented in Eq. 3.2.2.31. This process must be iterated to within some error bound.

Radial conduction must then be accounted for in each time step after the temperature changes caused by lengthwise conduction has been computed. For the inner nodes described by $i \in [2, n_L - 1]$ and $j \in [2, n_r]$, the conservation of energy equations are given by:

$$k_{i,j-\frac{1}{2}} 2\pi (r_j - \frac{\Delta r}{2}) \Delta x \frac{T_{i,j-1}^{\ell+\gamma} - T_{i,j}^{\ell+\gamma}}{\Delta r}$$
$$= k_{i,j+\frac{1}{2}} 2\pi (r_j + \frac{\Delta r}{2}) \Delta x \frac{T_{i,\ j}^{\ell+\gamma} - T_{i,\ j+1}^{\ell+\gamma}}{\Delta r} + \rho c_p \pi \left((r_j + \frac{\Delta r}{2})^2 - (r_j - \frac{\Delta r}{2})^2\right) \Delta x \frac{T_{i,j}^{\ell+1} - T_{i,j}^{\ell}}{\Delta t} \quad (3.2.3.15)$$

As before, while this is an adequate discretization, integration across the control volume of the radial heat equation allows for better results. The weak form of the radial heat equation is given by:

$$\int_{r_j-\Delta r/2}^{r_j+\Delta r/2}\left[r\rho c_p\frac{\partial T}{\partial t}-\frac{\partial}{\partial r}\left(kr\frac{\partial T}{\partial r}\right)\right]dr \tag{3.2.3.16}$$

Assuming that each nodal temperature can be connected by lines allows for the Trapezoidal rule to be utilized to perform these integrations. Letting $\gamma = 1$ and performing these integrations generates the following system of equations:

$$\begin{aligned} f_{i,j} = 0 = &\left(\frac{r_j}{2}+\mathrm{Fo}_{\Delta r}+k_r r_r \mathrm{Fo}_{\Delta r}\right)T_{i,j}^{\ell+1}+\left(\frac{3r_j-\Delta r}{12}-\mathrm{Fo}_{\Delta r}\right)T_{i,j-1}^{\ell+1} \\ &+\left(\frac{3r_j+\Delta r}{12}-k_r r_r \mathrm{Fo}_{\Delta r}\right)T_{i,j+1}^{\ell+1}-\frac{r_j}{2}T_{i,j}^{\ell}-\frac{3r_j+\Delta r}{12}T_{i,j+1}^{\ell}-\frac{3r_j-\Delta r}{12}T_{i,j-1}^{\ell} \end{aligned} \tag{3.2.3.17}$$

where:

$$\mathrm{Fo}_{\Delta \mathrm{r}} = \frac{k_{i-\frac{1}{2}j}\left(r_j-\frac{\Delta r}{2}\right)\Delta t}{\rho c_p \Delta r^2} \tag{3.2.3.18}$$

$$k_r = \frac{k_{i,j+\frac{1}{2}}}{k_{i,j-\frac{1}{2}}} = \frac{k_{i,j+1}}{k_{i,j-1}}\left(\frac{k_{i,j}+k_{i,j-1}}{k_{i,j}+k_{i,j+1}}\right) \tag{3.2.3.19}$$

$$r_r = \frac{r_j+\frac{\Delta r}{2}}{r_j-\frac{\Delta r}{2}} \tag{3.2.3.20}$$

For the central control volume given by $j = 1$, the discretized conservation of equations simplify because of symmetry and the conservation of energy for the central control volume is given by:

$$k_{i,j+\frac{1}{2}}2\pi\Delta r\Delta x\frac{T_{i,j+1}^{\ell+\gamma}-T_{i,j}^{\ell+\gamma}}{\Delta r} = \rho c_p \pi\left(\frac{\Delta r}{2}\right)^2\Delta x\frac{T_{i,j}^{\ell+1}-T_{i,j}^{\ell}}{\Delta t} \tag{3.2.3.21}$$

Algebraically manipulating the system to generate a system of equations:

$$f_{i,1} = 0 = T_{i,j+1}^{\ell+\gamma}-T_{i,j}^{\ell+\gamma}-\frac{\rho c_p \Delta r^2}{8k_{i,j+\frac{1}{2}}}\left(\frac{T_{i,j}^{\ell+1}-T_{i,j}^{\ell}}{\Delta t}\right) \tag{3.2.3.22}$$

To simplify this system, the discretized radial Fourier number is redefined for the system of equations reflecting the centerline such that:

$$\mathrm{Fo}_{\Delta \mathrm{r}}|_{j=1} = \frac{k_{i,j+\frac{1}{2}} \Delta t}{\rho c_p \Delta r^2} \tag{3.2.3.23}$$

Letting $\gamma = 1$ and rewriting the system of equations yields:

$$f_{i,1} = 0 = \left(8\mathrm{Fo}_{\Delta \mathrm{r}}|_{j=1}\right) T_{i,2}^{\ell+1} + \left(-1 - 8\mathrm{Fo}_{\Delta \mathrm{r}}|_{j=1}\right) T_{i,1}^{\ell+1} + T_{i,1}^{\ell} \tag{3.2.3.24}$$

Finally, the surface control volume given by $j = n_r$ will be treated as a boundary condition for the radial conduction problem. The Jacobian can then be formulated for each set of radial nodes, and Euler's method can compute the temperature profile for the next time step. The phase fraction for each segment of the actuator can then be computed. From this information, the macroscopic properties of the actuator's discretized sections can be found and the actuator geometry can be computed. One such property, the electrical resistance, is computed by first finding the resistance of each discretized disk via:

$$R_{i,j} = \begin{cases} \rho_e|_{(i,j)} \left(\dfrac{\Delta x}{\pi \left(\left(r_j + \frac{\Delta r}{2}\right)^2 - \left(r_j - \frac{\Delta r}{2}\right)^2 \right)} \right), & j > 1 \\ \rho_e|_{(i,1)} \left(\dfrac{4\Delta x}{\pi \Delta r^2} \right), & j = 1 \end{cases} \tag{3.2.3.25}$$

The total resistance of the actuator is then found from treating the equivalent resistance of all of the rows of nodes as resistors in parallel such that:

$$R = \left(\frac{1}{\sum_{i=n_b}^{i=n_L - n_b} R_{i,1}} + \frac{1}{\sum_{i=n_b}^{i=n_L - n_b} R_{i,2}} + \cdots + \frac{1}{\sum_{i=n_b}^{i=n_L - n_b} R_{i,n_r}} \right)^{-1} \tag{3.2.3.26}$$

Because each axis requires uniform grid spacing, both axes are resized at the end of each time step to accommodate for the actuator strain and Poisson contraction. The convergence criteria is similar to that of the 1-D model.

For each type of solution, the procedures can best be summarized as:

1. Initialize all properties of the system.
2. Compute initial macroscopic properties based on initial phase composition.
3. Compute the voltage applied to the actuator based on the control scheme and find current from Ohm's Law.
4. Use tabulated values of fluid to find the surface averaged Nusselt number and convection coefficient.
5. Use finite difference method to implicitly compute temperature profile at next time step assuming no change in phase composition from the previous time step. The Jacobi method may be over-relaxed without loss of solution stability for over-relaxation constants less than two.
6. Use kinetics equations to compute phase composition at next time step.
7. Repeat steps 5 and 6 but using the updated phase compositions in step 5 to gain better values for the latent heat of transformation and thus more accurate temperature profiles.
8. Update the macroscopic properties of the system for the next time step using Voigt's rule of mixing (includes Poisson's ratio, Young's modulus, electric resistivity, thermal conductivity, coefficient of thermal expansion, etc.).
9. Update the mechanical system and formulate values of wire stress and strain for the next time step.
10. Update the nodal spacing to reflect the change in wire geometries.
11. Repeat steps 3 through 10 until the simulation is complete.

This process can be visualized using a flow chart as shown Figure 14. Where multiple line types are connected to a box, the solid lines are performed first and only followed by the dashed line when some type of error criteria is fulfilled ending the cycle.

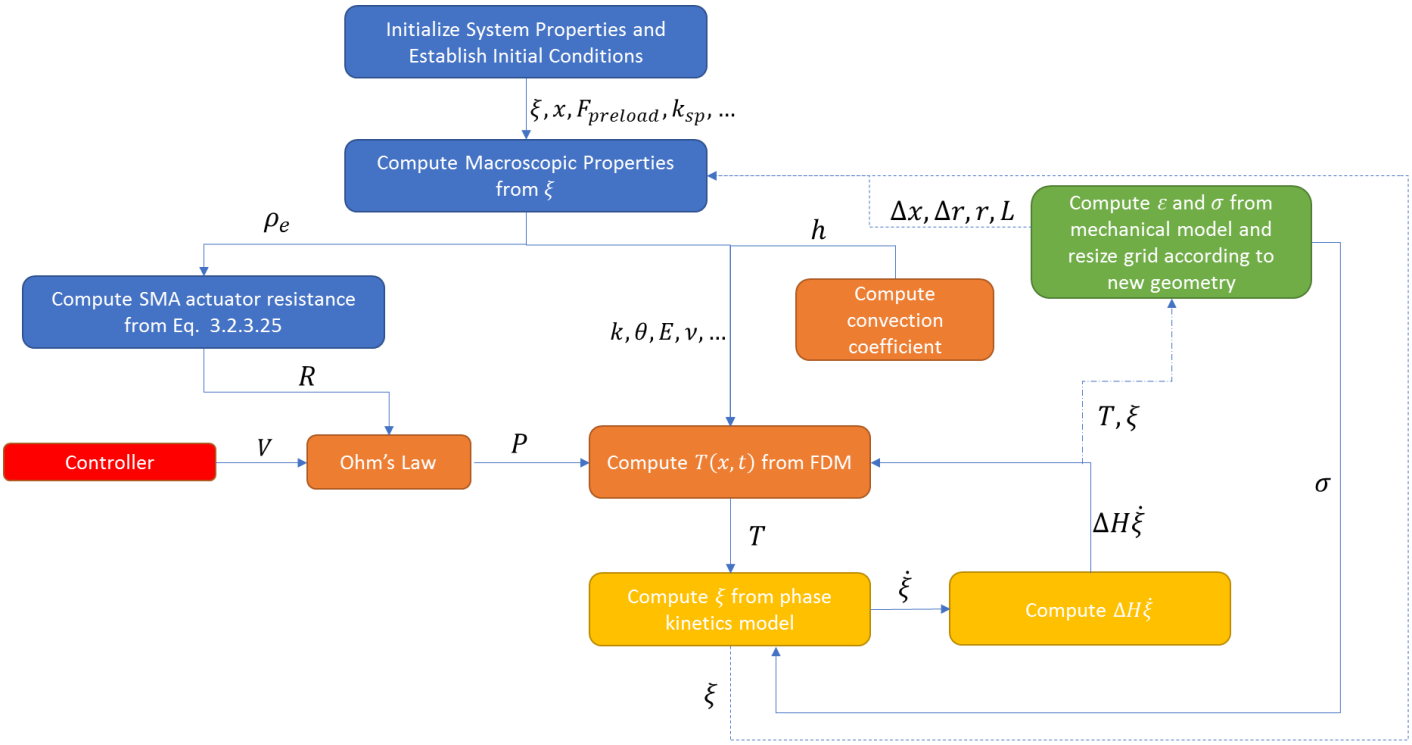

Figure 14. SMA Model Flow Chart

3.2.4 Numerical Simulations and Model Comparisons

Simulations performed to compare the numerical solution during a heating and cooling cycle with the following parameters:

Table 8. Simulation Parameters

Symbol	Variable	Units	Value
Intrinsic Material Properties			
θ_A	Coefficient of Thermal Expansion (Austenite)	1/°C	11E-6
θ_M	Coefficient of Thermal Expansion (Martensite)	1/°C	6.6E-6
ϵ_L	Phase Transformation Strain	N/A	0.04
T_0	Initial Temperature	°C	20
E_A	Elastic Modulus (Austenite)	GPa	75
E_M	Elastic Modulus (Martensite)	GPa	28
υ_A	Poisson's Ratio (Austenite)	-	0.3
υ_M	Poisson's Ratio (Martensite)	-	0.4
ρ_{A0}	Electrical Resistivity (Austenite)	$\mu\Omega$cm	84
ρ_{M0}	Electrical Resistivity (Martensite)	$\mu\Omega$cm	76
α_A	Thermal Effect on Electrical Resistivity (Austenite)	$\mu\Omega$cm /°C	0.05
α_M	Thermal Effect on Electrical Resistivity (Martensite)	$\mu\Omega$cm /°C	0.15
k_A	Thermal Conductivity (Austenite)	$\frac{\mathrm{W}}{\mathrm{mK}}$	18.0
k_M	Thermal Conductivity (Martensite)	$\frac{\mathrm{W}}{\mathrm{mK}}$	8.6
c_p	Specific Heat	J/(kg °C)	836
ΔH	Latent Heat of Transformation	J/g	-24.2
ρ	Density	kg/m^3	6450
Kinetics Model Properties			
M_s	Martensite Start Temperature	°C	42
M_f	Martensite Finish Temperature	°C	32
A_s	Austenite Start Temperature	°C	68
A_f	Austenite Finish Temperature	°C	78
ν_A	Transformation Center Offset Parameter	-	1/8
ν_M	Transformation Center Offset Parameter	-	1
C_A	Effect of Stress on *A*	MPa/°C	6.89
C_M	Effect of Stress on *M*	MPa/°C	6.89
Mechanical Model Parameters			
k_s	Spring Rate	N/m	52.6
c_d	Viscous Damping Coefficient	Ns/m	10.0
d	Actuator Diameter	m	0.000125
L_0	Initial Length	m	0.05
V	Voltage Source	V	3.3
Simulation Parameters			
Δt	Time Step	s	0.00001
n_x	Nodes (lengthwise)	-	101
n_r	Nodes (radially)	-	11

The first simulation was a heating/cooling cycle where a six centimeter span of wire would subject to a 3.7 V heating period of 0.12 seconds before cooling down for two seconds. The results are shown in Figure 15.

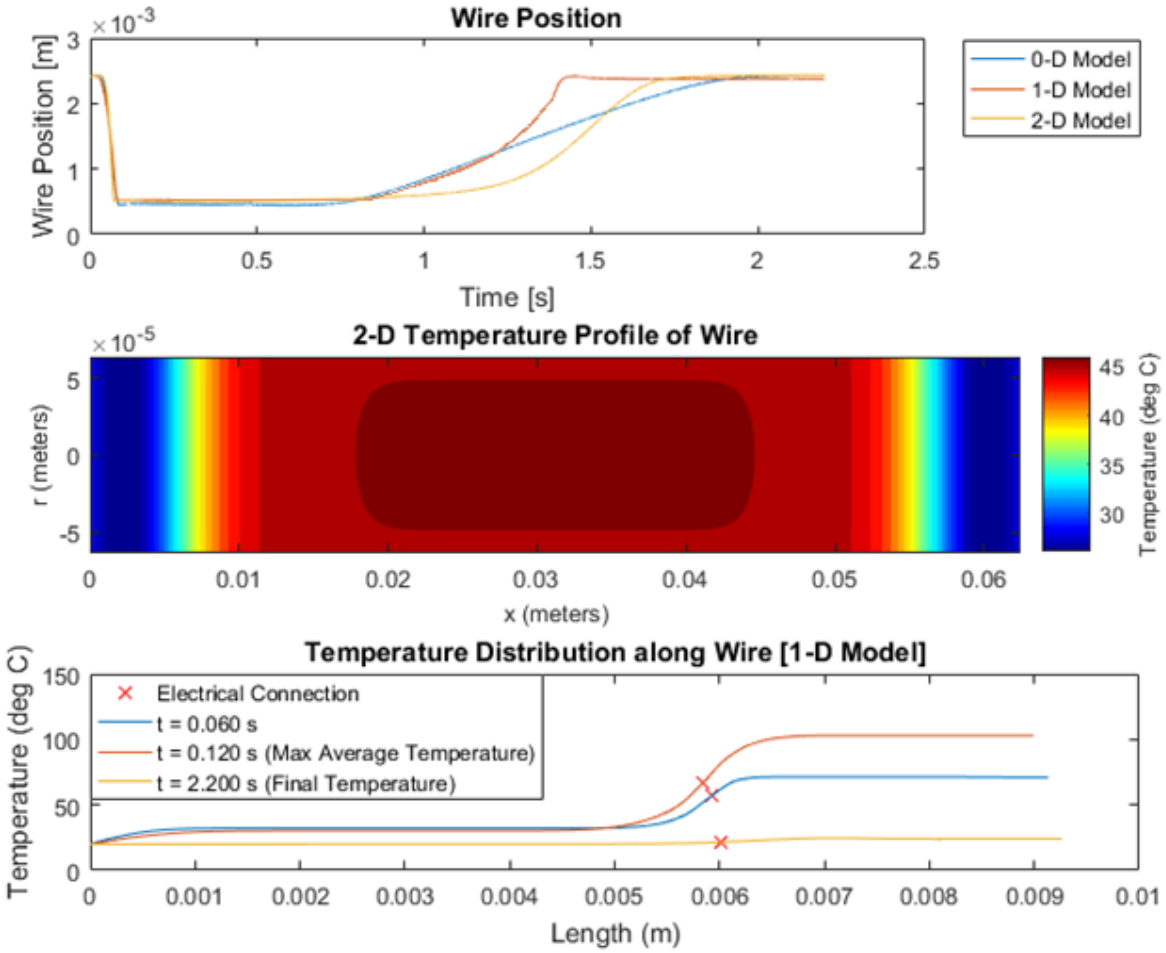

Figure 15. Heating and Cooling Response

This simulation can also be used to show the hysteresis present in each model as a result of the shape memory effect. The wire strain is plotted against the temperature for each model in Figure 16.

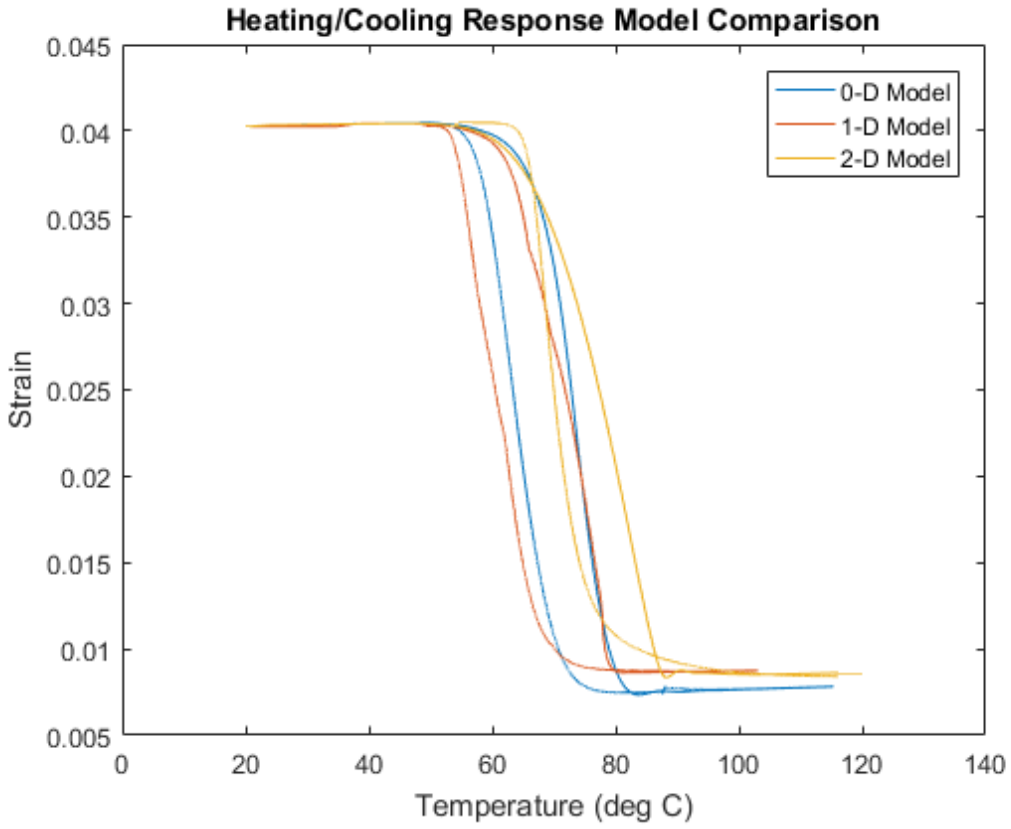

Figure 16. Strain versus Temperature for Heating/Cooling Simulation

Similarly, the wire strain and wire stress are plotted both against time and then against one another in Figure 17. The hysteresis in the response is again very visible.

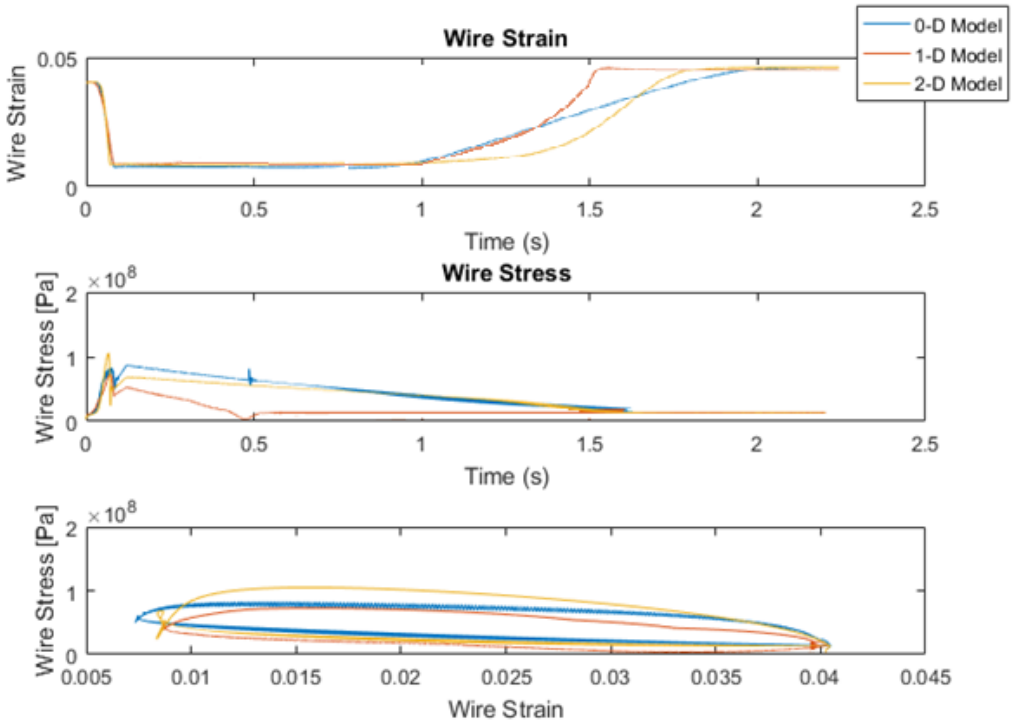

Figure 17. Stress versus Strain for Heating/Cooling Simulation

For the next simulation, a sliding mode controller with a first order sliding surface was then simulated with the control laws with position error e in meters and position error derivative $\dot{e}$ in meters per second being given by:

$$D = 0.65\text{sign}(\dot{e} + 100e) \tag{3.2.4.1}$$

This was simulated for all three discretized models and the simulation results are shown in Figure 18.

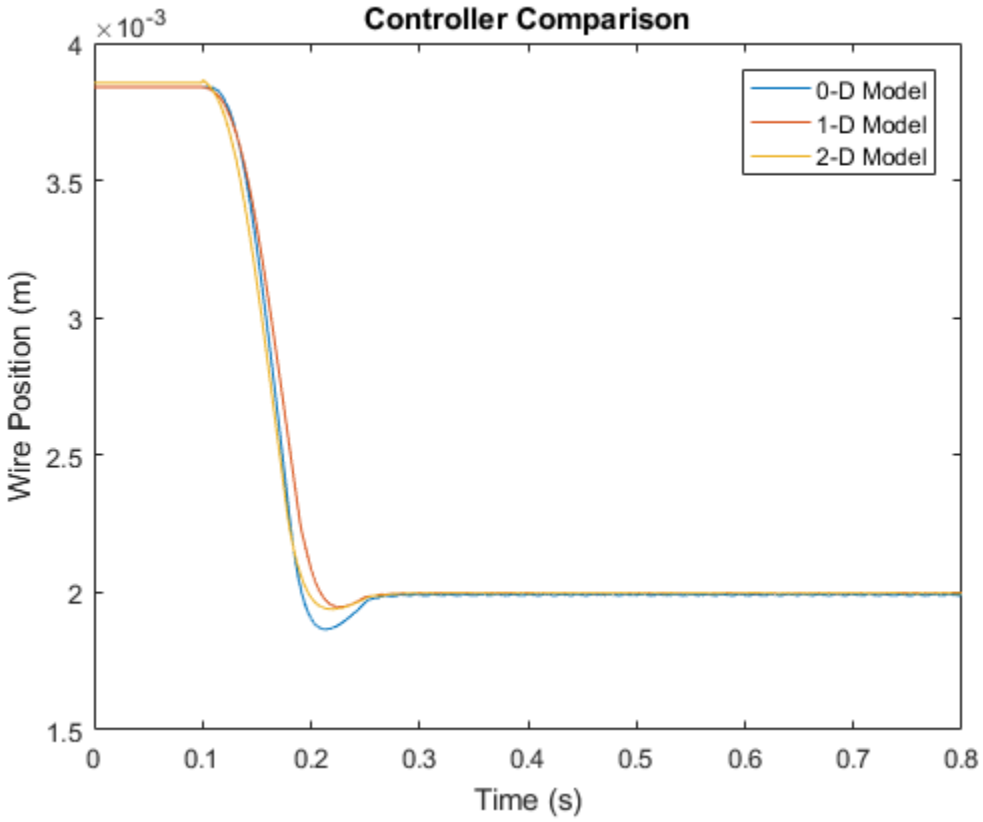

Figure 18. Discretized Model Comparison for Sliding Mode Control

3.3 Experimental Setup

3.3.1 Bandwidth Determination Experiment

Various diameter Dynalloy Flexinol Nitinol wire actuators were driven via an electrical current being passed through it at room temperature. The current, supplied from a 3.3 V PWM signal provided by a microcontroller, heats the wire and causes it to contract. This current was applied over a spectrum of frequencies in order to determine the system bandwidth. The measured change in position of the SMA actuator is the system gain, and this value was normalized so that the DC gain was equal to unity, and the constricted length characteristic of a total phase transformation into Austenite was equal to zero. The measurements of wire position were performed using a self-sensing technique with a probe located along the length of the actuator [78]. The experimental setup is shown in Figure 19.

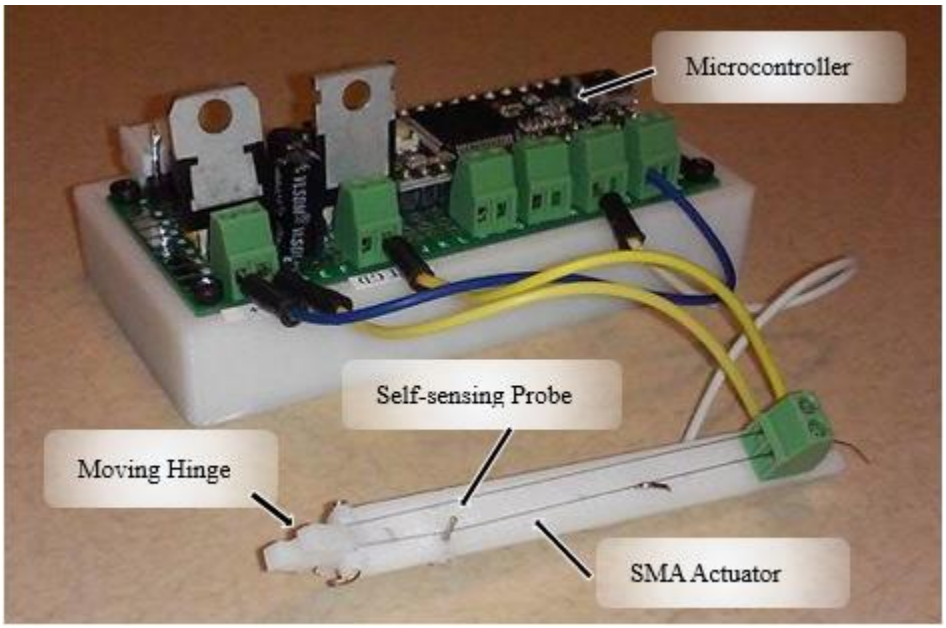

Figure 19. Bandwidth Determination Experiment utilizing SMA Actuator with Self-Sensing Probe

3.3.2 Model Verification with Controller Response

A test platform was constructed in which a shape memory actuator could be connected to a pendulum with an antagonist spring and different controllers could be tested in order to verify the results obtained from the numerical model. The length of the SMA actuator was obtained from three separate position sensors: a rotary encoder, a linear potentiometer, and the slide-sense methodology. The actuator was connected to a load cell so that the axial forces experienced by the actuator could be measured. The data was recorded through the use of a microcontroller and power was supplied by a variable power supply.

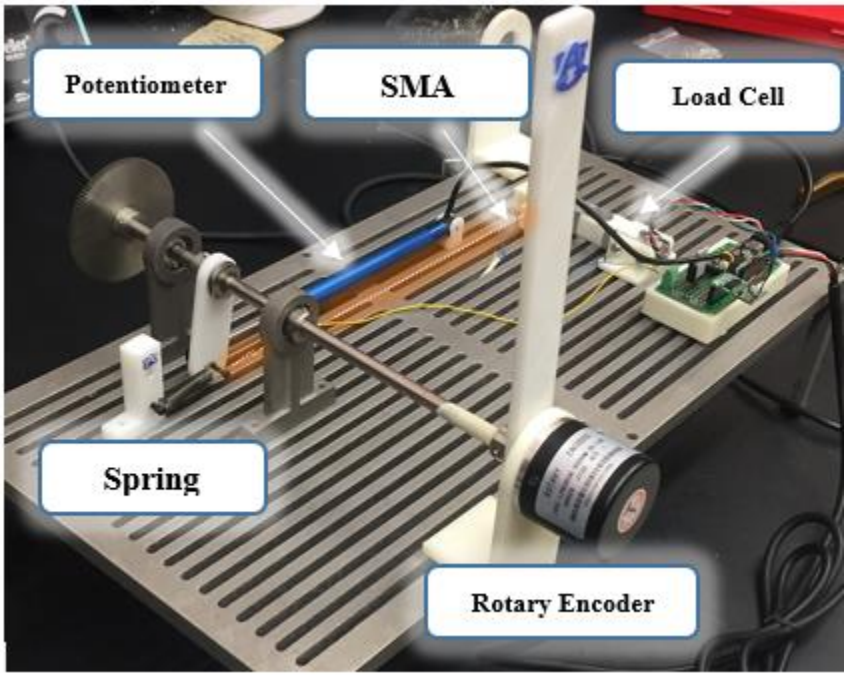

Figure 20. SMA Test Platform

Experiments were performed in order to quantify the properties of the system plant. The spring rate was determined by cycling the actuator through a complete phase transformation and measuring the load cell data versus the wire position measured by the linear potentiometer and utilizing Hooke's Law to find a linear relationship between the quantities (Figure 21).

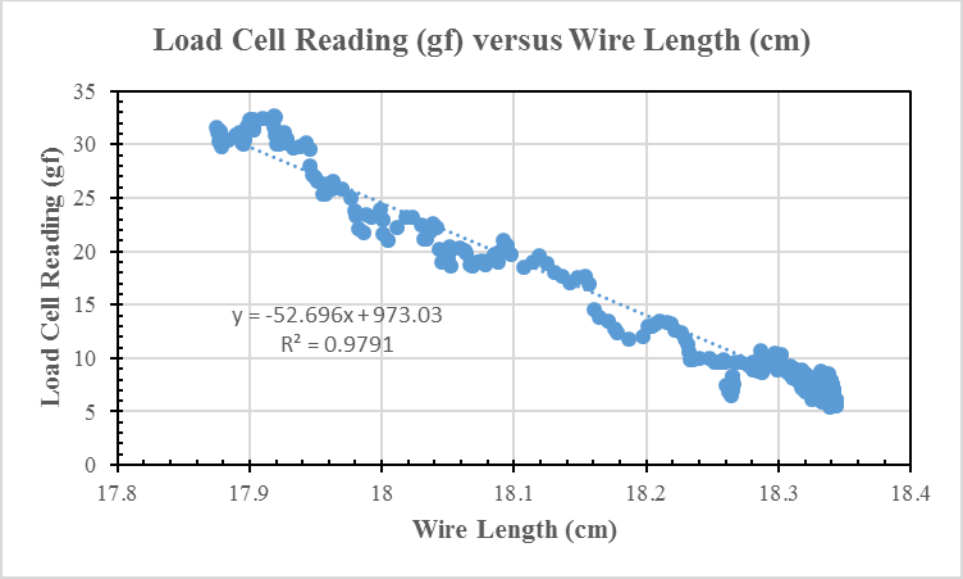

Figure 21. SMA Platform Spring Rate Data

That data can be seen to be sufficiently linear, and applying a linear trend line to the data shows that the system plant has a stiffness coefficient of approximately $k = 52.696\ \frac{\text{gf}}{\text{cm}} = 52.696\ \frac{\text{N}}{\text{m}}$.

The damping coefficient of the plant was obtained through analysis of the transient response of the system to an impulse and modelling the damping as viscous damping. Because the viscous damping model was utilized, the damping coefficient was determined from an analysis of the logarithmic decrement, δ, given by:

$$\delta = \frac{1}{n}\ln\left(\frac{x(t)}{x(t+nT)}\right) \tag{3.3.2.1}$$

$x(t)$ denotes the amplitude at time t and $x(t+nT)$ represents the amplitude of the signal n peaks away from the original measurement. The logarithmic decrement is related to the damping ratio coefficient via:

$$\zeta = \frac{1}{\sqrt{1 + \left(\frac{2\pi}{\delta}\right)^2}} \tag{3.3.2.2}$$

In order to isolate the effects of phase transformation on the damping coefficient, the impulse was applied to the system when the wire remained hot during the response (Figure 22) and when the wire remained cold during the response (Figure 23)

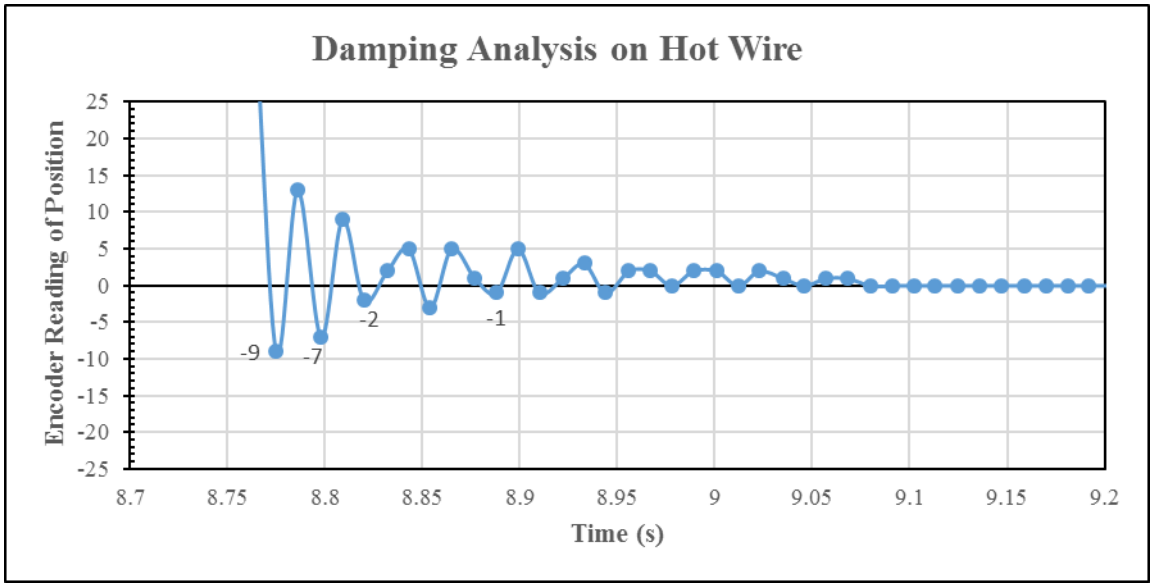

Figure 22. SMA Test Platform Damping Analysis (Hot Wire)

The logarithmic decrement between peaks was found for the hot wire analysis such that:

$$\delta_{1-2} = \ln\left(\frac{9}{7}\right) = 0.2513 \tag{3.3.2.3}$$

$$\delta_{2-3} = \ln\left(\frac{7}{2}\right) = 1.2527 \tag{3.3.2.4}$$

This process was continued for each peak and the results were averaged to get an effective logarithmic decrement of 0.63344. From Eq. 3.3.2.2, the damping ratio is then:

$$\zeta_{hot} = \frac{1}{\sqrt{1 + \left(\frac{2\pi}{0.63344}\right)^2}} = 0.10036 \tag{3.3.2.5}$$

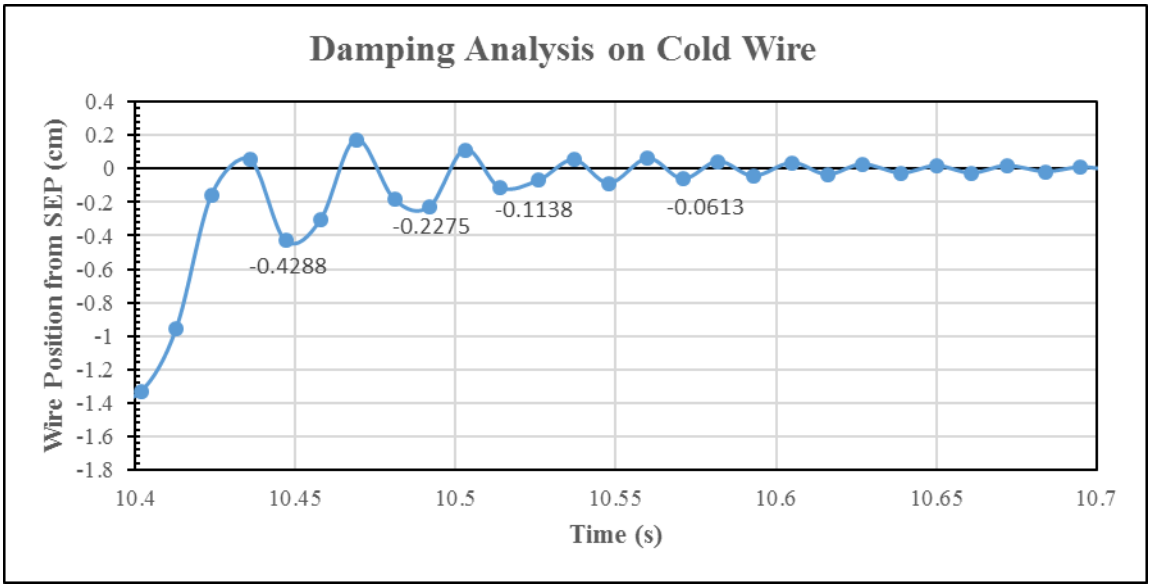

Figure 23. SMA Test Platform Damping Analysis (Cold Wire)

The logarithmic decrement between peaks was found for the hot wire analysis such that:

$$\delta_{1-2} = \ln\left(\frac{0.4288}{0.2275}\right) = 0.63384 \tag{3.3.2.6a}$$

$$\delta_{2-3} = \ln\left(\frac{0.2275}{0.1138}\right) = 0.6927 \tag{3.3.2.6b}$$

This process was continued for each peak and the results were averaged to get an effective logarithmic decrement of 0.537097. From Eq. 3.3.2.2, the damping ratio is then:

$$\zeta_{cold} = \frac{1}{\sqrt{1 + \left(\frac{2\pi}{0.537097}\right)^2}} = 0.08571 \tag{3.3.2.7}$$

The hot wire causes the system to be more heavily damped, which is indicative of energy loss during phase transformation. The effective viscous damping ratio of the system for this analysis is taken to be the average between the hot and cold wire values such that:

$$\zeta_{plant} = \frac{\zeta_{hot} + \zeta_{cold}}{2} = 0.093035 \tag{3.3.2.8}$$

The damping coefficient with the SMA actuator replaced by a spring was also computed for comparison.

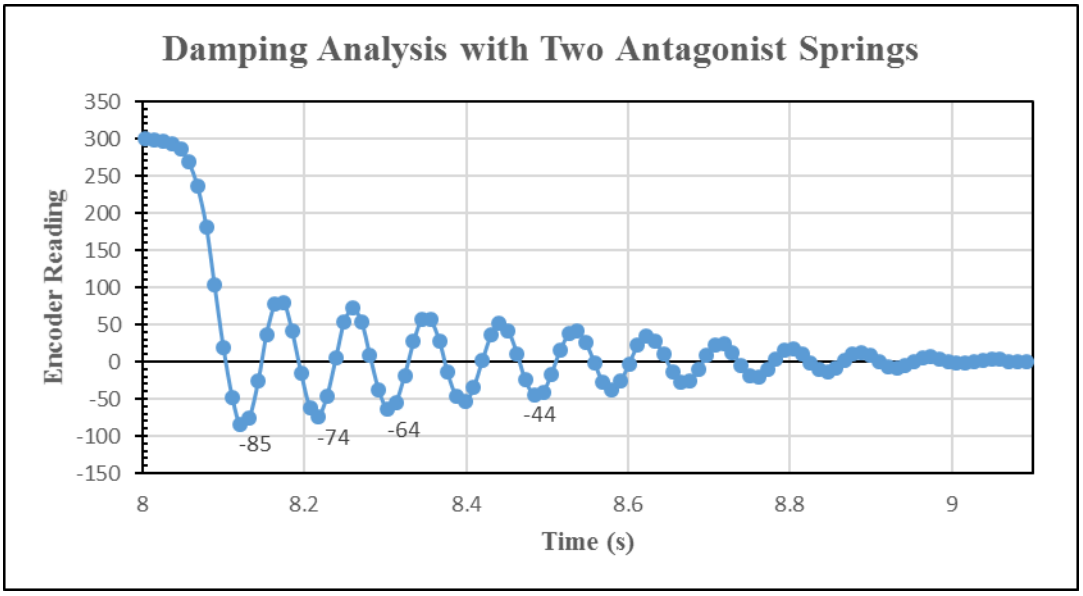

Figure 24. SMA Platform Damping Analysis (Two Antagonist Springs)

The logarithmic decrement analysis would reveal a damping ratio of 0.030226 that is more consistent peak to peak, but also much lower than the computed damping ratio of the plant. This confirms that friction losses in the bearing constitute only a small portion of the overall damping effects in the system, and losses in the SMA wire constitute the majority of the losses. From Figure 24, the damped natural frequency can be obtained as approximately 11 Hz. The natural frequency of the system is then given by:

$$\omega_n = \frac{\omega_d}{\sqrt{1-\zeta^2}} \tag{3.3.2.9}$$

The natural frequency of the system can then be obtained as 69.119 radians per second, which can be related to the plant inertia from:

$$m = \frac{k}{{\omega_n}^2} \tag{3.3.2.10}$$

Substitution of the stiffness found from Figure 21 into this expression yields a system inertia of 0.01103 kg. The critical damping coefficient of the system is then given by:

$$c_{cr} = 2\sqrt{mk_{sp}} = 1.529\ \frac{\text{Ns}}{\text{m}} \tag{3.3.2.11}$$

The system damping coefficient is then determined from the definition of the damping ratio:

$$c = c_{cr}\zeta_{plant} = 2\sqrt{mk} = 0.093035\left(1.529\ \frac{\text{Ns}}{\text{m}}\right) = 0.1423\ \frac{\text{Ns}}{\text{m}} \tag{3.3.2.12}$$

3.3.3 Model Verification with Temperature Response and Boundary Effects

An experiment dedicated to verifying the heat transfer models was developed by connecting SMA wire actuators into a tensile testing machine. The density of the wire actuator was determined by weighing the wire and dividing its weight by its volume. The electrical resistivity of the wire was likewise determined by measuring its resistance and using the definition of electrical resistivity. The SMA wire actuators were connected to a variable power supply by soldering wires to crimps that were crimped to the SMA actuator. This allowed for a precise measurement of the distance between the two crimps. The wires were then connected to the variable power supply through the use of alligator clips. The resistance of the alligator clips and the wires soldered to the crimps were measured for use in running of the simulations. The length of wire electrically connected and the length of wire outside of the crimps were both measured before the experiment.

A 36 AWG K-type thermocouple was verified to accurately log data, and then was electrically insulated and placed in contact with the wire actuator. Heating and cooling curves were logged for various voltages passing through various diameter SMA actuators in order to verify the model. In order to isolate the thermal model from the phase kinetics and mechanical modelling, superelastic wire was used because it would remain in the Austenite phase for the duration of the experiment. Shape memory wires were then used to test the interactions between the kinetics model and the thermal modelling. Finally, a FLIR camera was used to examine the boundary effects for comparison with the discretized modelling.

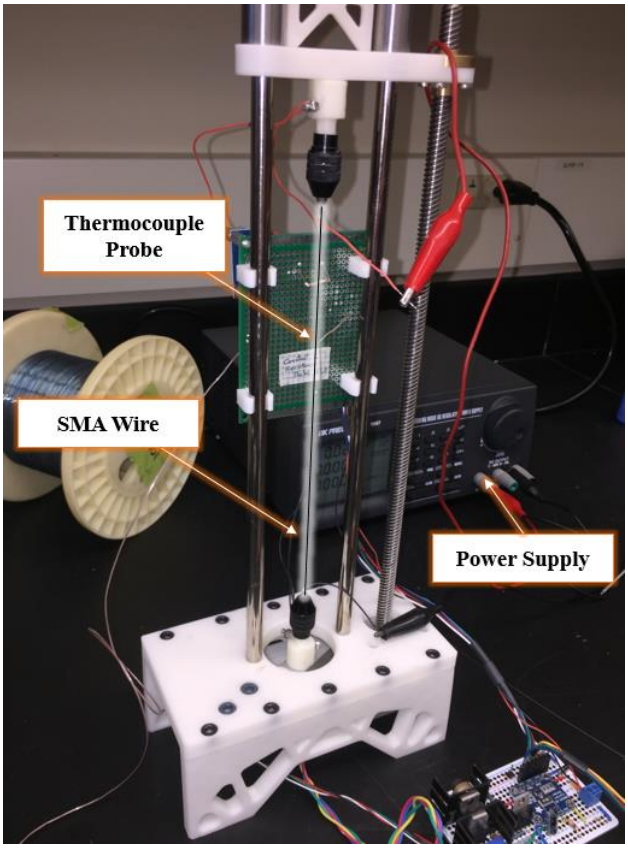

Figure 25. Ohmic Heating Experiment

3.4 Results and Conclusions

3.4.1 Bandwidth Determination

The frequency response of a 0.125 mm diameter actuator from an increasing sinusoidal input with frequencies ranging from 0 to 1.4 Hz is provided in Figure 26, with the cutoff frequency being graphically denoted by the star symbol.

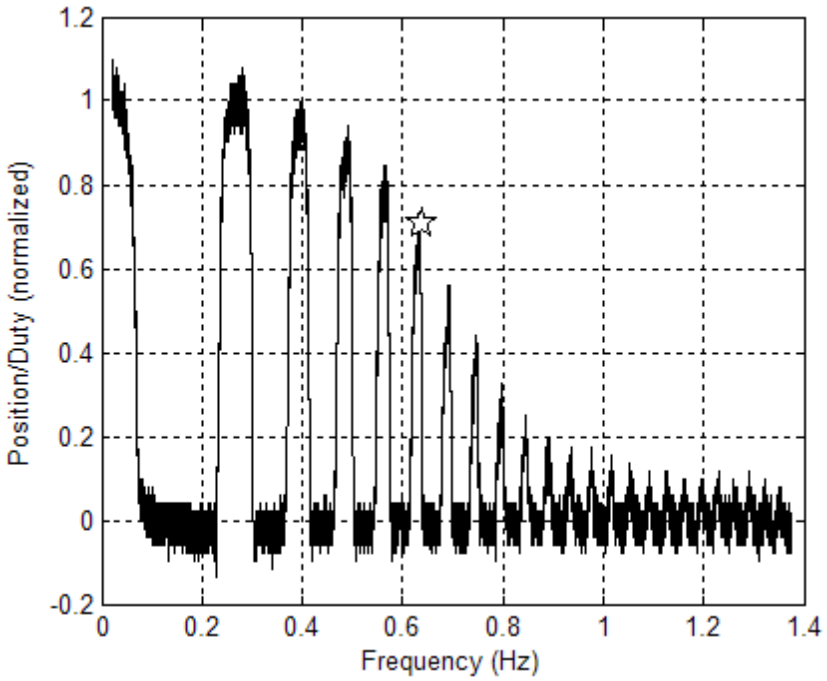

Figure 26. Sinusoidal Sweep Results (0.125 mm diameter)

The results of this experiment show that at a frequency of approximately 0.65 Hz, the gain has shifted –3 dB (to about 70.7%) of its DC value. The corrected bandwidth derived from the analytical solution would predict a system bandwidth of 0.5504 Hz, which carries fifteen percent error when compared to the experimental results. This is because this solution utilizes a correction factor based on the complete temperature range experienced by the actuator which is likely to carry some error and because this value neglects the impact of changes in the crystalline structure of the SMA actuator. The transformation bandwidth formulation predicts a transformation bandwidth of

0.6304 Hz, assuming the wire remains horizontal during operation. This value has a three percent error with the experimental results.

The frequency response of a 0.3 mm diameter actuator from an increasing sinusoidal input with frequencies ranging from 0 to 0.12 Hz is provided in Figure 26, with the cutoff frequency being denoted graphically with a star symbol.

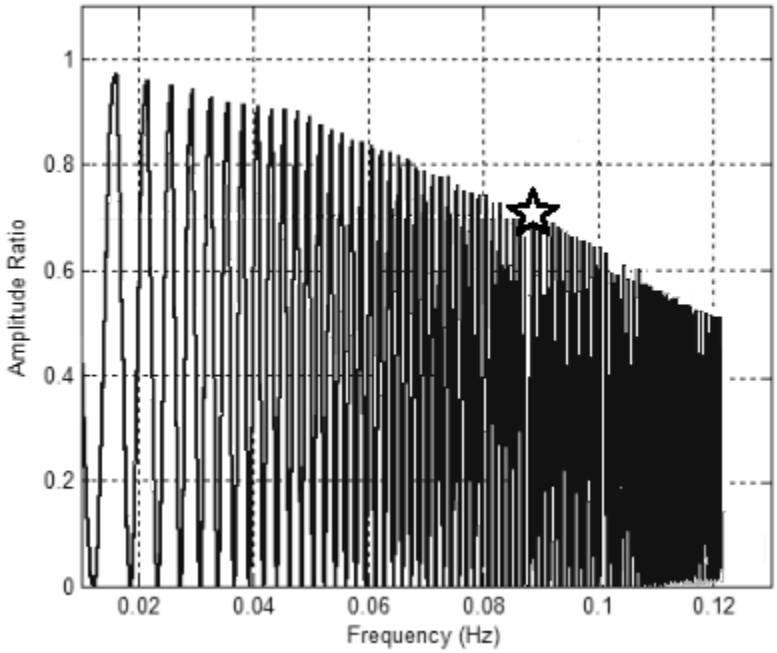

Figure 27. Sinusoidal Sweep Results (0.3 mm diameter)

The results of this experiment show that at a frequency of approximately 0.09 Hz, the gain has shifted –3 dB (to about 70.7%) of its DC value. The corrected bandwidth derived from the analytical solution would predict a system bandwidth of 0.0956 Hz, which carries approximately six percent error when compared to the experimental results. The transformation bandwidth formulation predicts a system bandwidth of 0.11 Hz, which carries a twenty percent error when compared to the experimental results.

Error is the numerically based bandwidth formulations are attributed to the system being non-ideal, as Eq. 3.1.11 is derived for ambient, still air with a temperature of 25 degrees Celsius. If the ambient temperature is significantly different than room temperature, or there is air movement around the wire, then this approximation will experience some degree of error. Also, if the fundamental assumption that the rate of cooling matches the rate of heating is violated, and the speed at which the wire heats up is significantly different than the speed at which it cools, this will also lead to a degree of error because the numerically based bandwidth formulation assumes comparable rates of heating and cooling. Because the rate of cooling is faster for smaller diameter wires, this assumption becomes more applicable for smaller wires and less applicable for larger ones. As a result, the analytically based bandwidth estimate is sufficient for larger actuators and the numerically based bandwidth estimate is more suitable for smaller actuators. An additional source of error comes from the self-sensing measurement technique. This technique provides a resolution of 1.5 degrees out of 90 degrees of travel, or about 0.0167 on the normalized plot of position, limiting the accuracy at which the system bandwidth can be obtained.

3.4.2 Model Verification with Controller Response

The experiment used sliding mode control with a second order sliding surface to drive the wire to a reference position. The simulations were compared to the experimental results and are provided in Figure 28.

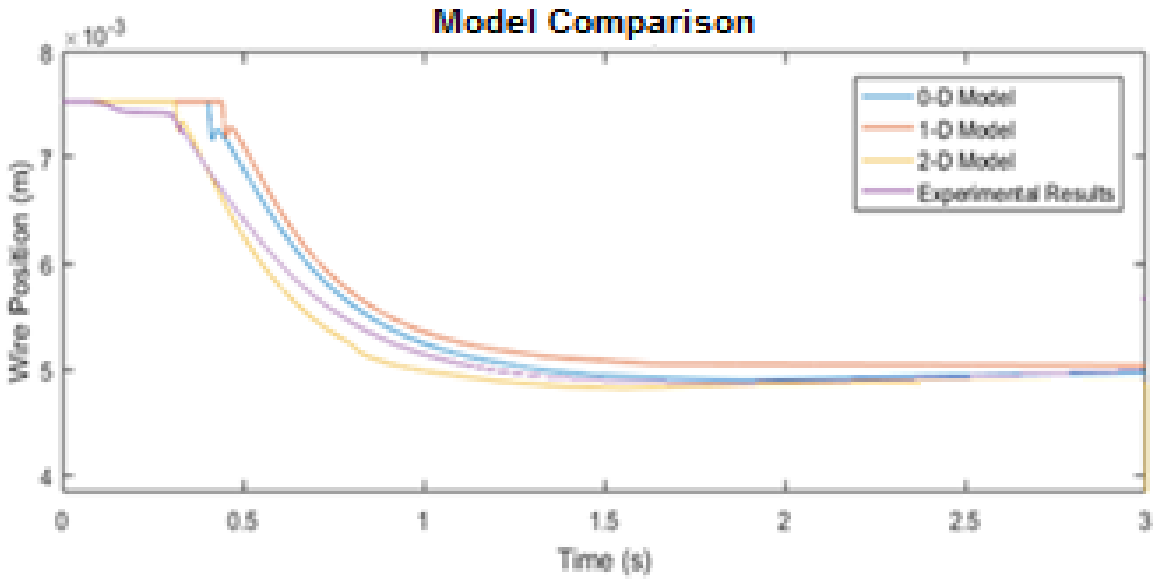

Figure 28. Experimental Results (MATLAB Simulation vs. Experiment for SMC)

As expected, the 2-D model most accurately captured the transient response and all three models converge to the reference position in similar time and in accordance to the experiment. The controller was predicted to be stable with very little overshoot, which is the predicted response and what was observed in the experiment.

3.4.3 Model Verification with Thermal Response and Boundary Effects

The thermocouple was initially placed into ice water and removed into room temperature air in order test if it could accurately read both zero degrees Celsius and room temperature. The thermocouple was found to adequately display both freezing temperatures and room temperatures with a time constant of approximately three seconds (Figure 29).

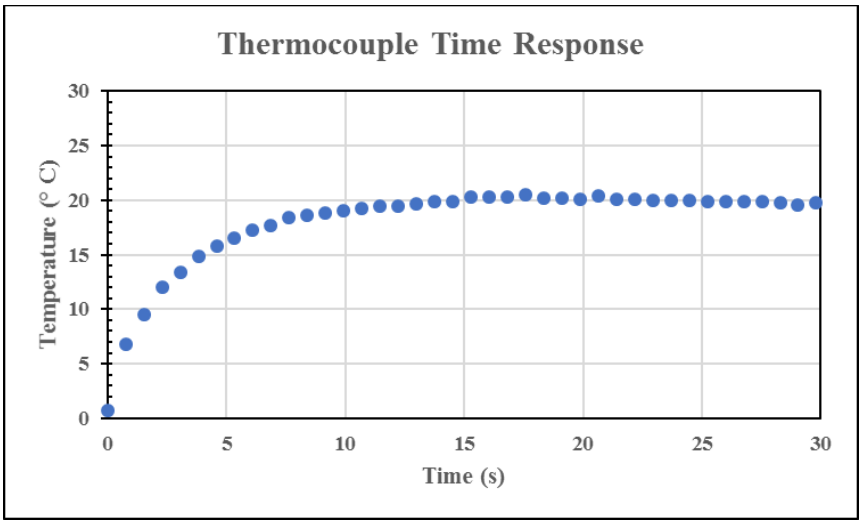

Figure 29. Thermocouple Measurement Validation

The experiments were carried out in accordance to parameters found in Table 9.

Table 9. Model Verification Experiment Log

	Wire Length (cm)	Wire Diameter (mm)	Applied Voltage (V)	Wire Type	Wire Density ($\frac{kg}{m^3}$)	Electric Resistivity ($\mu\Omega$ cm)
Run #1	18.0	0.5	1.6	Superelastic	7666	10.0
Run #2	18.0	0.5	2.0	Superelastic	7666	10.0
Run #3	18.0	0.5	2.5	Superelastic	7666	10.0
Run #4	18.0	0.5	3.0	Superelastic	7666	10.0
Run #5	21.0	0.25	1.0	Superelastic	6450	10.0
Run #6	21.0	0.25	2.0	Superelastic	6450	10.0
Run #7	21.0	0.25	3.0	Superelastic	6450	10.0
Run #8	19.5	0.375	2.5	Shape Memory	6450	*A*: 84 *M*: 76

The experimental data is compared directly to the lumped capacitance modelling which accounts for heat loss from thermal conduction to the boundaries, convection to the air, thermal radiation to the surroundings, and the latent heat of transformation (where applicable).

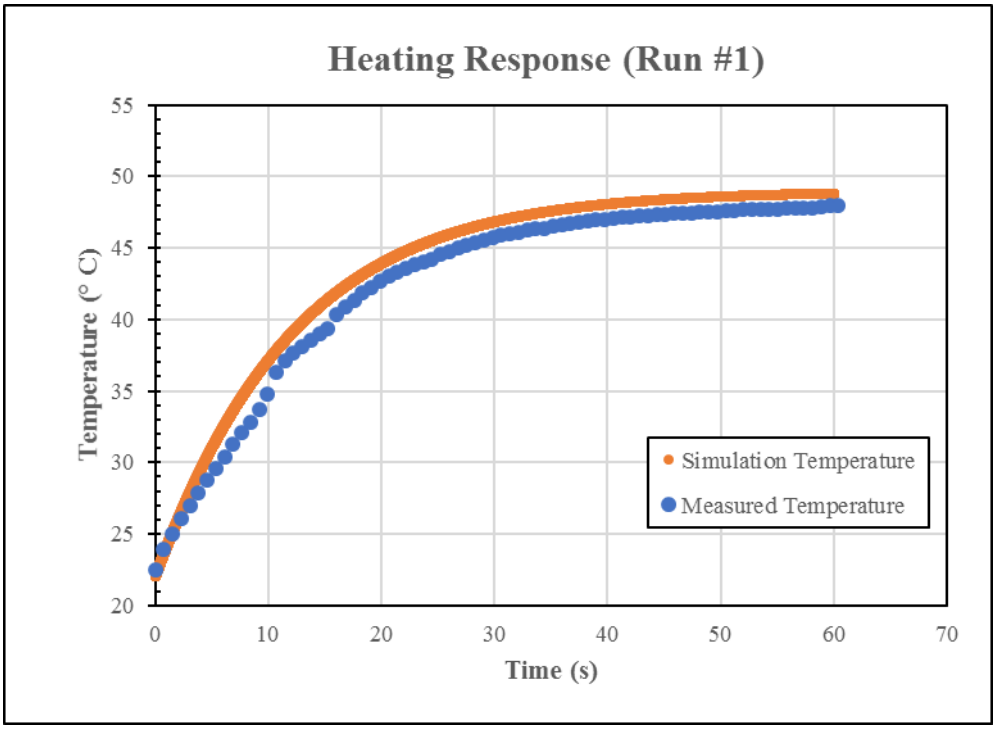

Figure 30. Heating Response (Run #1)

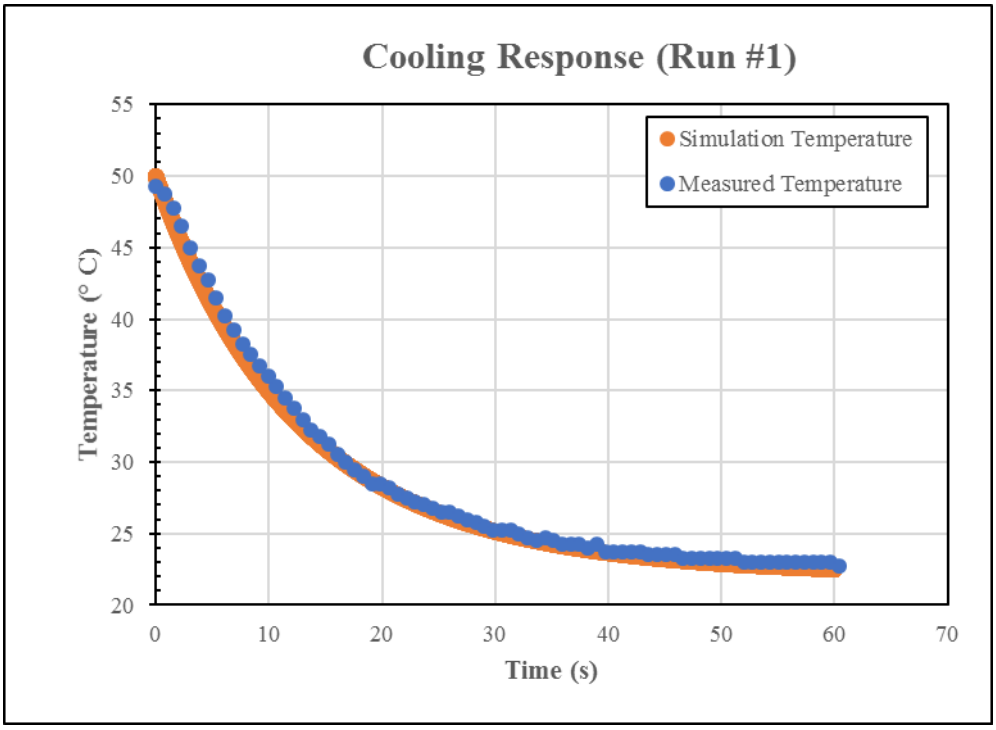

Figure 31. Cooling Response (Run #1)

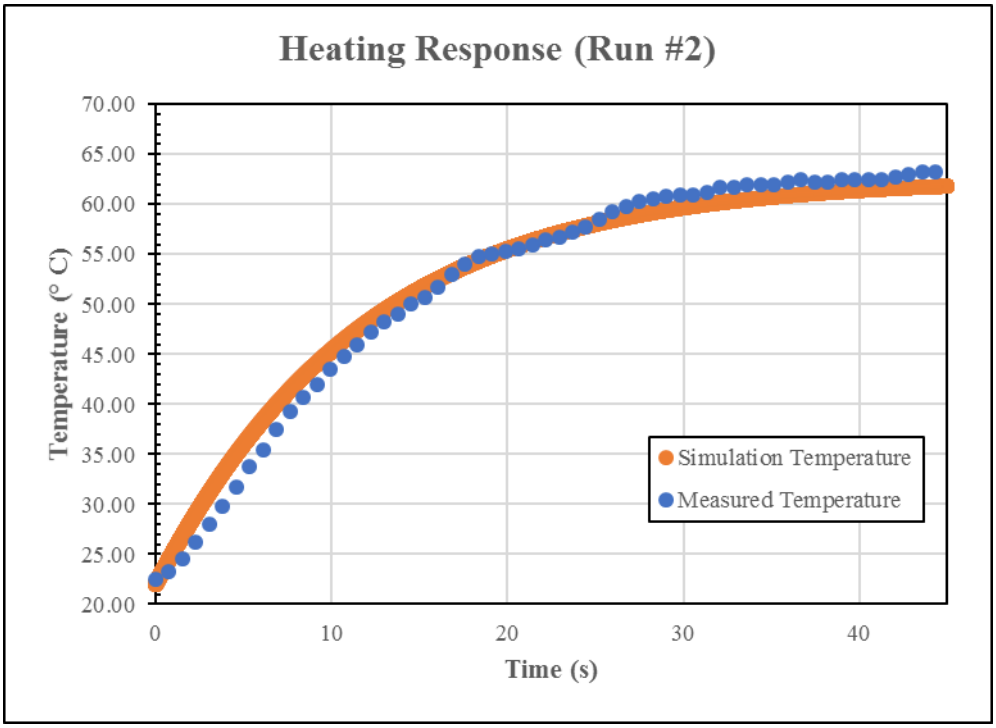

Figure 32. Heating Response (Run #2)

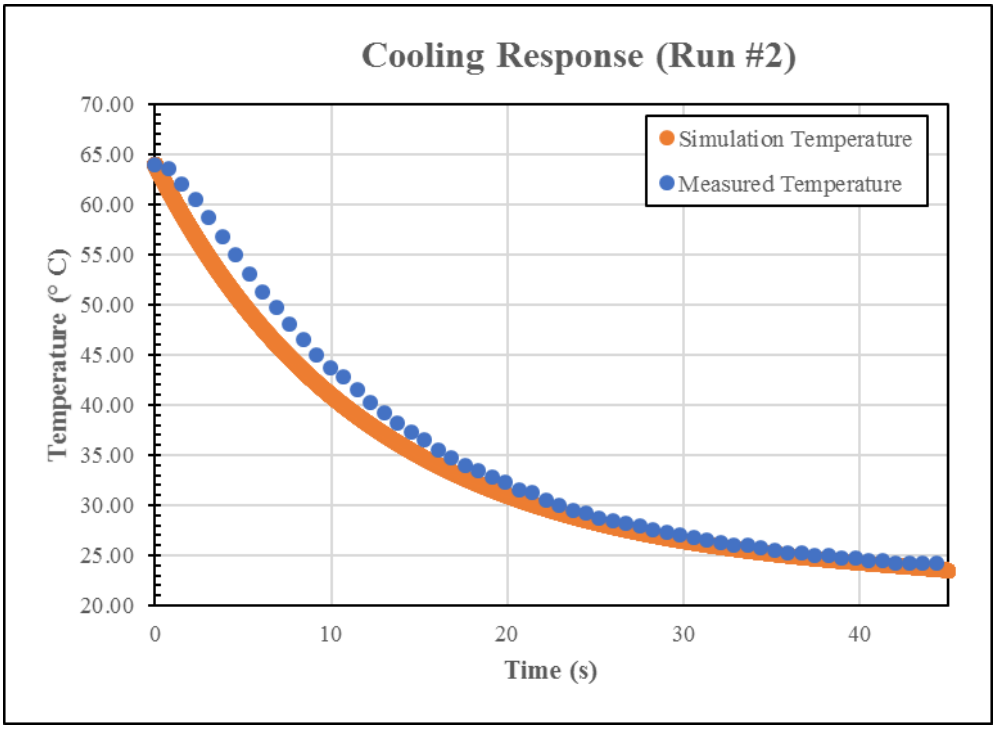

Figure 33. Cooling Response (Run #2)

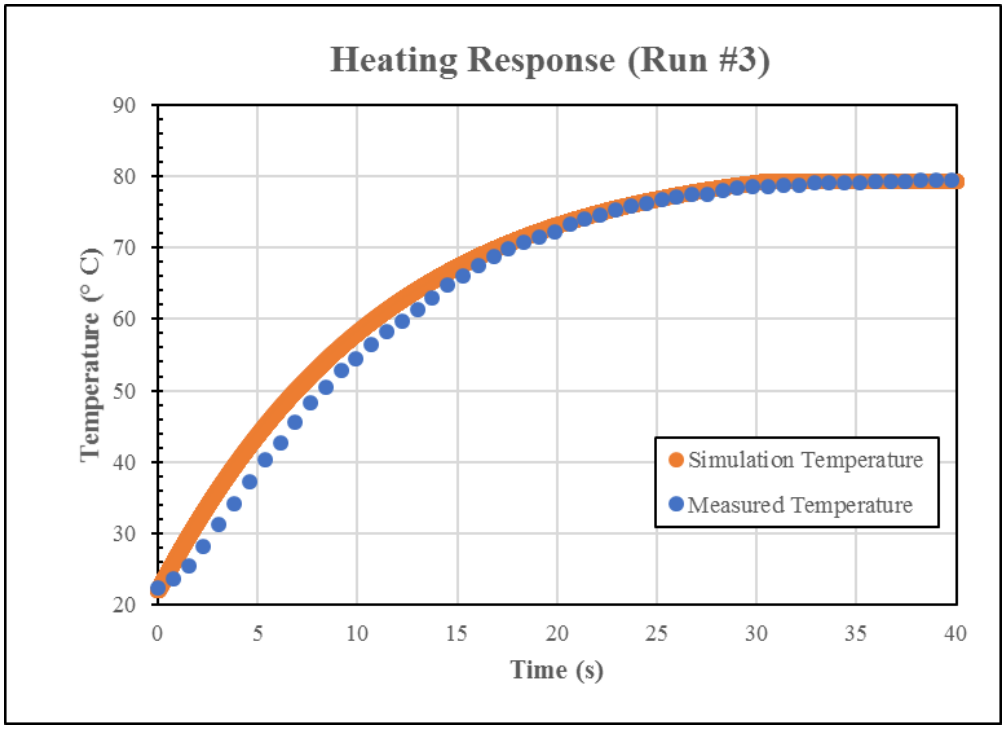

Figure 34. Heating Response (Run #3)

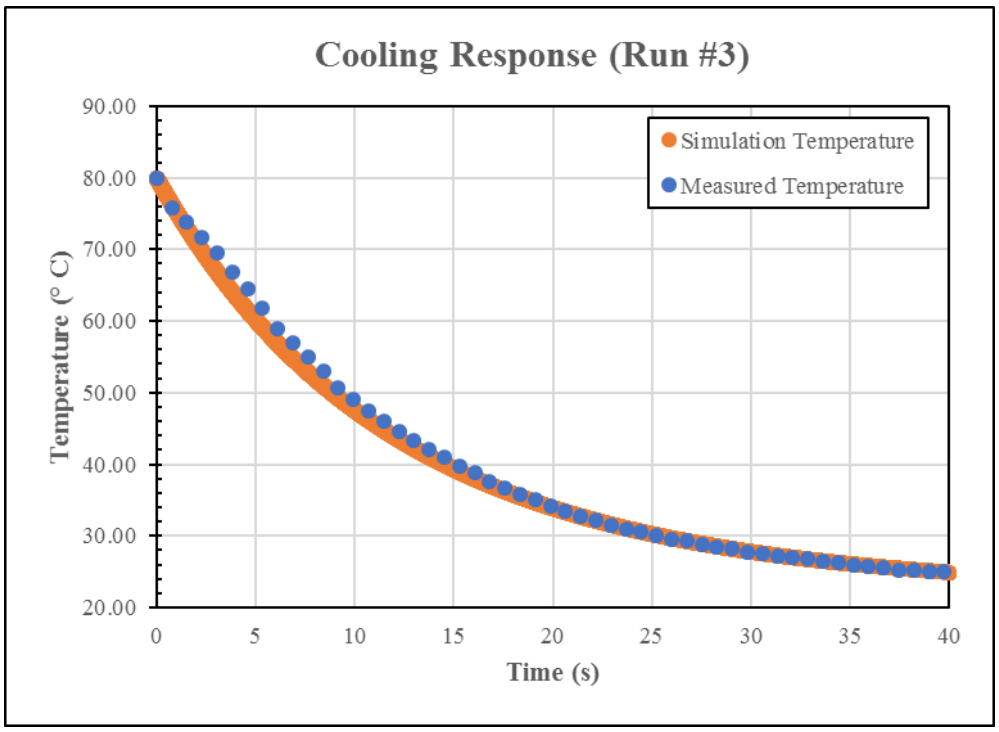

Figure 35. Cooling Response (Run #3)

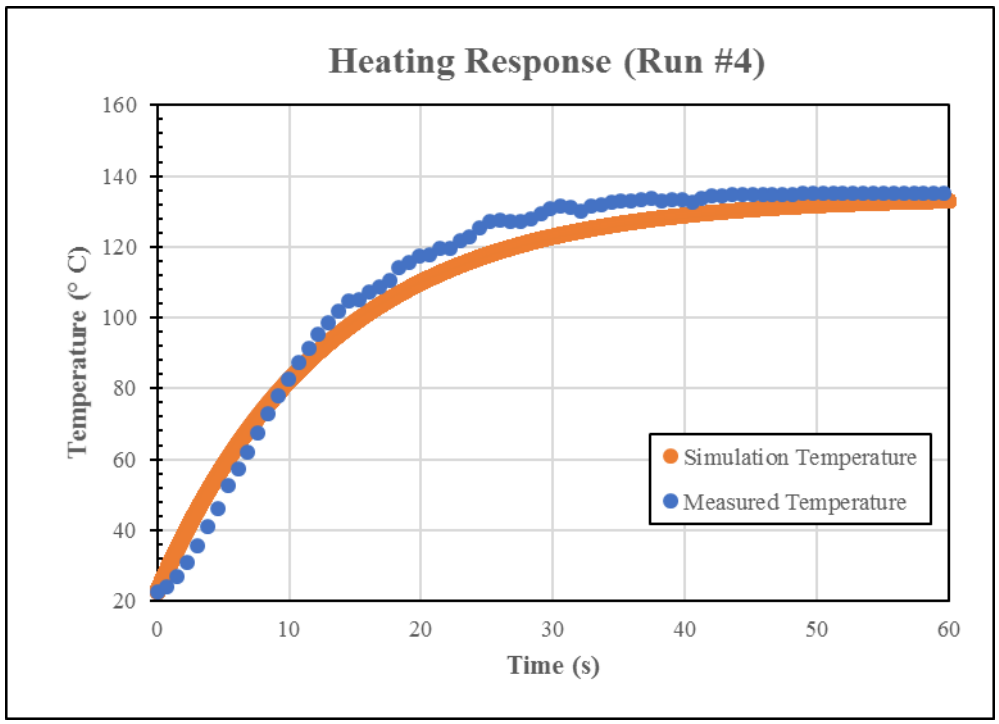

Figure 36. Heating Response (Run #4)

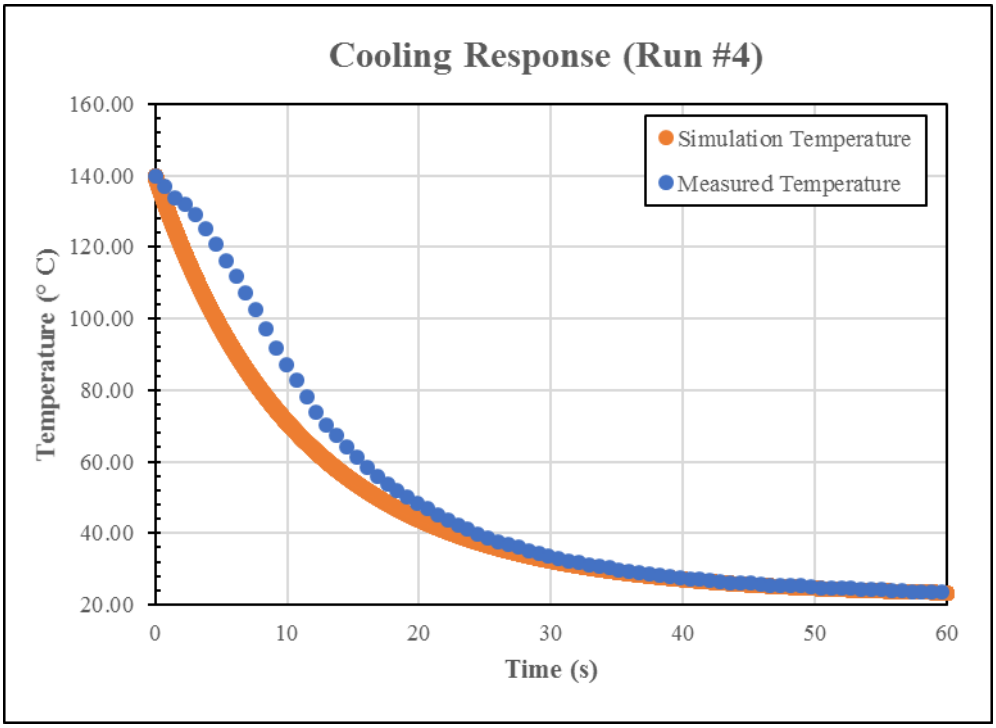

Figure 37. Cooling Response (Run #4)

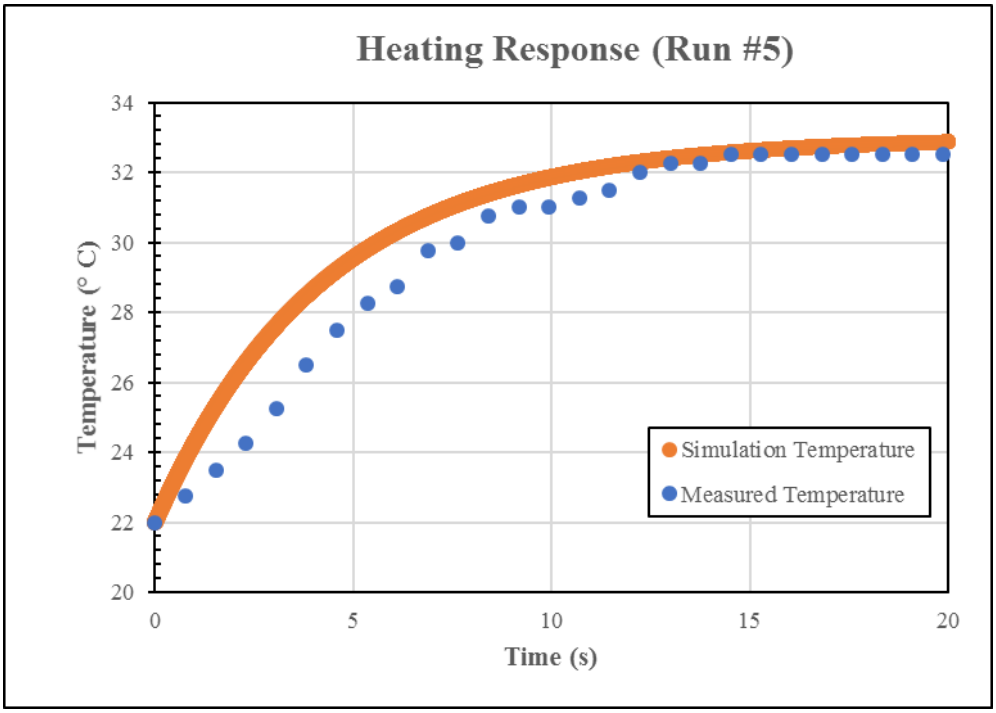

Figure 38. Heating Response (Run #5)

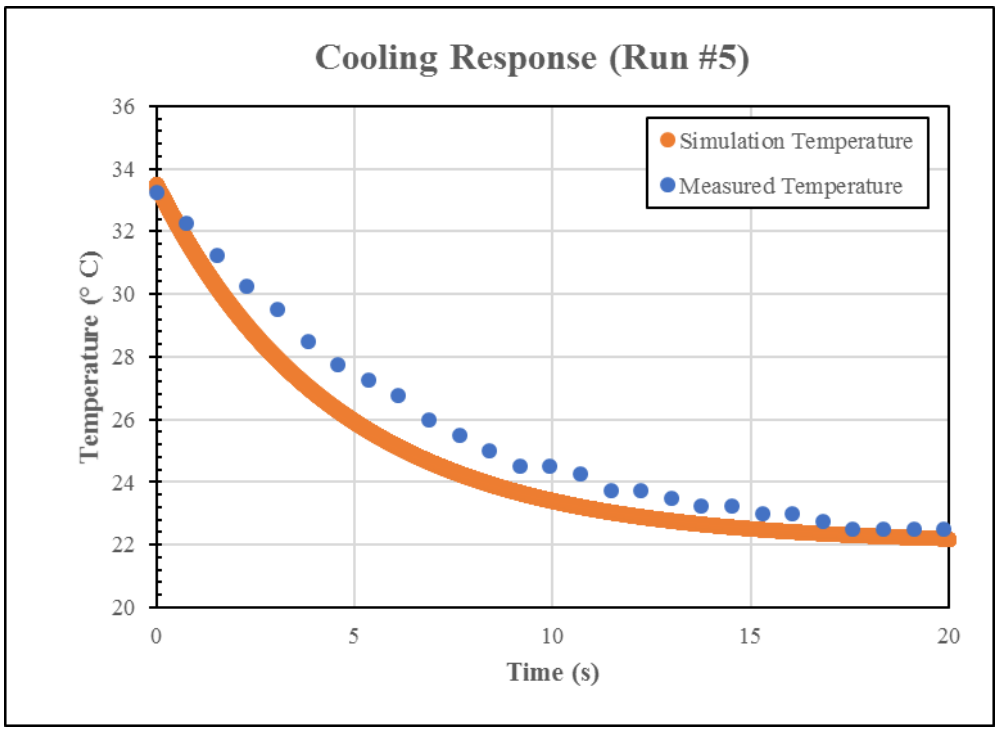

Figure 39. Cooling Response (Run #5)

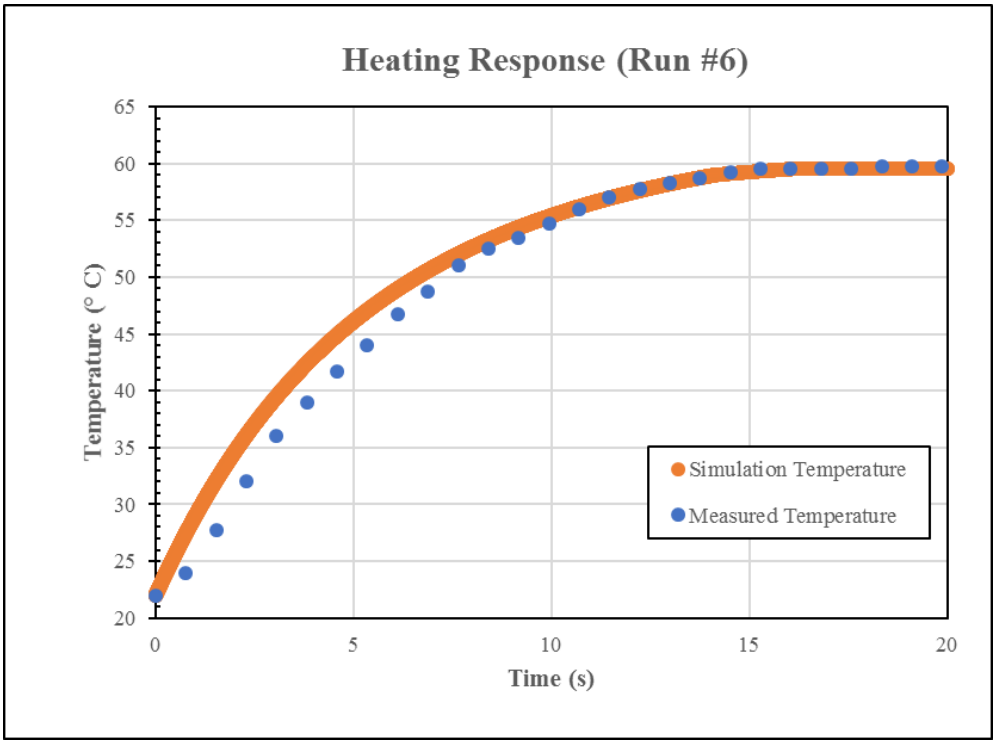

Figure 40. Heating Response (Run #6)

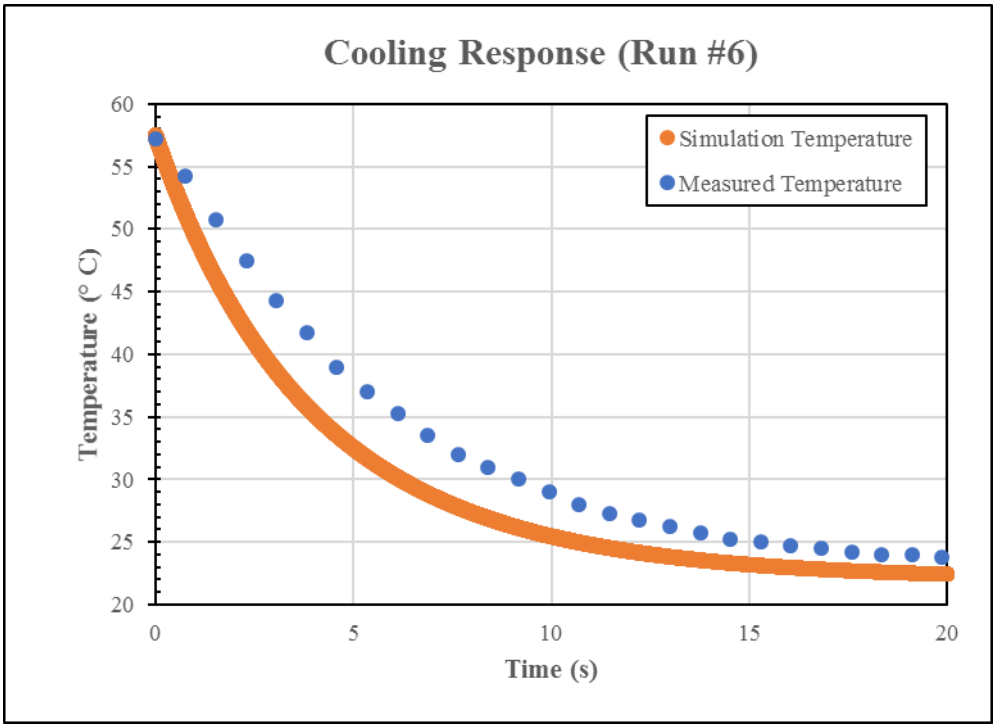

Figure 41. Cooling Response (Run #6)

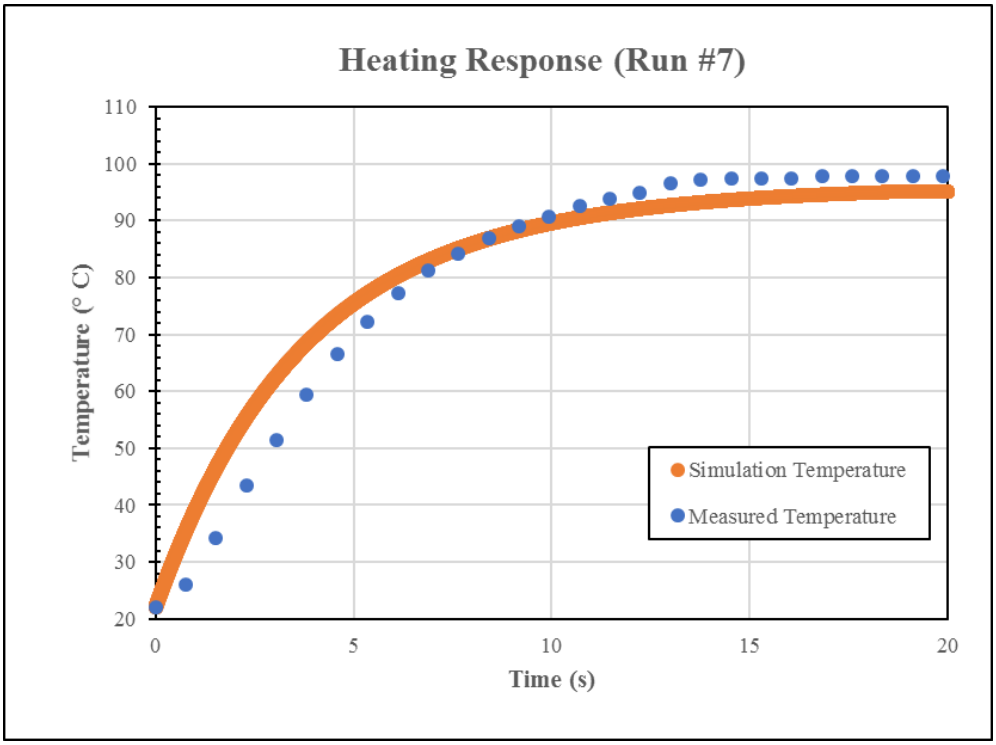

Figure 42. Heating Response (Run #7)

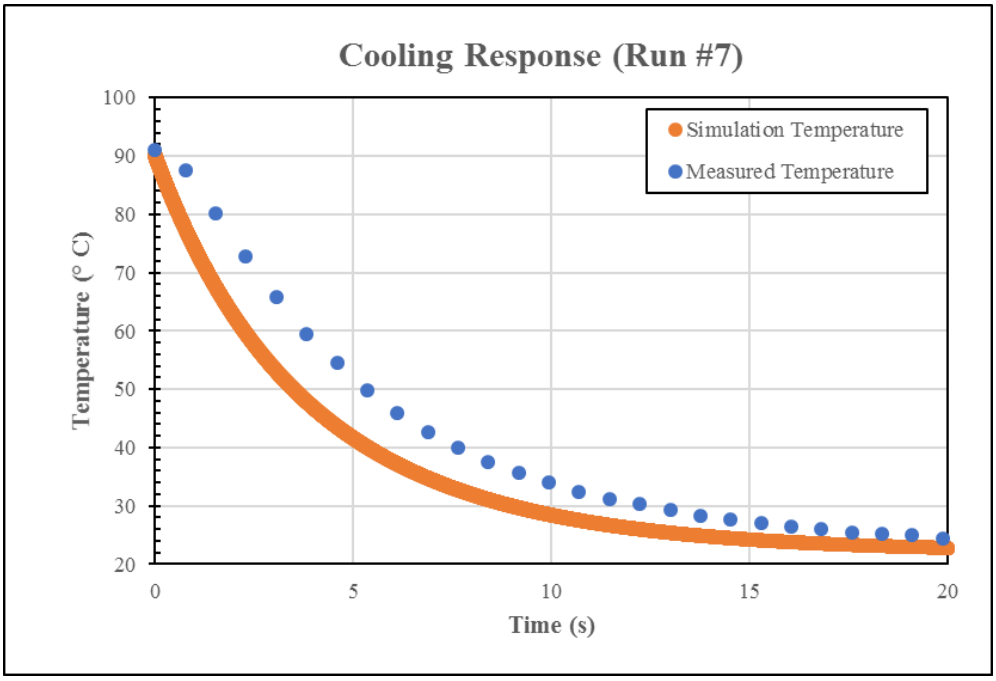

Figure 43. Cooling Response (Run #7)

The shape memory alloy wire was tested in such a way that the complete transformation could be observed.

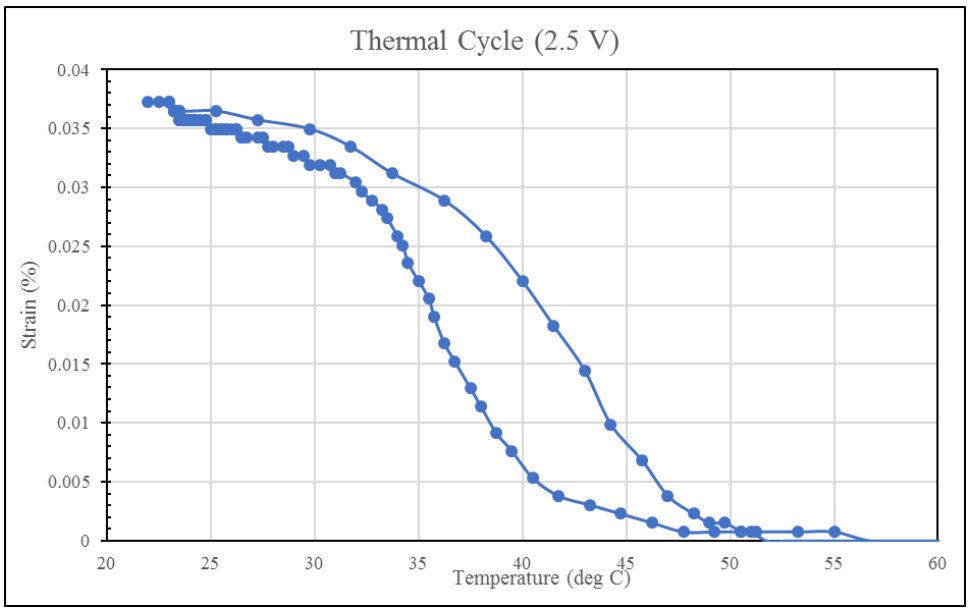

Figure 44. Experimental Shape Memory Effect (Run #8)

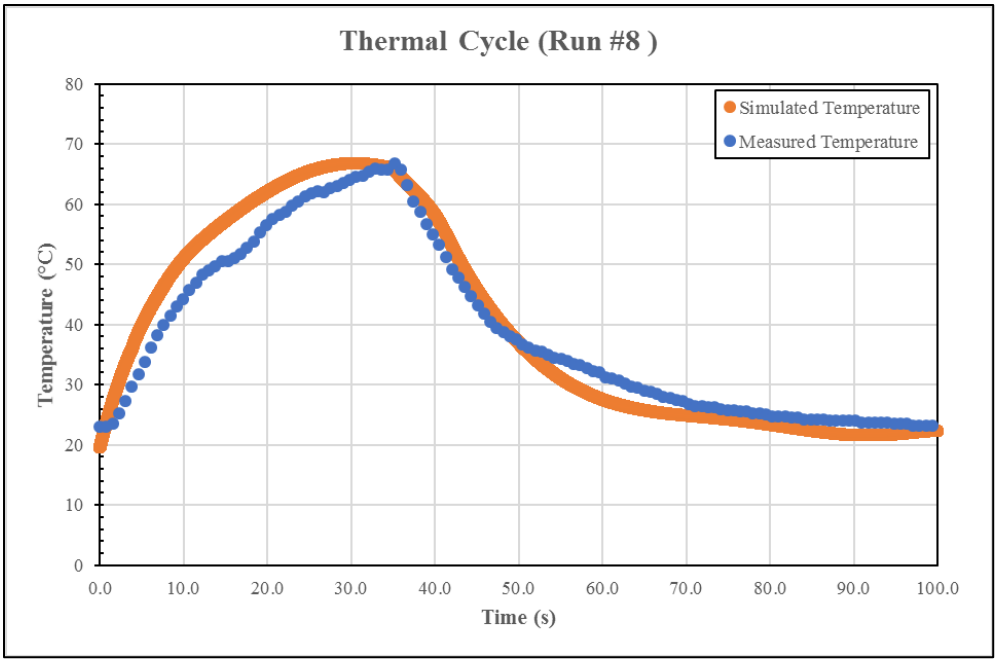

Figure 45. Thermal Cycling with Complete Transformation (Run #8)

The results of the experiments carried out on the superelastic and shape memory wires are summarized through the use of the mean squared error of the simulation versus the measured temperature response and the average percent error of the predicted response. These results are summarized in Table 10. To compute an average percent error across the entire transient response, a non-dimensionalized version of temperature was crafted such that $T^* = \frac{T}{T_\infty}$, where T_∞ and T are given as absolute temperatures (e.g. in Kelvin). The percent error may then be defined as:

$$\% \text{ error} = \frac{|T^*_{simulation} - T^*_{measured}|}{T^*_{measured}} \times 100\% \qquad (3.4.3.1)$$

Table 10. Thermal Modelling Error Statistical Breakdown

Experiment	Root Mean Squared Error (℃)	Average Normalized Percent Error (%)
Run #1 Heating	1.22	0.366
Run #1 Cooling	0.57	0.156
Run #2 Heating	1.58	0.449
Run #2 Cooling	1.82	0.452
Run #3 Heating	1.16	0.244
Run #3 Cooling	0.84	0.144
Run #4 Heating	2.10	0.536
Run #4 Cooling	2.02	0.426
Run #5 Heating	1.00	0.301
Run #5 Cooling	0.77	0.168
Run #6 Heating	1.85	0.502
Run #6 Cooling	3.05	0.878
Run #7 Heating	2.22	0.539
Run #7 Cooling	2.47	0.643
Run #8 Thermal Cycle	1.82	0.481

The lumped capacitance model captures the behavior of the thermal response relatively well. The sources of error that do emerge can be attributed to the accuracy of the thermocouple, which is given as $\pm 2℃$, as well as the time constant of the thermocouple probe combined with the delay effects of converting the raw thermocouple data into temperature data. There are also errors in assuming the temperature does not vary along the wire as is implied by the lumped capacitance model and also a reason why the time constants for heating and cooling are close to one another in each experiment, but not exactly the same. An additional source of error comes from the inability to directly measure the specific heat capacity to a great deal of precision for use in the simulation. Because of this, tabulated values in literature were used instead. Finally, the empirical methods used to find the convection coefficient during the simulation carry with them a potential error as high as twenty percent.

The results of logging the temperature profile in Run #6 are shown in Figure 46. Note that the temperature gradient is very sharp and that outside of the crimps the actuator is fairly close to room temperature.

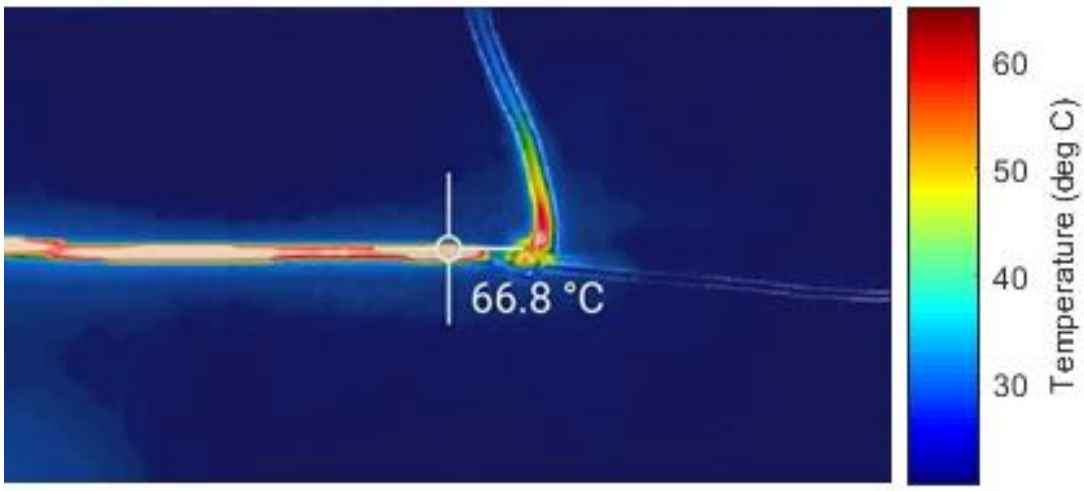

Figure 46. FLIR Image of Boundary Effects

Figure 47 shows the predicted response for the same experiment. Note that the center of the wire is the hottest portion, which is intuitive as the centerline is the furthest away from the surface of the wire which loses heat to convection and radiation. Also note that the temperature gradient is very sharp in the simulation, lending some credence to the accuracy of the solution.

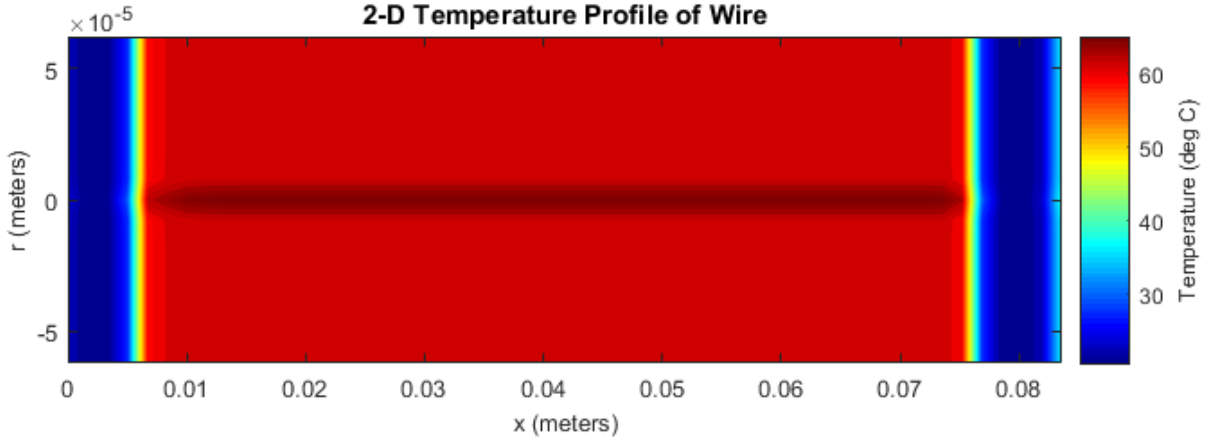

Figure 47. Simulation of Heating/Cooling Response

Chapter 4: Multibody Dynamics Implementation

4.1 Model Implementation

The constitutive equations that describe the behavior and heat transfer of Nitinol wire were placed into ADAMS, the multibody dynamics solver. ADAMS was chosen because the variable step integrators would allow for high accuracy in using the constitutive model, and would allow for controllers to be tested via simulation before experiments would have to be performed. Some parameters, such as the phase composition, cannot be measured in practice and a module that could show these parameters accurately is of inherent value.

Because ADAMS utilizes the Newton-Raphson method of solving for roots whilst searching for a converged solution at every integration step, it naturally succumbs to the method's inability to accurately handle functions that are not "well behaved". This means that functions with rapidly changing derivatives, or discontinuities, will often not lead to a convergent solution. Therefore, a variety of smoothing functions exist to replace the hard logic of an operator such as the IF() operator which is utilized in the constitutive model specified in Equation 2.4.1. An example of these smoothing operators would be the STEP() or STEP5() operators, which can be used to smooth transitions with either cubic or fifth order polynomials, the hyperbolic tangent function TANH(), or the HAVSIN() function, which utilizes the haversine function. These operations can be expressed mathematically as:

$$\mathrm{STEP}(t, t_0, x_0, t_1, x_1) = \begin{cases} x_0, & t < t_0 \\ x_0 - (x_1 - x_0)\left(\frac{t - t_0}{t_1 - t_0}\right)^2 \left(3 - 2\left(\frac{t - t_0}{t_1 - t_0}\right)\right), & t_0 \le t \le t_1 \\ x_1, & t \ge t_1 \end{cases} \tag{4.1.1}$$

$$\mathrm{STEP5}(t, t_0, x_0, t_1, x_1) = \begin{cases} x_0, & t < t_0 \\ x_0 - (x_1 - x_0)\left(\frac{t - t_0}{t_1 - t_0}\right)^3 \left(10 - 15\left(\frac{t - t_0}{t_1 - t_0}\right) + 6\left(\frac{t - t_0}{t_1 - t_0}\right)^2\right), & t_0 \le t \le t_1 \\ x_1, & t \ge t_1 \end{cases} \tag{4.1.2}$$

$$\mathrm{HAVSIN}(t, t_0, x_0, t_1, x_1) = \begin{cases} x_0, & t < t_0 \\ \dfrac{x_0 + x_1}{2} + \dfrac{x_1 - x_0}{2}\left(\sin\left(\pi\left(\dfrac{t - t_0}{t_1 - t_0}\right) - \dfrac{\pi}{2}\right)\right), & t_0 \le t \le t_1 \\ x_1, & t \ge t_1 \end{cases} \tag{4.1.3}$$

A comparison of the different smoothing functions is provided below (Figure 48).

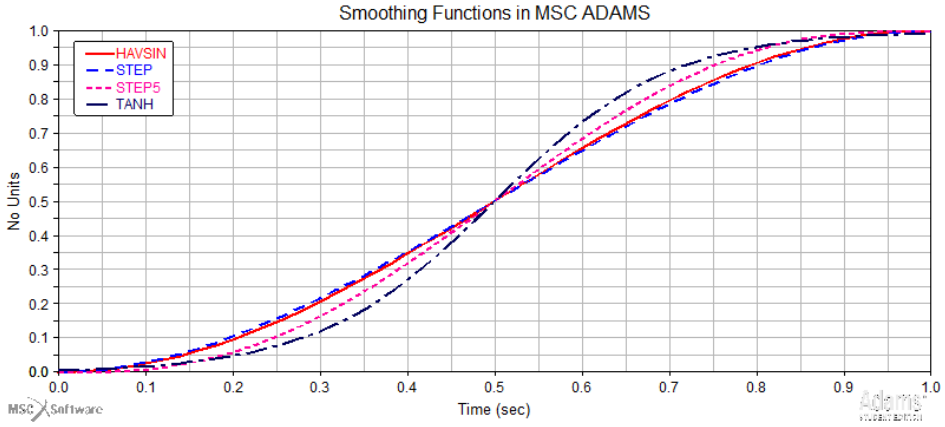

Figure 48. Smoothing Function Comparison in ADAMS

Whilst these smoothing operators all have advantages and drawbacks, the STEP5() operator was selected as it returns the most consistent results. The constitutive model then takes the following form using MSC ADAMS syntax:

$$\xi = \mathrm{STEP5}\left\{\frac{dT}{dt} - \frac{\dot{\sigma}}{\mathrm{C}}, -1, \ \xi_{A\to M}, 1, \xi_{M\to A}\right\} \tag{4.1.4}$$

$$\xi_A = \mathrm{STEP5}\left\{\frac{dT}{dt} - \frac{\dot{\sigma}}{\mathrm{C}_A}, -1, \ \xi_A, 1, \xi\right\} \tag{4.1.5}$$

$$\xi_M = \mathrm{STEP5}\left\{\frac{dT}{dt} - \frac{\dot{\sigma}}{\mathrm{C}_M}, -1, \ \xi, 1, \ \xi_M\right\} \tag{4.1.6}$$

The first argument of these operators is the independent variable under evaluation. If the independent variable is below the second argument, then the third argument is returned. Likewise, if it is above the fourth argument, then the fifth argument is returned. If the independent variable is between the second and fourth arguments, then the returned value is interpolated between the third and fifth arguments using a fifth order polynomial, which ensures that the time response of

the phase fraction and its time derivative are continuous and differentiable. In order to reference variables from the previous integration time step, elements called sensors are utilized which store these values and can be referenced by calling the function SENVAL(). The wire module functions by computing the actuator strain using the above model to compute the crystalline phase composition, and using the capabilities of the ADAMS software to find the force applied to the wire.

4.2 Model Verification

The first application of the SMA module was to apply it to a simple application where the anchored wire holds up a five gram hanging mass. The force of gravity acting on the mass serves as a preload force. To demonstrate the super-elastic effect, the temperature of the wire is held constant (beyond the *A* transformation region) and an oscillating force is then applied to the mass, given by:

$$F(t) = (0.1\ \text{N})t + (0.5\ \text{N})(1 - \cos(2\pi t)) \tag{4.2.1}$$

The resulting crystalline phase composition (from Eq. 4.1.4) and strains, are then plotted (Figure 49)

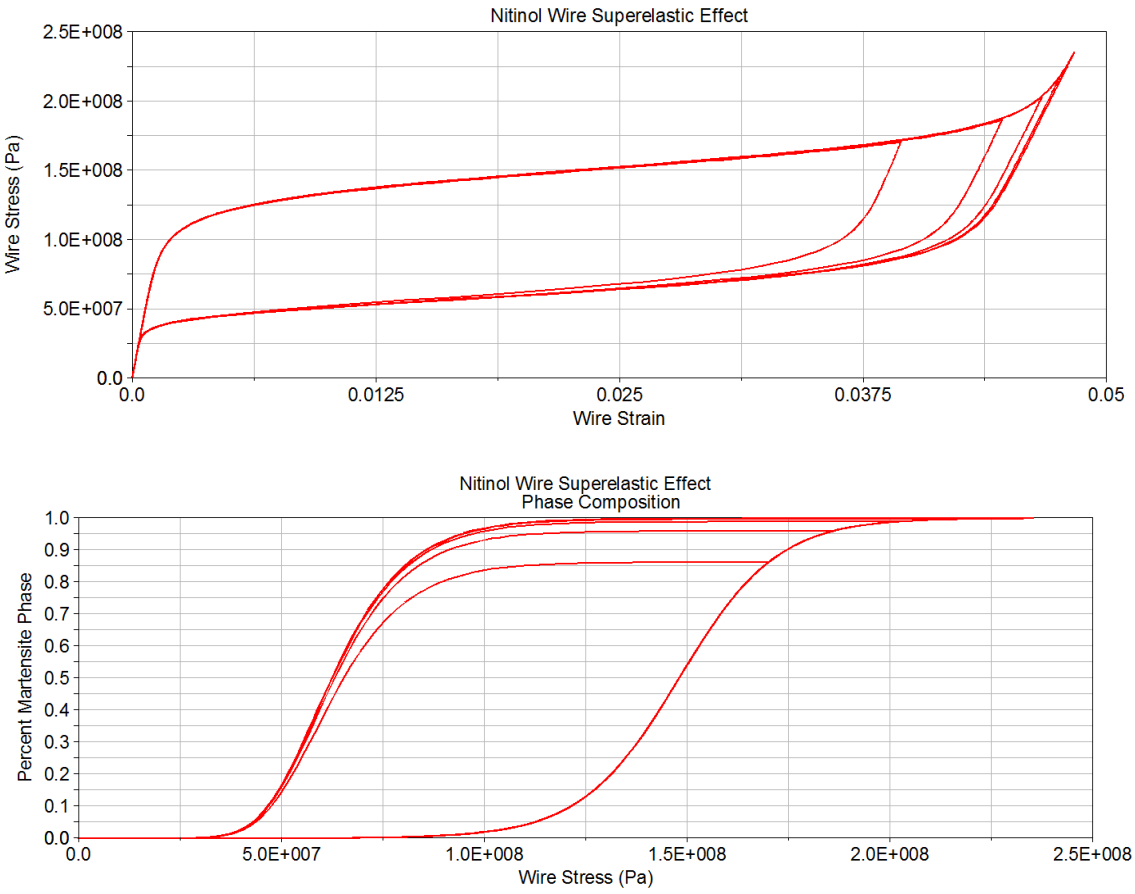

Figure 49. Superelastic Effect in ADAMS

By holding the stress constant and instead oscillating the temperature with the function expression found in Eq. 4.1.8, the shape memory effect can instead be seen (Figure 50):

$$T(t) = (23\ °\text{C})t + (10\ °\text{C})(1 - \cos(2\pi t)) \tag{4.1.8}$$

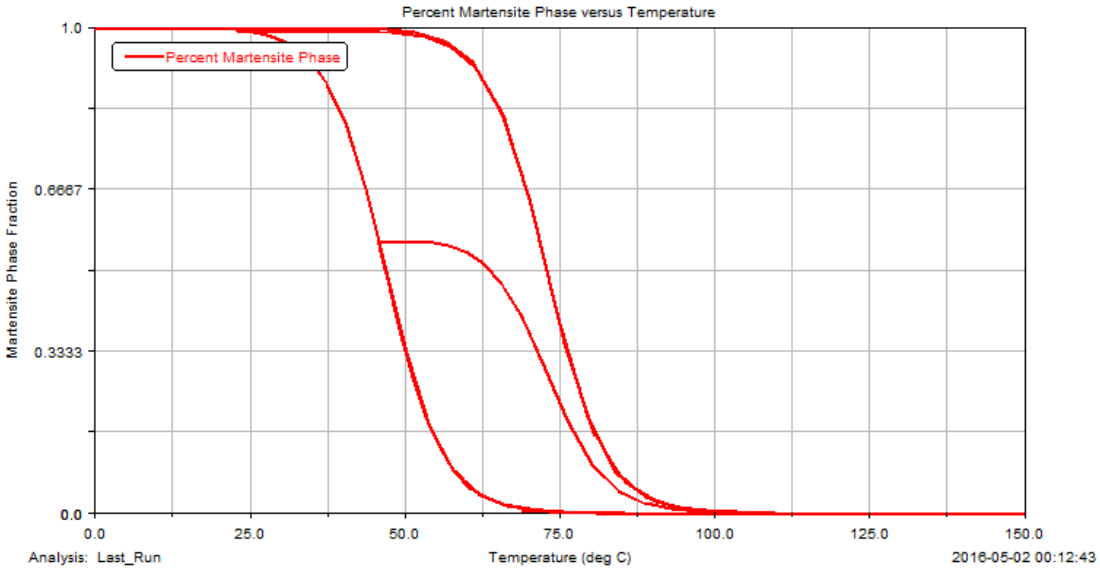

Figure 50. Shape Memory Effect in ADAMS

Both simulations demonstrate the characteristic hysteresis of the SMA. This set of routines is useful because it allows for more information to come from simulations (such as phase composition) than can be measured in an actual experiment. This includes the crystalline phase composition, the wire resistivity, and the wire temperature. If a temperature sensor were used, the wire temperature would be difficult to measure to a high degree of accuracy because probe invariably change the wire temperature.

4.3 Experimental Setup

In order to verify the ADAMS model was working for a dynamics system, a ball-beam balancer was modelled and run with a variety of control laws (Figure 51).

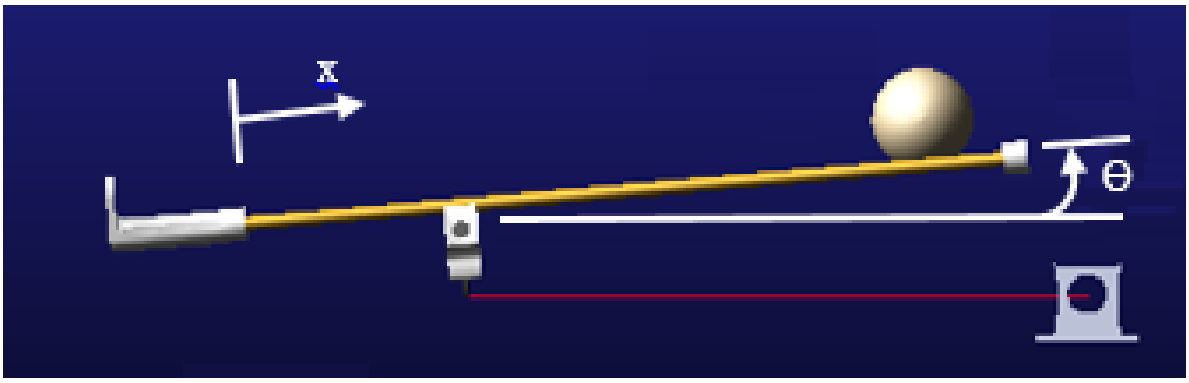

Figure 51. Ball-Beam-Balancer ADAMS Model

The model includes two twelve-inch-long brass tubes with an outer diameter of 7/32" and a wall thickness of 0.014 inches. The end pieces and the pivot piece are given mass properties of ABS. The pivot is placed 3.5 inches away from the center of the brass tubes. A beam angle of seven degrees corresponds to $\xi = 0$. The nitinol wire is connected to a 12 V supply and regulated using pulse-width modulation (PWM). A complete list of properties is provided in Table 11.

Table 11. Ball-on-a-Beam Properties

Ball Properties			
Property	**Value**	**Units**	**Formulation**
Mass [m]	0.0027	kg	*Standard*
Radius [R]	0.019939	m	*Standard*
Volume [V]	3.32E-05	m^3	(4/3)π*R^3
Density [ρ]	81.31395	kg/m^3	m/V
Contact Angle [Θ]	46.90837	degrees	arctan(F_y/F_z)
Rolling Radius [r]	0.014560696	m	R*sin(Θ)
Moment of Inertia [J]	4.29369E-07	kg m^2	(2/5)*m*R^2
Effective Inertia [m_{eff}]	0.00473	kg	(J/(r^2)) + m
Beam Properties			
Property	**Value**	**Units**	**Formulation**
Mass [M]	0.04691	kg	*SolidWorks*
Moment of Inertia about Assembly COM [I_0]	546.48	g cm^2	*SolidWorks*
Distance from Pivot to Assembly COM [d]	0.14	cm	*SolidWorks*
Moment of Inertia about Assembly Pivot [I_P]	547.40	g cm^2	I_0 + M*d^2

In order to control the position of the ball, sliding mode control is used in a cascaded controller arrangement (Figure 53). PID control is used with the ball position error to create a desired beam angle. The controller then uses the angle error to apply send power from a 12 V supply using duty cycles ranging from 0 % to 28% depending on the control law (where e_x denotes the ball position error, θ denotes the beam angle, and *D* denotes the duty):

$$\theta_{des} = Ke_x + K(a+b)\dot{e_x} + K(a*b)\int_0^t e_x dt \tag{4.3.1}$$

$$e_\theta = \theta - \theta_{des} \tag{4.3.2}$$

The gains for the angle controller were tuned by first constructing the transfer function from the beam angle to the ball position. The ball acceleration is related to the ball's angular acceleration by:

$$\ddot{x} = r_{eff}\ddot{\emptyset} \tag{4.3.3}$$

where r_{eff} is the effective rolling radius of the ball. The torque experienced by the ball is given by:

$$T_{ball} = mgr_{eff}\sin(\theta) = J\ddot{\emptyset} \tag{4.3.4}$$

The friction experienced by the ball is given by:

$$F_f = \frac{T_{ball}}{r_{eff}} \tag{4.3.5}$$

The equation of motion is then found to be:

$$m\ddot{x} = mg\sin(\theta) - \frac{J\ddot{\emptyset}}{r_{eff}} \tag{4.3.6}$$

Mapping this expression into the Laplace domain yields the desired transfer function:

$$\frac{X(s)}{\theta(s)} = \frac{mg}{\left(\frac{J}{{r_{eff}}^2} + m\right)s^2} = \frac{5.605}{s^2} \tag{4.3.7}$$

The angular PID controller was then tuned in order to achieve a damping ratio of 0.707, which is accomplished with poles places at -0.15 and -1.0 with a controller gain of 0.062 as shown in Figure 52.

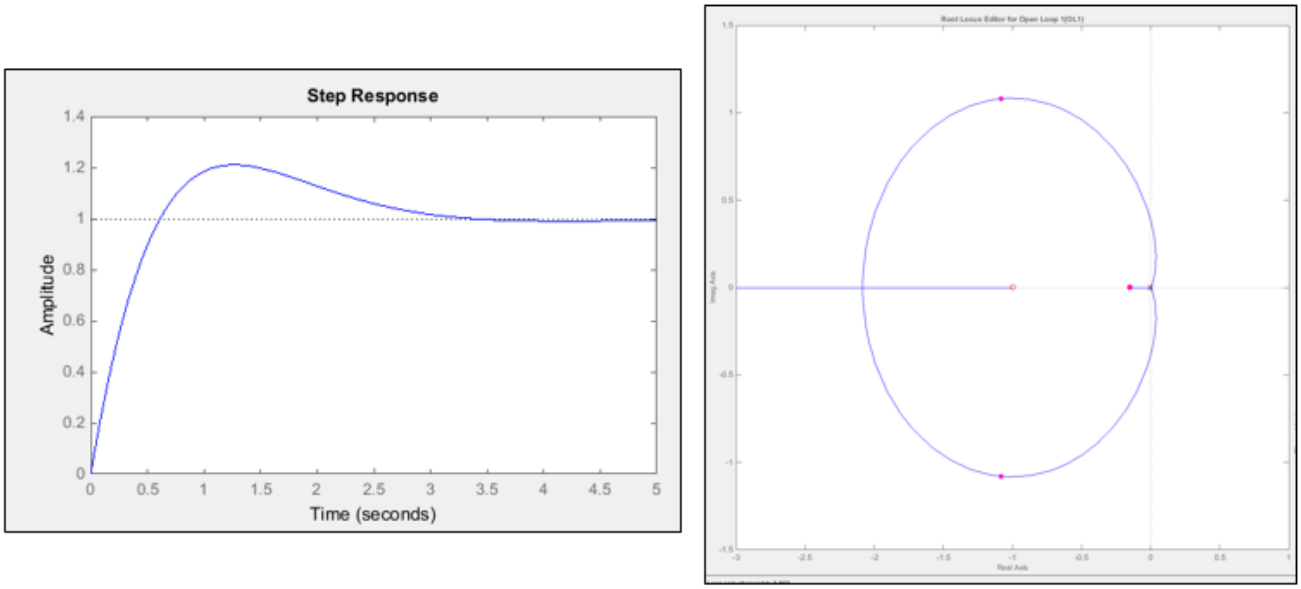

Figure 52. Pole Placement in MATLAB using SISO tool

From this point, two control laws were tested. The first is a separate PI control that takes the angle error and generates a duty cycle based on the following law:

$$D_{PI} = e_\theta + 0.01\int_0^t e_\theta dt \tag{4.3.3}$$

The SMC control laws are governed by the following block diagram representation (Figure 53)

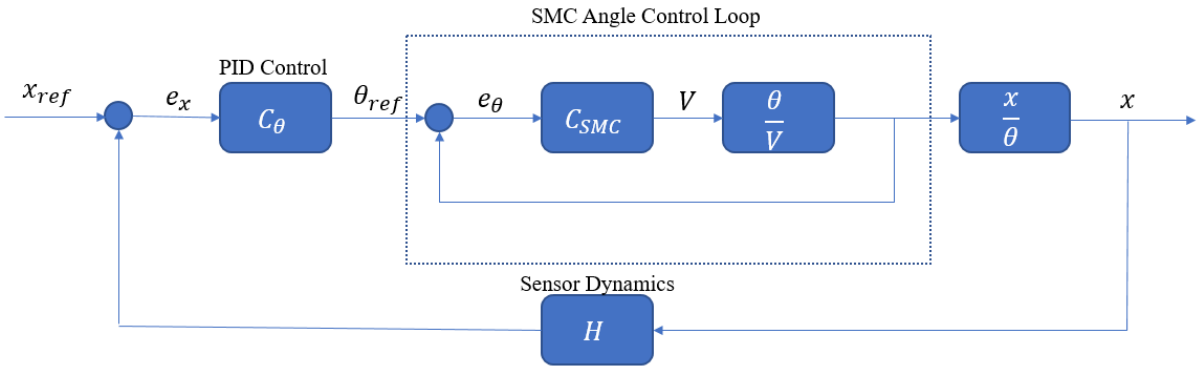

Figure 53. SMC Control Laws Block Diagram

$$D_{SMC} = \begin{cases} 0.28, & \text{for } \dot{e_\theta} + 100e_\theta > 0 \\ 0, & \text{for } \dot{e_\theta} + 100e_\theta \leq 0 \end{cases} \tag{4.3.4}$$

The pulse wave associated with a given duty generates a rectangle waveform that can be simply modelled by using the constant RMS value for the voltage over the interval in which the duty is turned on. This is because the pulse frequency of 11 kHz is much greater than the system bandwidth of 0.55 Hz. This voltage is then given by:

$$V_{RMS} = V_{peak}\sqrt{D} \tag{4.3.5}$$

During simulation of the SMC control laws, the average resistance of the wire was found to be approximately 16 ohms. This means that approximately 2.52 Watts of electrical power is sent through the wire during heating. The cooling power of the wire can fall anywhere between 0.7 and 1.2 Watts (depending on the wire temperature) from results found during simulation, which is approximately half of the heating power. This means that the heating of the wire and cooling of the wire should occur at approximately the same rate, which indicates that 28% duty is a fairly good value to use with the sliding mode control laws.

The dimensions of all the components used for the experimental assembly are identical to those used in the ADAMS simulation. The end-pieces of the beam and the pivot point are 3D printed of ABS plastic. A steel shaft is placed through two bearings and the printed pivot piece, which is free to rotate as the shaft rotates. The printed pivot piece has a screw placed at the bottom in order to attach the wire without melting the plastic. High temperature NiTi wire [76] with 0.125 mm diameter was selected as the SMA actuator and is attached from this mounting point to a bearing located 24 centimeters away from the pivot mount when the beam is perfectly horizontal. The pivot is offset so that the SMA actuator is given a preload in order to provide the necessary antagonism so that the beam can be free to rotate in both directions from horizontal. The nitinol wire was soldered to an electrically conducting wire that was connected to a Teensy 3.2 microcontroller. This microcontroller sent out a controlled PWM signal at 11 kHz, drawing power from a nearby 12 V battery. A Sharp GP 2Y0A41SK0F IR range sensor [79] was mounted onto the larger ABS end piece and used to read the position of the ball along the beam (Figure 54). The beam angle was read from using a dual measurement technique with the SMA wire in which the voltage is measured at three locations along the wire (at ground, at a stationary probe over which the wire slides, and where the wire attaches to the pivot). The change in wire length can be found by making the assumption that the resistance is constant throughout the wire and using a self-sensing technique to derive the wire's length [78] . Knowledge of this length yields the beam angle. A linear potentiometer was used to verify these measurements. A complete Austenitic transformation corresponded to roughly a seven degree angle of inclination.

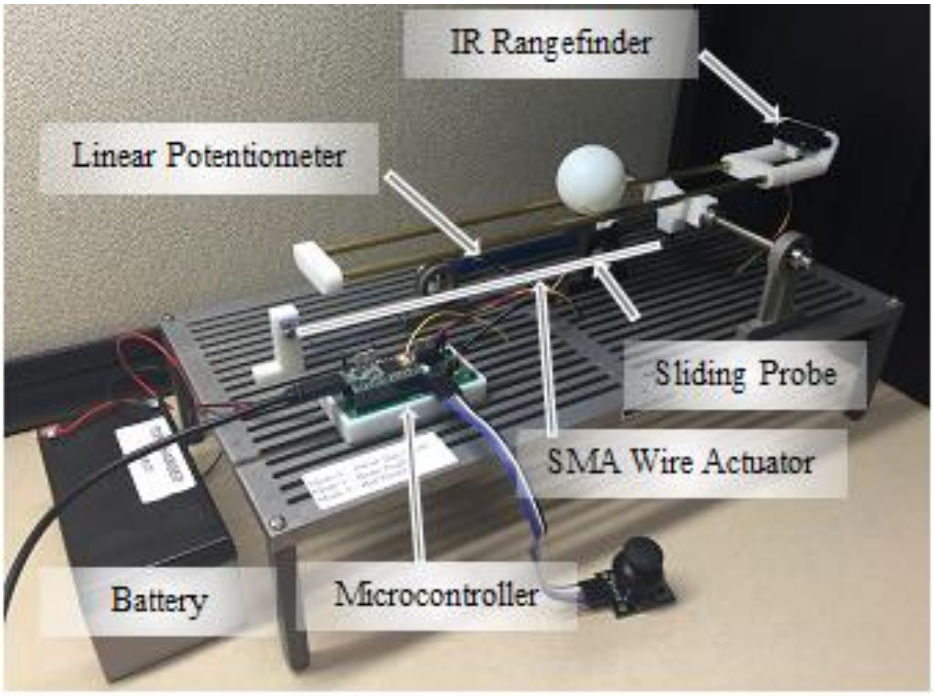

Figure 54. Experimental ball-on-a-beam assembly (SMA wire is Highlighted for visibility)

The ball's starting position during experimentation is on the far side of the beam away from the IR sensor, and the NiTi actuator starts heated up and completely transformed into Austenite, so as to tilt the beam in a way that the ball will roll back towards the IR sensor. The set point was set to be 15 cm away from the ABS end piece on which the IR sensor was mounted. The results of the ball position were logged through use of the serial logging available through the microcontroller; data was passed through a low-pass filter to cancel out some noise in the sensor readings and plotted in MATLAB.

4.4 Results and Conclusions

The results of running the balance beam experiment with the PID control laws are plotted below (Figure 55). Note that the red line corresponds to the steady state position of the ball, thus the ball can be said to have a steady state error of roughly one centimeter.

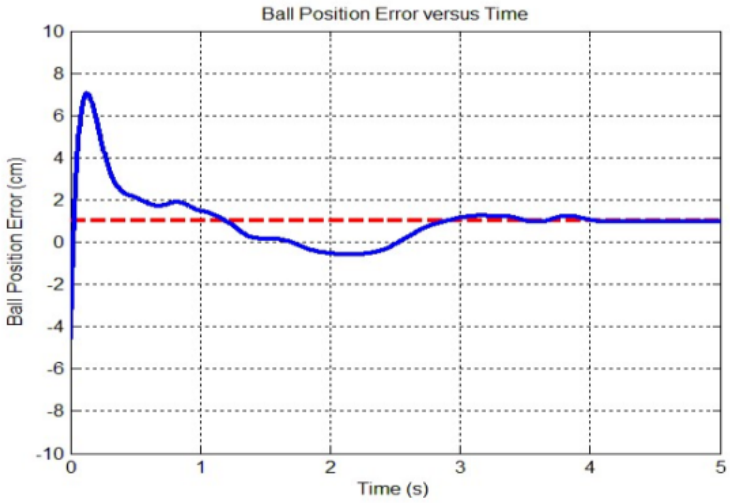

Figure 55. Ball Position Error using PID Control (Experiment)

The results of the simulation were recorded for five seconds after the ball was free to move (Figure 56). The dotted line denotes the steady state position of the ball.

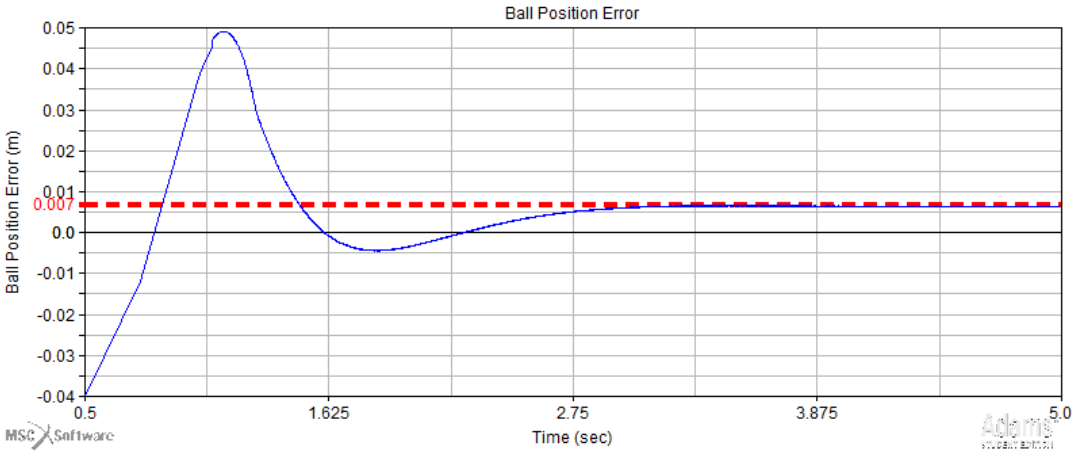

Figure 56. Ball Position Error using PID Control (ADAMS)

The results match very well with the experimental data, even predicting the steady state error (with the simulation prediction being a steady state error of 0.7 centimeters). The results of the system response when utilizing the sliding mode control laws is then given below (Figure 57).

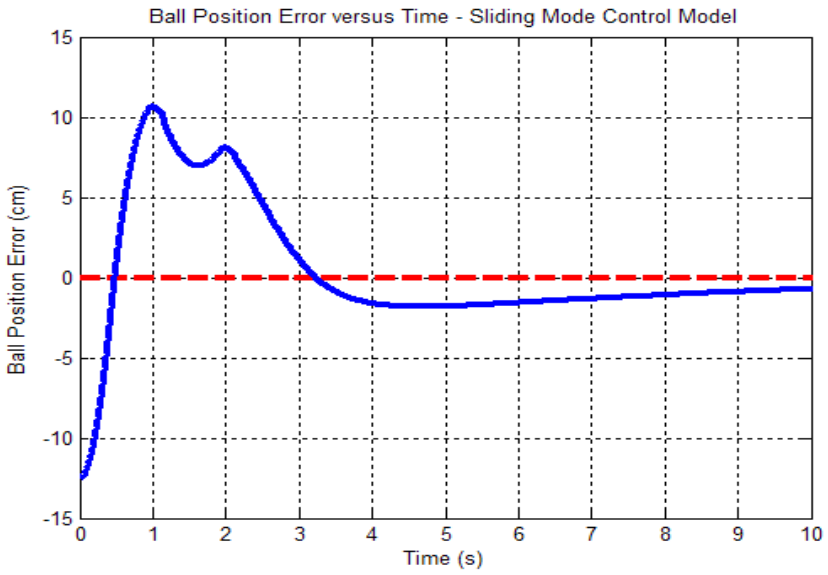

Figure 57. Ball Position Error using SMC Control (ADAMS)

Sliding mode control results in zero steady state error. Whilst the plots are not shown here, the beam angle was also much more stable than with PID control, having an extremely damped response.

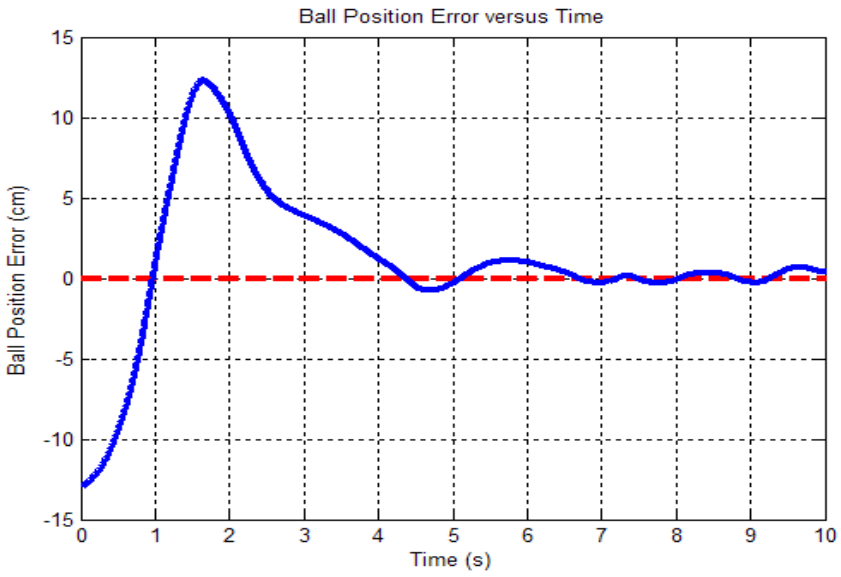

Figure 58. Ball Position Error using SMC Control (Experiment)

The experimental results (Figure 58)**Figure 58.** Ball Position Error using SMC Control (Experiment) show very similar responses until after the ball starts to settle into position. The small oscillations at this point can be attributed to small amounts of air flow over the wire causing some disturbance in the system via small phase changes in the wire itself.

The high levels of accuracy in predicting how the controllers behave show that the constitutive equations allow for the effective modelling of the SMA crystalline fraction as a result of temperature and stress inputs. This crystalline phase percentage can be used to define the macroscopic properties of the material, which in turn are fed into the heat transfer model developed from Eq. 3.2.1.1, which returns the new temperature inputs for modelling crystalline phase percentages at later time steps. Some common simplifying assumptions, such as neglecting the latent heat of transformation, are not made in this model so as to increase its degree of accuracy versus other models. This model has a very wide scope of potential applications, as it is able to account for changes in temperature and stress and accurately modelling these effects.

This improved constitutive model was fed into MSC ADAMS, and simulations showed that a variety of control schemes that could be used to control the ball position using an SMA wire. For experiments run with the cascaded controller scheme with the selected PID control laws, there was always a degree of steady state error for our chosen gains. The ADAMS simulations of these same experiments captures this steady state error, and also captures to a high degree of accuracy the rise time, settle time, and overshoot present in the actual model. The SMC control scheme was implemented because of its robustness in the face of the nonlinearities of SMA behavior, and this model under the same initial conditions features no steady state error and a much higher level of damping in comparison to the PID control scheme.

An investigation was also performed to see the effect on higher convection coefficients on the time it would take for the ball to stabilize. In general, a higher convection coefficient (such as for cases where the wire is exposed to a crossflow) results in a faster response time, until the convection coefficient reaches a certain value at which the response time is not significantly affected (Figure 59).

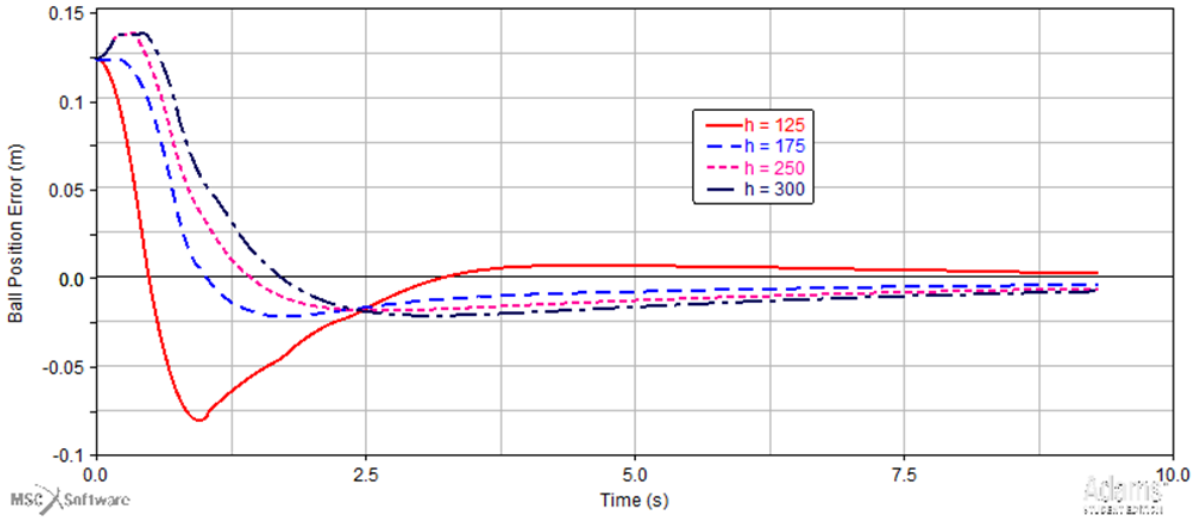

Figure 59. Simulation with varying Convection Coefficients

The results of the simulations run with the SMA actuator module are always presented in the postprocessor with the following animation, displaying real-time tracking of the beam angle as well as the phase fraction (Figure 60):

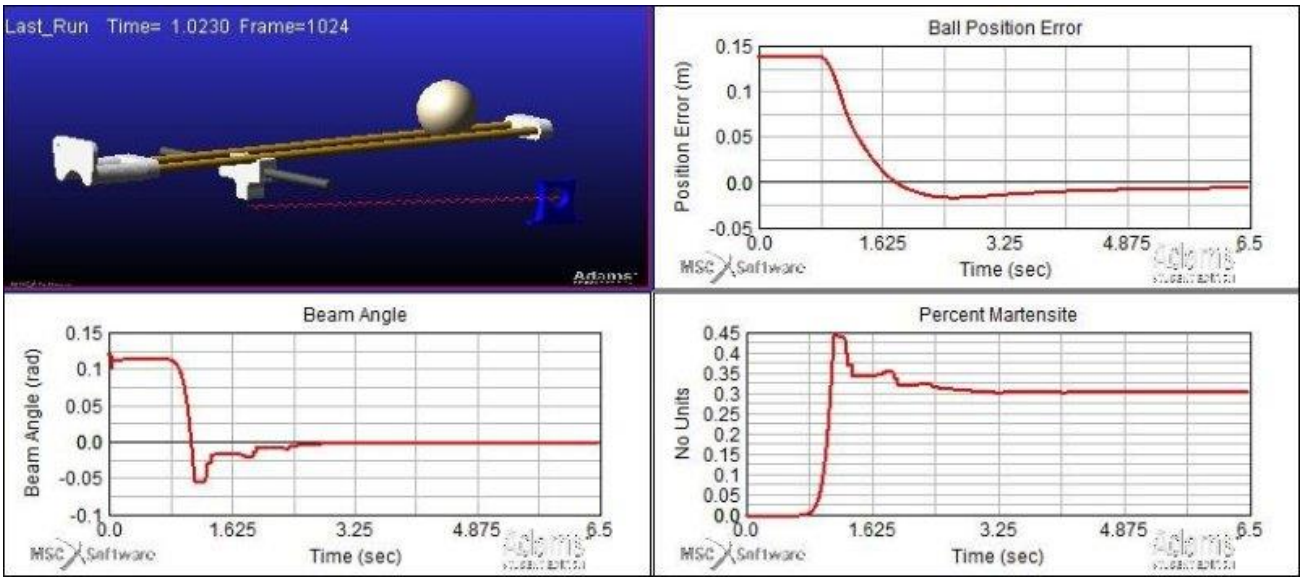

Figure 60. Post-Processing Environment for User

The temperature of the wire can also be displayed, but user written routines have been implemented that show the temperature of the wire on a color scale where red is indicative of hotter temperatures and blue is indicative of colder temperatures.

Chapter 5: Discussion and Conclusion

This literature presents a variety of analytical and numerically derived models that work to predict the behavior of shape memory alloy actuators in robotics applications. The analytical approaches are suitable for gaining insights on if shape memory alloys are a suitable alternative to more traditional actuators due to their problems of low bandwidths and low efficiency. The numerical techniques and simulations have been shown to accurately capture the temperature response and kinetic response to a controller input, making them suitable for the prototyping phase of a design. The lumped capacitance model, such as the one used in the MSC ADAMS simulations is suitable for most long, thin actuators and not computationally expensive to evaluate. However, for shorter spans of wires, boundary effects can heavily influence the amount of strain delivered by the actuator and the lengthwise discretization techniques can provide an adequate representation of these effects. For larger diameter actuators, radial discretization may prove useful to demonstrate the radial temperature gradient and its effect on the wire temperature response and ultimately its response to control laws.

Future research should be done on the kinetics modelling and how it feeds into the temperature model. The nature of the schemes presented here is to model the temperature implicitly and then solve for the phase fraction and ultimately the actuator stress and strain explicitly and then reiterating the same time step with the new values of the phase fraction and stress. While this does prove to be a stable solution process for small time steps, the kinetics model as is currently implemented requires very small time steps, especially when the transformation reverses directions and a discontinuity arises, to remain accurate.

References

[1] X. Huang, G. Ackland and K. Rabe, "Crystal structures and shape-memory behaviour of NiTi," *Nature Materials,* vol. 2, pp. 307-311, 2003.

[2] T. Duerig and C. Wayman, "An Introduction to Martensite and Shape Memory," in *Engineering Aspects of Shape Memory Alloys*, London, Butterworth-Heinemann Publishers, 1990, pp. 3-20.

[3] M. Kök, F. Dağdelen, A. Aydoğdu and A. Y., "The change of transformation temperature on NiTi shape memory alloy by pressure and thermal ageing," in *9th International Conference on Magnetic and Superconducting Materials,* 2016.

[4] V. Novak, P. Sittner, G. Dayananda, B. Braz-Fernandes and K. Mahesh, "Electrical resistance variation of NiTi shape memory alloy wires in thermomechanical tests: Experiments and simulation," *Materials Science and Engineering A,* Vols. 481-482, pp. 127-133, 2008.

[5] H. Song, E. Kubica and R. Gorbet, "Resistance Modelling of SMA Wire Actuators," in *International Workshop at the Smart Materials, Structures & NDT in Aerospace*, Montreal, 2011.

[6] J. Zhang and Y. Yin, "SMA-based bionic integration design of self-sensor-actuator-structure for artificial skeletal muscle," *Sensors and Actuators A: Physical,* vol. 181, pp. 94-102, 2012.

[7] J.-J. Zhang, Y.-H. Yin and J.-Y. Zhu, "Electrical Resistivity-Based Study of Self-Sensing Properties for Shape Memory Alloy-Actuated Artificial Muscle," *Sensors,* vol. 13, pp. 12958-12974, 2013.

[8] K. Tanaka, "A Thermomechanical Sketch of Shape Memory Effect: One-Dimensional Tensile Behavior," *Res Mechanica,* vol. 2, no. 3, pp. 59-72, 1986.

[9] C. a. R. C. Liang, "One-Dimensional Thermomechanical Constitutive Relations for Shape Memory Materials," *Journal of Intelligent Materials, Systems, and Structures,* vol. 4, pp. 229-242, 1993.

[10] K. Ikuta, M. Tsukamoto and S. Hirose, "Mathematical Model and Experimental Verification of Shape Memory Alloy for Designing Micro Actuator," in *Micro Electro Mechanical Systems (MEMS '91) Proceedings. An investigation of Micro Structures, Sensors, Actuators, Machines, and Robots IEEE,* Nara, 1991.

[11] Y. Ivshin and P. T. J., "A thermomechanical model for a one variant shape memory material," *Journal of Intelligent Material Systems and Structures,* vol. 5, pp. 455-473, 1994.

[12] L. Brinson and M. Huang, "SimpliCcations and comparisons of shape memory alloy constitutive models," *Journal of Intelligent Material Systems and Structures,* vol. 7, pp. 108-114, 1996.

[13] A. Gurley, "Classifying the Development of SMA Actuator Phenomenological Models from the Past 30 Years," Auburn, AL.

[14] S. Furst, J. Crews and S. Seelecke, "Stress, strain, and resistance behavior of two opposing shape memory alloy actuator wires for resitsancebased self-sensing applications," *Intelligent Material Systems and Structures,* vol. 24, no. 16, pp. 1951-1968, 2013.

[15] Johnson Matthey Medical Components, "Nitinol Technical Properties," 2017. [Online]. Available: http://jmmedical.com/resources/221/Nitinol-Technical-Properties.html. [Accessed 29 April 2017].

[16] W. Johnson and R. Emery, "Modular prosthesis". United States of America Patent US 5858020 A, 12 January 1999.

[17] P. Chowdhury, G. Ren and H. Sehitoglu, "NiTi superelasticity via atomistic simulations," *Philosophical Magazine Letters,* vol. 95, no. 12, pp. 574-586, 2015.

[18] V. Antonucci, G. Faiella, M. Giordano, F. Mennella and L. Nicolais, "Electrical resistivity study and characterization during NiTi phase transformation," *thermochimica acta,* vol. 462, pp. 64-69, 2007.

[19] K. Ikuta, M. Tsukamoto and S. and Hirose, "Shape Memory Alloy Servo Actuator System with Electric Resistance Feedback and Application for Active Endoscope," in *Proceedings of 1988 International Conference on Robotics and Automation*, Philadelphia, 1988.

[20] L. Brinson and M. Huang, "Simplifications and Comparisons of Shape Memory Alloy Constitutive Models," *Journal of Intelligent Material Systems and Structures,* vol. 7, pp. 108-114, 1996.

[21] M. Elahinia and M. Ahmadian, "An enhanced SMA phenomenological model: II. The experimental study," *Smart Materials and Structures,* vol. 14, pp. 1309-1319, 2005.

[22] Pisces Conservation, "Growth II," 2010 December 18. [Online]. Available: ttp://www.piscesconservation.com/growthhelp/index.html?richards_curve.htm. [Accessed 10 April 2017].

[23] L. Li, Q. Li and F. and Zhang, "One-Dimensional Constitutive Model of Shape Memory Alloy with and Empirical Kinetics Equations," *Journal of Metallurgy, Hindawi Publishing Corporation,* vol. 2011, no. 563413, pp. 1-14, 2011.

[24] D. a. W. D. Madill, "Modeling and L2-Stability of a Shape Memory Alloy Position Control System," *IEEE Transactions on Control Systems Technology,* vol. 6, no. 4, pp. 473-481, 1998.

[25] N. Zotov, V. Marzynkevitsch and E. Mittemeijer, "Evaluation of kinetic equations describing the martensite-austenite phase transformation in NiTi shape memory alloys," *Journal of Alloys and Compounds,* vol. 616, pp. 385-393, 2014.

[26] T. R. Lambert, A. Gurley and D. Beale, "SMA actuator material model with self-sensing and sliding-mode control; experiment and multibody dynamics model," *Smart Materials and Structures,* vol. 26, no. 3, 2017.

[27] W. Huang, "Modified Shape Memory Alloy (SMA) Model for SMA Wire Based Actuator Design," *Journal of Intelligent Material Systems and Structures,* vol. 10, pp. 221-231, 1999.

[28] J. Swensen, A. Nawroj, P. Pounds and A. Dollar, "Simple, scalable active cells for articulated robot structures," in *2014 IEEE Conference on Robotics and Automation,* Hong Kong, 2014.

[29] S. J. Furst, J. H. Crews and S. Seelecke, "Numerical and experimental analysis of inhomogeneities in SMA wires induced by thermal boundary conditions," *Continuum Mechanical Thermodynamics,* vol. 10, no. 24, p. 497, 2012.

[30] R. Hilpert, *Forsch. Geb. Ingenierwes.,* vol. 4, p. 215, 1933.

[31] A. Zukauskas, "Heat Transfer from Tubes in a Cross Flow," *Advances in Heat Transfer,* vol. 8, pp. 93-160, 1972.

[32] S. Churchill and W. Bernstein, "A Correlating Equation for Forced Convection From Gases and Liquids to a Circular Cylinder in Crossflow," *The American Society of Mechanical Engineers,* vol. 99, no. 2, pp. 300-306, 1977.

[33] V. Morgan, "The Overall Convective Heat Transfer from Smooth Circular Cylinders," *Advances in Heat Transfer,* vol. 11, pp. 199-264, 1975.

[34] Indian Institute of Technology Delhi, "Free Convection Lecture Notes," [Online]. Available: http://web.iitd.ac.in/~prabal/MEL242/(23-24)-free-convection.pdf. [Accessed 17 May 2016].

[35] E. Le Fevre, "Laminar Free Convection from a Vertical Plane Surface," in *Proceedings of the 9th International Congress of Applied Mechanics*, Brussels, 1956.

[36] T. Cebeci, "Laminar-Free-Convective Heat Transfer from the Outer Surface of a Vertical Slender Circular Cylinder.," in *Proceedings of the Fifth International Heat Transfer Conference*, 1974.

[37] W. J. Minkowycz and E. M. Sparrow, *Journal of Heat Transfer,* vol. 178, no. 96, p. 178, 1974.

[38] J. Shaw and S. Kyriakides, " On the nucleation and propagation of phase transformation fronts in a NiTi alloy.," *Acta Materialia,* vol. 45, no. 2, pp. 683-700, 1997.

[39] M. Iadicola and J. Shaw, "An experimental method to measure initiation events during unstable stress-induced martensitic transformation in a shape memory alloy wire," *Smart Materials and Structures,* vol. 16, no. 1, pp. 155-169, 2007.

[40] M. G. Faulkner, J. J. Amalraj and A. Bhattacharyya, "Experimental determination of thermal and electrical properties of Ni-Ti shape memory wires," *Smart Materials and Structures,* vol. 9, pp. 632-639, 2000.

[41] A. Amini, C. Cheng, Q. Kan, M. Naebe and H. Song, "Phase Transformation Evolution in NiTi Shape Memory Alloy under Cyclic Nanoindentation Loadings at Dissimilar Rates," *Scientific Reports,* vol. 3, no. 3412, 2013.

[42] J. Wall, "Transient Heat Conduction: Analytical Methods," [Online]. Available: http://ewp.rpi.edu/hartford/~wallj2/CHT/Notes/ch05.pdf. [Accessed 2017 18 May].

[43] H. J. and F. S., Numerical methods for engineers and scientists, Boca Raton: CRC Press, 2001.

[44] D. Lagoudas and Z. Ding, "Modeling of thermoelectric heat transfer in shape memory alloy actuators: Transient and multiple cycle solutions," *International Journal of Engineering Science,* vol. 33, no. 15, pp. 2345-2364, 1995.

[45] S. Huang, M. Leary, T. Ataalla, K. Probst and A. Subic, "Optimisation of Ni–Ti shape memory alloy response time by transient heat transfer analysis," *Materials and Design,* vol. 35, p. 655–663, 2012.

[46] R. Mirzaeifar, R. DesRoches and A. Yavari, "Analysis of the rate-dependent coupled thermo-mechanical response of shape memory alloy bars and wires in tension," *Continuum Mechanical Thermodynamics,* vol. 23, p. 363–385, 2011.

[47] T. Evdaimon and M. a. D. P. T. Sfakiotakis, "A Closed-Loop Position Control Scheme for SMA-Actuated Joints," in *2014 22nd Mediterranean Conference on Control and Automation (MED)*, Palermo, Italy, 2014.

[48] J. Ditman, L. Bergman and T.-C. Tsao, "The design of extended bandwidth shape memory alloy actuators," *Journal of Intelligent Material Systems and Structures*, vol. 7, no. 6, pp. 635-645, 1996.

[49] V. Bundhoo, E. Haslam, B. Birch and E. Park, "A shape memory alloy-based tendon-driven actuation system for biomimetic artificial fingers, part I: design and evaluation," *Robotica*, vol. 27, no. 1, pp. 131-146, 2009.

[50] V. Bundhoo, E. Haslam, B. Birch and E. Park, "A shape memory alloy based tendon-driven actuation system for biomimetic artificial fingers, part II: modelling and control," *Robotica*, vol. 28, no. 5, pp. 675-687, 2010.

[51] L. Odhner and H. Asada, "Scaling up shape memory alloy actuators using a recruitment control architecture," in *Robotics and Automation*, Anchorage, AK, 2010.

[52] J. Ditman and L. Bergman, "A Comparison on the Effectiveness of Two Shape Memory Alloy Based Actuators," in *Intelligent Materials, Second International Conference Proceedings*, Colonial Williamsburg, VA, 1994.

[53] S. Nakshatharan, D. Kaliaperumal and D. Ruth, "Effect of stress on bandwidth of antagonistic shape memory alloy actuators," *Journal of Intelligent Material Systems and Structures*, vol. 27, no. 2, pp. 153-165, 2016.

[54] D. a. H. V. Grant, "Constrained Force Control of Shape Memory Alloy Actuators," in *Proceedings of the IEEE International Conference on Robotic and Automation*, San Francisco , 2000.

[55] S. Choi, H. Y. J. Kim and C. Cheong, "Force tracking control of a flexible gripper featuring shape memory alloy actuators," *Mechatronics*, vol. 11, no. 6, pp. 677-690, 2001.

[56] Y. Teh and R. Featherstone, "An Architecture for Fast and Accurate Control of Shape Memory Alloy Actuators," *The International Journal of Robotics Research*, vol. 27, pp. 595-611, 2008.

[57] Y. Teh, "Fast, Accurate Force and Position Control of Shape Memory Alloy Actuators," ANU College of Engineering and Computer Science, Canberra, 2008.

[58] Song, C. V. G. and C. Batur, "A Neural Network Inverse Model for a Shape Memory Alloy Wire Actuator," *Journal of Intelligent Material Systems and Structures*, vol. 14, pp. 371-377, 2003.

[59] C. Lan and C. Fan, "An accurate self-sensing method for the control of shape memory alloy actuated flexures," *Sensors and Actuators*, vol. 163, pp. 323-332, 2010.

[60] T.-M. Wang, Z.-Y. Shi, D. Liu, C. Ma and Z.-H. Zhang, "An Accurately Controlled Antagonist Shape Memory Alloy Actuator with Self Sensing," *Sensors*, vol. 12, pp. 7682-7700, 2012.

[61] R. Josephine, N. Sunja and K. Dhanalakshmi, "Differential resistance feedback control of a self-sensing shape memory alloy actuated system," *International Society of Automation Transactions*, vol. 53, pp. 289-297, 2014.

[62] Y. Teh and R. Featherstone, "Frequency Response Analysis of shape memory alloy actuators," in *International Conference on Smart Materials and Nanotechnology in Engineering*, Harbin, China, 2007.

[63] Gorbet, M. K. A. R. B. and R. C. Chau, "Mechanism of bandwidth improvement in passively cooled SMA position actuators," *Smart Materials and Structures,* vol. 18, pp. 1-9, 2009.

[64] T. C. Tszeng and V. Saraf, "A Study of Fin Effects in the Measurement of Temperature Using Surface-Mounted Thermocouples," *Journal of Heat Transfer,* vol. 125, pp. 926-935, 2003.

[65] V. Souza and E. Zaparoli, "Analysis of Error in the Surface Temperature Measurement of a Semi-Infinite Body," Brazilian Society for Mechanical Sciences and Engineering , São José dos Campos, 2000.

[66] P. E. Nikravish, Computer-Aided Analysis of Mechanical Systems, Tuscon: Prentice-Hall, Inc., 1988.

[67] "LMS Dads," Siemens , 2016. [Online]. Available: https://www.plm.automation.siemens.com/en_us/products/lms/virtual-lab/legacy-applications/dads.shtml. [Accessed 19 July 2016].

[68] "COMSOL Multibody Dynamics Module," COMSOL, 2016. [Online]. Available: https://www.comsol.com/multibody-dynamics-module. [Accessed July 19 2016].

[69] "ANSYS Rigid Body Dynamics," ANSYS, 2016. [Online]. Available: http://www.ansys.com/Products/Structures/Rigid-Body-Dynamics. [Accessed 19 July 2016].

[70] M. Quadrelli, P. Backes and e. al, "Investigation of phase transition-based tethered systems for small body sample capture," *Acta Astronautica,* vol. 68, no. 7-8, pp. 947-973, 2011.

[71] M. Kohl and B. Krevet, "3D Simulation of a Shape Memory Microactuator," *Materials Transactions,* vol. 43, no. 5, pp. 1030-1036, 2002.

[72] P. Terriault, F. Viens and V. Brailovski, "Non-isothermal finite element modeling of a shape memory alloy actuator using ANSYS," *Computational Materials Science,* vol. 36, no. 4, pp. 397-410, 2006.

[73] N. Lewis, Y. A and S. and Seelecke, "Experimental determination of thermal and electrical properties of Ni-Ti shape memory wires," *Smart Materials and Structures,* vol. 9, pp. 632-639, 2000.

[74] M. Hancock, "The 1-D Heat Equation," August 2006. [Online]. Available: https://ocw.mit.edu/courses/mathematics/18-303-linear-partial-differential-equations-fall-2006/lecture-notes/heateqni.pdf. [Accessed 12 May 2017].

[75] T. R. Lambert, A. Gurley and D. Beale, "Heat Transfer Modelling and Bandwidth Determination of Shape Memory Alloy Actuators in Robotics Applications," in *Early Career Technical Conference*, Birmingham, 2016.

[76] Dynalloy, Inc., "Technical Characteristics of Flexinol Actuator Wires," Irvine, CA.

[77] B. Fornberg, "Generation of Finite Difference Formulas on Arbitrarily Spaced Grids," *Mathematics of Computation,* vol. 51, no. 184, pp. 699-706, 1988.

[78] A. Gurley, Lambert, T. R., B. D. G. and R. Broughton, "Robust Self Sensing in NiTi Actuators using a Dual Measurement Technique," in *SMASIS*, Stowe, VA, 2016.

[79] " Sharp GP2Y0A21YK Datasheet," Sharp, 2005. [Online]. Available: https://www.sparkfun.com/datasheets/Components/GP2Y0A21YK.pdf. [Accessed 25 April 2015].

[80] X.-Y. Lu and S. K. Spurgeon, "Robust sliding mode control of uncertain nonlinear systems," *Systems & Control Letters*, vol. 32, no. 2, pp. 75-90, 1997.